Quantum Dot Dispersion in Block Copolymer Matrices

A Dissertation
SUBMITTED TO THE FACULTY OF THE
UNIVERSITY OF MINNESOTA
BY

Whitney Nowak Wenger

IN PARTIAL FULFILLMENT OF THE REQUIREMENTS
FOR THE DEGREE OF
DOCTOR OF PHILOSOPHY

Eray S. Aydil, co-advisor
Frank S. Bates, co-advisor

August 2018

Acknowledgements

First, I would like to express my sincere thanks to my advisors, Eray Aydil and Frank Bates, for their support, patience, and perseverance throughout this project. I am thankful for their guidance in navigating both the successes and failures of our work towards a greater understanding of this crazy idea and becoming a better scientist and engineer. Their infectious passion for they do will remain with me for a long time.

Thank you to all of the Aydil and Bates group members, who have provided assistance and thoughtful discussion over the years. In particular, I would like to thank Boris Chernomordik for starting me on my way in the Aydil lab, Robert and Danielle Hickey both for their assistance in identifying early pitfalls in my quantum dot synthesis and Rob in specific for helping me make my first polymer-QD composites, and Danielle in specific for insightful discussions on transmission electron microscopy. I would also like to thank Nancy Trejo for the many conversations in lab. Thank you to Ron Lewis for supplying polymers and answering my naïve questions. Thank you to Bongjoon Lee for the assistance in polymer staining and TEM. Thank you to Michael Maher for supplying a few homopolymers. Thank you to Ferry group members Dana Dement and Mayank Puri for our monthly quantum dot discussions, and Matthew Quan and Ryan Connell for their support in fluorescence measurements. Thank you to all of my classmates, who have worked as a group to support one another through classwork; my sincere thanks go to those I most closely worked alongside, including Dr. Michael Harris, Ryan Connell, Ron Lewis, Andrew Allman, and Jacob Held.

The CEMS department would cease to function without the crucial support and guidance of Julie Prince and Teresa Bredahl. I am thankful for their assistance along this journey.

Finally, thank you to my parents Ron and Connie, my brother Adam and my sister-in-law Kathryn, and my sister Rachael for being an endless system of support and source of laughter over the years. Thank you, Connie, for encouraging me to consider engineering when I was leaving high school, and for showing me that life has many possibilities if you are dedicated. Lastly, thank you to my life partner, Elliot Combs, who has been a constant source of love, encouragement, and support throughout my graduate studies. When this is all over, let’s talk about that trip to Europe.

For my family, new and old.

Abstract

Quantum dots (QDs) have demonstrated viability for a wide set of applications ranging from bioimaging to electronics. Their unique size-tunable band gaps and accessibility for roll-to-roll processing via solution synthesis makes them promising candidates in many of these areas. Several of these applications benefit from carefully manipulated spacing in QD films, often achieved through integration of QDs in a polymer matrix. Although many studies have achieved varying degrees of success in dispersing QDs in polymer matrices, there remains much to be understood about the path dependency of QD integration and how QDs may be integrated into sphere-forming polymer matrices.

In this work, CdSe QDs were synthesized via a hot injection technique in an air-free environment. These QDs were fabricated in a range of sizes based on the reaction time and were evaluated for their crystal structure, absorbance, fluorescence, ligand coverage, and dispersion in various solvents. The resulting QDs feature a wurtzite crystal structure and exhibit narrow absorbance and emission peaks. The QDs are well stabilized in nonpolar solvents like hexane and toluene via trioctylphosphine oxide (TOPO) and trioctylphosphine (TOP) ligands.

In the first approach towards QD integration in polymer matrices, the native TOPO ligands were exchanged for a poly(ethylene glycol) ligand functionalized with a thiol end group. The resulting QDs were qualitatively and quantitatively analyzed to determine the ligand density on the QD surface and the QD dispersion in different solvents. After ligand exchange, the QDs were no longer dispersible in nonpolar solvents like hexane but formed stable dispersions in solvents like tetrahydrofuran, chloroform, and water. Upon ligand exchange, 50-85% of the original ligands were removed and an average of 2-4 poly(ethylene glycol) ligands were installed on each QD surface.

The extent of QD dispersion in various homopolymers was evaluated using transmission electron microscopy (TEM). CdSe QDs were mixed with poly(lactic acid) in chloroform and dropcast into thin films for TEM. The resulting films indicate phase separation of the polymer and the QDs where the spacing between QDs does not change upon addition of the polymer. In a separate study, CdSe QDs were mixed with poly(butadiene) in n-hexane and dropcast into thin films for TEM. These films

demonstrated an increase in spacing between the QDs of roughly 2 nm. However, the majority of the polymer does not end up in the space between QDs and is phase separated from the QD crystal phase. Finally, CdSe QDs after ligand exchange with PEG were mixed with poly(lactic acid) in chloroform and dropcast into thin films for TEM. The resulting films indicate some mixing between the QDs and the polymer.

Finally, the extent of QD dispersion in various diblock copolymers was evaluated using small angle x-ray scattering (SAXS), TEM, and fluorescence measurements. CdSe QDs were mixed with a lamellae-forming poly(ethylene-*b*-cyclohexylethylene) in benzene and dried and heated to T ≈ 200°C and then cooled to 140°C to induce polymer ordering. The resulting solid composites exhibited aggregates of QDs via SAXS and TEM measurements. In a separate study, CdSe QDs were mixed with a body-centered cubic forming poly(styrene-*b*-butadiene) in benzene. Two types of samples were prepared: one formed from drying the polymer and QDs from the solvent and subsequently heating to 140°C, and one formed from dropcasting the dispersion of polymer and QD from the solvent. The resulting solid composite prepared with temperature processing was microtomed and exhibited QD aggregation in TEM. The dropcast sample exhibited phase separation of the QDs and the polymer. Finally, CdSe QDs were mixed with a body-centered cubic poly(lactide-*b*-butadiene) in a mixture of n-hexane and chloroform. Micelles with the minority poly(butadiene) block on the outside were formed in similar mixtures of n-hexane and chloroform and observed via dynamic light scattering. QDs were added to the polymer in a mixture of n-hexane and chloroform after micellization (at higher hexane concentrations) and before micellization (at lower hexane concentrations); in the latter case, hexane was added to induce polymer micellization after the addition of QDs. These dispersions were dropcast into films for TEM, which revealed similar film structures for both samples where QDs appeared at the interstices between roughly spherical shapes; these shapes were attributed to the formation of polymer microemulsions during the drying process. The effect of chloroform and n-hexane content of the solvent mixture on the composite formation was tested for various mixtures of n-hexane and chloroform. TEM of QD and polymer samples prepared from these solvent mixtures showed phase separation of QDs and polymer at low n-hexane concentrations and the polymer microemulsion structure for

higher n-hexane concentrations. Although this work focused on the integration of CdSe QDs, the insights demonstrated here should prove relevant for other nanoparticle-composite systems.

Table of Contents

List of Tables

List of Figures

Chapter 1 – Introduction

The traditional assumptions of bulk materials are challenged in the world of small materials, where length scales range from 1 nanometer to hundreds of nanometers. In this world, as few as hundreds of atoms can compose a single particle. The electronic and optical properties of bulk semiconductors change with material size, resulting in opportunities for innovative device design.[1-3]

Although unique for their individual properties, small materials and particles prepared into bulk composites open a new field of study integrating knowledge of inorganic and organic systems. Much like molecules or atoms can be assembled into complex structures, these particles can be used as building blocks for advanced materials carefully tuned to exhibit desired properties. Interactions between separate particles can be manipulated through distance and surface chemistry. Composites of these small materials can be made by assembling them via solvent processing or through integration in a host matrix. By engineering not only the small materials themselves, but their method of spatial arrangement, the materials can be tuned to exhibit unique properties.

Here, we review the characteristics of these small, semiconducting materials, known as quantum dots, and begin to explore how polymers may act as a template for organizing quantum dots in complex morphologies.

Section 1.1 – Quantum Dots: Characteristics and Properties

Quantum dots (QDs) describe a class of semiconductor nanoparticles in which the radius of the nanoparticle is smaller than the exciton Bohr radius (average distance between an excited electron and the hole it left behind). The exciton Bohr radius is a

property of the material itself; for CdSe, a commonly studied QD material, the exciton Bohr radius is ≈5.6 nm.[4,5] As a result of the nanoparticle size, QDs are quantum confined. Whereas bulk semiconductors exhibit a fixed band gap energy dependent on the semiconductor material, the band gap energy of QDs increases as a result of the confinement. QDs feature discrete energy levels as opposed to bulk semiconductors, which exhibit a continuous density of states. A schematic of this effect is given in Figure 1.1. Because of this characteristic, QDs are commonly called "artificial atoms.[2,6]" As the QD size is made smaller, the distance between energy states increases, resulting in a larger band gap; thus, QDs have an inverse relationship between QD size and band gap energy.

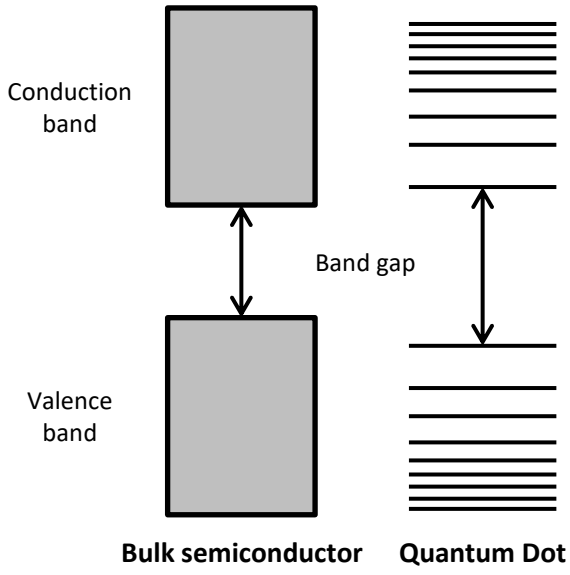

Figure 1.1: Cartoon schematic of the band structure of quantum dots compared to bulk semiconductors. Unlike bulk semiconductors, the band gap energy of quantum dots is affected by the quantum dot size.

The effect of QD size on the band gap is readily apparent in their optical properties. As the QD size increases, the band gap decreases, and the absorbance peak of the QDs shifts from higher energy (shorter wavelength) to lower energy (longer

wavelength). Similarly, for materials such as CdSe, which exhibits fluorescent properties, the emitted light shifts from blue or green to red as the QD radius increases from ≈ 2 nm to ≈ 5 nm. An example of fluorescence change with QD size is shown in Figure 1.2.

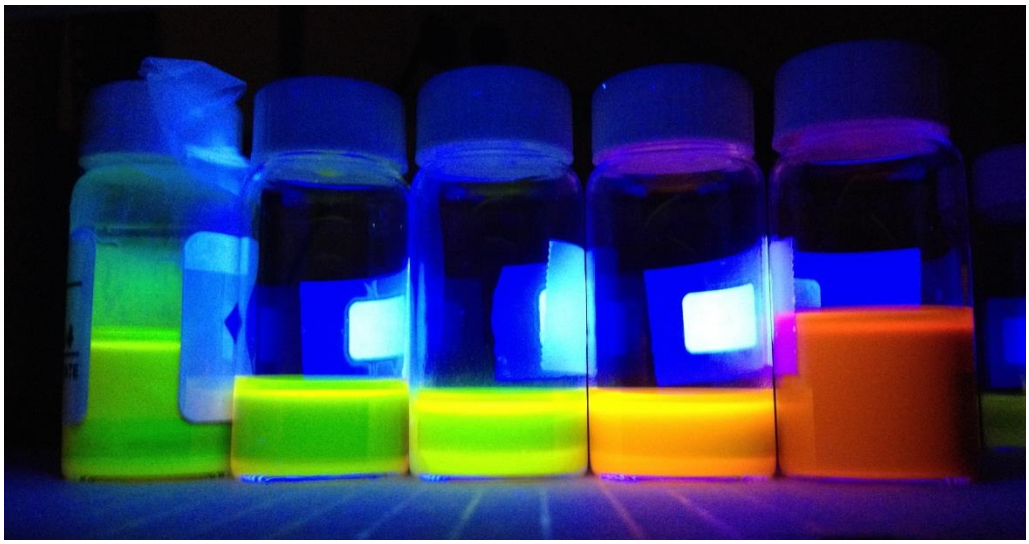

Figure 1.2: A digital photograph of CdSe QDs ranging from ≈ 3 to 5 nm in diameter, excited by a UV light source. QD size increases left to right.

1.1.1 Applications

Owing to their unique size-tunable properties, QDs have been considered for a variety of applications ranging from biodiagnostics to optoelectronics. The tunability of QD electrical and optical properties as well as their capacity for solution-processing allows QDs flexibility over traditional materials in a variety of applications. QDs are of interest in the biomedical imaging world for their high quantum yields, tunable emission wavelengths, stability in various solvents and different pH environments, and their small size.[7-10] Often in these studies, ligands on the surface of the QD are modified to enhance their solubility in water.[11] QDs have also been utilized in solar concentrator devices, which focus incident light onto photovoltaics.[12-16] In these applications, QDs offer easier band gap tuning and improved stability than organic counterparts. Similarly, QDs are of

interest for light waveguiding applications in photonic devices.[17] The broad range of potential band gaps across different QD materials enables access to both visible and near-infrared wavelengths. Another arena seeking to capitalize on the emission tuning of QDs is the world of light-emitting diodes and display devices.[18,19] The high quantum yields attainable for QDs support more efficient devices and QDs approaching monodispersity exhibit a narrow emission spectral bandwidth ideal for displaying very specific spectra. Similarly, QDs offer interesting opportunities for photovoltaics.[20,21] The colloidal synthesis route for QDs and their ability to disperse in a solvent enables scalable processing techniques that are less time-consuming and energy intensive than synthesis and processing of traditional solar cell materials (i.e. single crystal silicon). Additionally, the band gap can be tuned to an optimal energy for solar light absorption. QDs have also demonstrated potential for field-effect transistors.[22] Again, the solution-processing allowed by QDs offers more cost-efficient device design and implementation. Cartoon schematic of two QD devices are given in Figure 1.3.

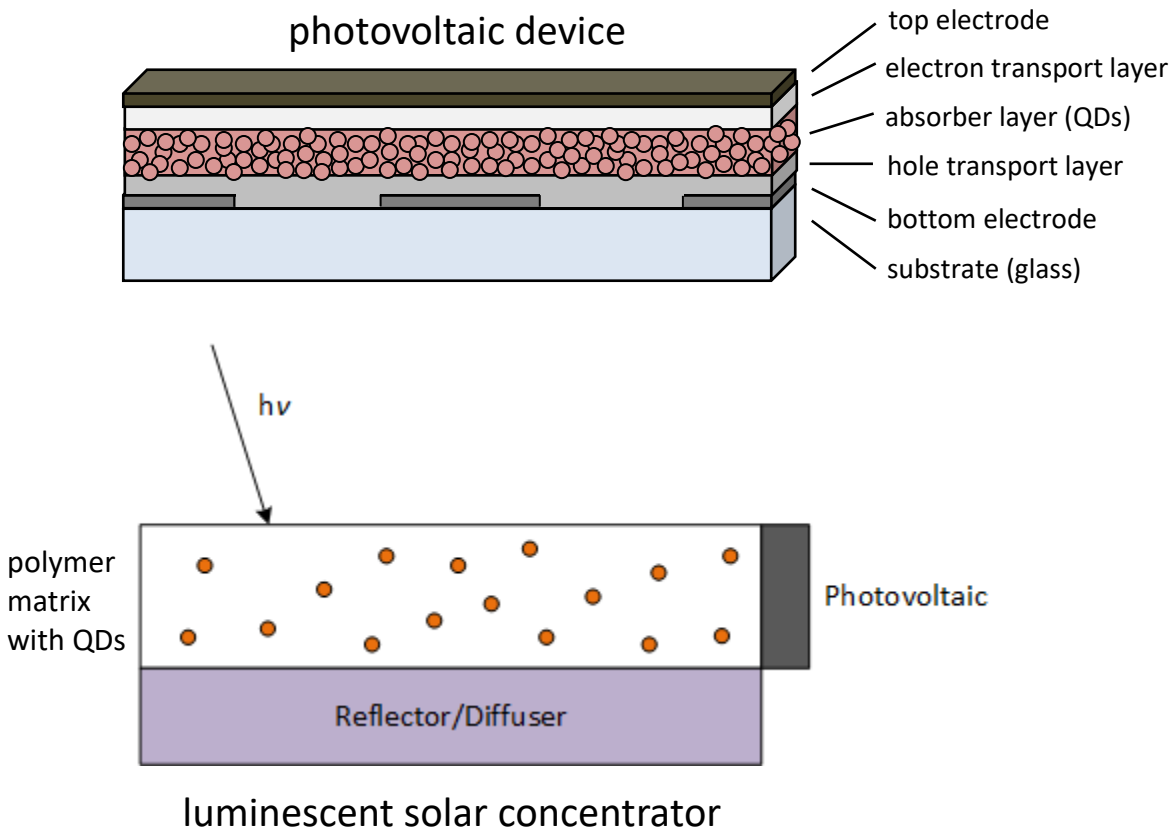

Figure 1.3: Cartoon schematics of a QD photovoltaic device (top) and a luminescent solar concentrator (bottom). The QD absorber layer in the photovoltaic is commonly composed from a film of QDs.

In many of these applications, the quantum dot surface dictates dispersion in solvents (relevant for device construction) and controls electronic coupling between QDs, but it also plays a critical role in the packing of QDs. Solution-based syntheses are common for many QD materials, which require ligands on the surface of the QD to stabilize the nanocrystals during growth and disperse the product in solvents. Similarly, plasma synthesis of QDs can be followed by surface modification to grant QD dispersion in solvents.[23] Although some of the applications given here are based on QDs dispersed in solvents (e.g. bioimaging), the majority relies on thin films or solid bulk structures of QDs. Hence, the nature in which QDs organize into solids is an important consideration

for these applications. The following section addresses the current limitations in QD packing and ordering.

1.1.2 Quantum Dot Ordering

Through modification of the ligands on the QD surface and control over the QD size, a wide range of ordered and disordered QD arrays is attainable. Glassy (amorphous) QD solids are readily prepared from drying QDs from solvent; a variety of factors can induce this behavior, including volatile solvents (i.e. fast drying), polydispersity of QD size, and poor QD dispersion in the solvent.[24] The resulting QD solid is comprised of randomly-packed QDs and is comparable to the dense solids prepared from hard spheres with soft shells.[2]

Given a narrow QD size distribution, QDs can also form ordered superlattices. Many methods employ slow drying rates through careful selection of solvents or utilize liquid or solid interfaces to produce ordered arrays.[2,25] Roughly spherical QDs typically pack in face-centered cubic morphologies, although examples of hexagonally closed packed and even simple hexagonal packing have been observed.[24,26] When the QD has a relatively soft shell (afforded through long ligands), body-centered cubic structures can also be observed.[27] More complex QD structures can be accessed through superlattices composed of more than one size of QDs. Binary nanoparticle superlattices (BNSLs) are composed of two sizes of particles and feature higher packing densities than single-size QD ensembles.[24] BNSLs have exhibited cubic, hexagonal, tetragonal, orthorhombic, and even quasicrystalline symmetries.[2,28-33] An example of a quasicrystal formed from two types of nanoparticles is given in Figure 1.4. In this example, 13.4 nm iron oxide and 5

nm gold nanoparticles (and 9 nm lead sulfide and 3 nm palladium nanocrystals) assemble a dodecagonal quasicrystal structure.[33]

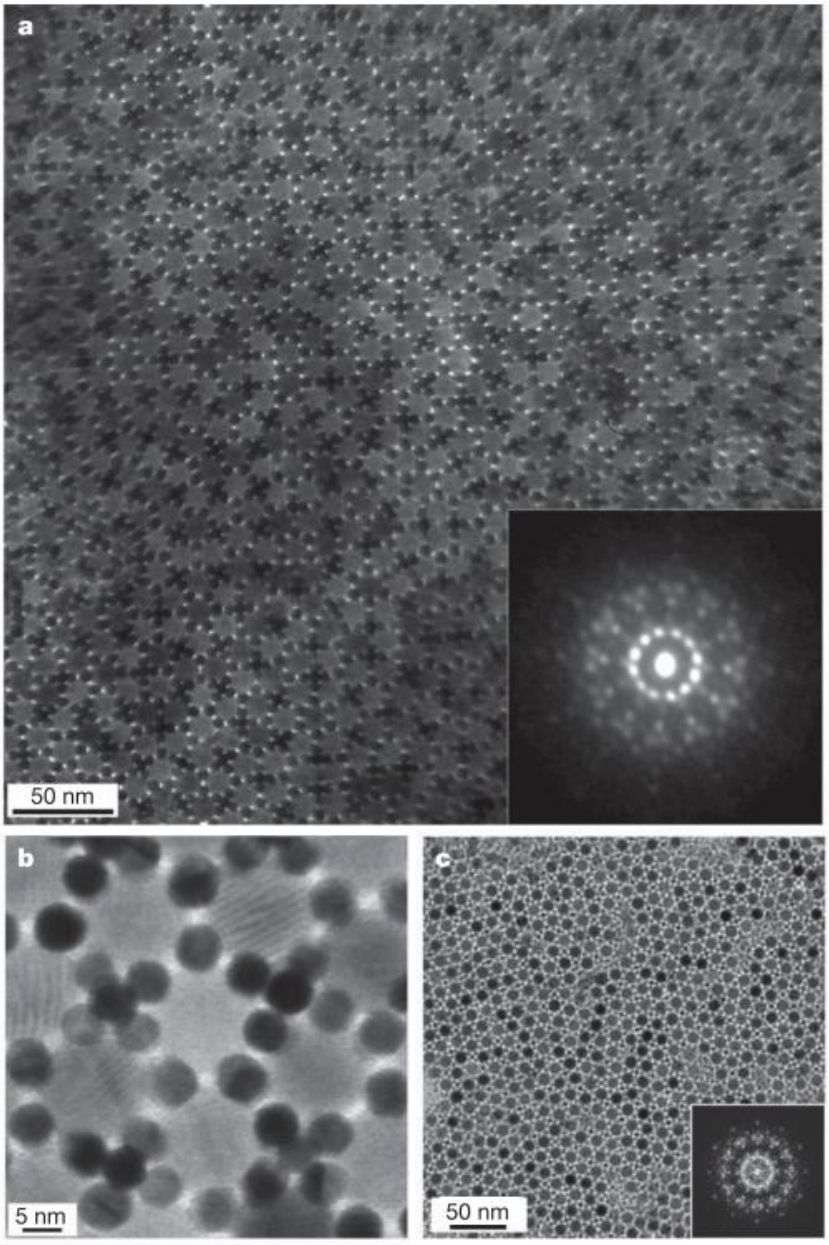

Figure 1.4: Micrographs of dodecagonal quasicrystals formed in two different two-nanoparticle ensembles. In (**a**) and (**b**), 13.4 nm Fe_2O_3 and 5 nm Au nanoparticles exhibit 12-fold rotational symmetry (inset electron diffraction patterns). In (**c**), 9 nm PbS and 3 nm Pd nanoparticles also exhibit a dodecagonal quasicrystal structure with corresponding 12-fold rotational symmetry in the inset fast Fourier transform pattern. These figures were reproduced from [33].

Spacing between QDs in both disordered and ordered arrays is determined by the ligands on the QD surface. As such, the distance between particles can be manipulated via ligand exchange to ≈ 2-20 nm spacing between edges of QDs.[27,34] However, more complex and larger-scale ensembles are difficult to achieve with particles and attached ligands alone. A broad range of these opportunities are perhaps attainable via the integration of QDs in polymer matrices.

Section 1.2 – Quantum Dot–Polymer Composites

QD-polymer and nanocrystal-polymer composites have been of interest for over a century. Originally, the impact of small particles on a polymer's mechanical properties was the driving question. Upon addition of mica, nylon was found to exhibit a five-fold increase in tensile and yield strength, while microparticles incorporated in rubber modified the rubber's elasticity.[35-37] More recently, the composites have been considered from an opposing viewpoint: how the polymer matrix might provide stability for nanoparticles and enable unique QD ordering through the rich variety of polymer phase morphologies.[38,39] The scale of sizes accessible via polymer ordering is immense compared to neat particles: while QDs are typically 2-10 nm in diameter and pack on similar length scales, polymers feature morphologies that range from 10s to 100s of nm in unit cell length.

1.2.1 Polymer Phase Behavior

Polymers are molecules composed of repeat units. Block copolymers are comprised of two or more different polymer chains chemically bound together. This

covalent bond between thermodynamically incompatible polymer components prevents macrophase separation, but results in periodic structure through polymer microphase separation.[40,41] These structures arise from the balance of enthalpic penalties of interfacial contact between polymer components and entropic penalties of polymer chain stretching. The phase behavior of A-B block copolymers is tuned through a variety of parameters including the degree of polymerization, *N*, the volume fraction of block A, f_A, (f_A = 1- f_B) and the Flory-Huggins interaction parameter, χ. (In more complex systems, the phase behavior is also a result of the conformational asymmetry of the block copolymers, related to the pure component densities and Kuhn statistical lengths).[42] When there is insufficient experimental data, χ between polymer components A and B is often estimated:

$$\chi_{AB} = \frac{V_{ref}}{RT}(\delta_A - \delta_B)^2 \tag{1.1}$$

where V_{ref} is the polymer segment reference volume, T is the temperature, and δ_A and δ_B are the Hildebrand solubility parameters of components A and B. The product χN (where $N = N_A + N_B$) governs the resulting polymer phase. At low values of χN, entropic forces dominate and the polymer state is disordered; as χN exceeds 10.5, ordered polymer morphology arises.[43] The morphology adopted by the block copolymer is controlled primarily by the volume fraction of a given polymer component, *f*. An example of a theoretical phase diagram compared to a diagram composed from experimental measurements is given in Figure 1.5. As temperature rises, the value of χ decreases; thus, as temperature is increased, ordered polymer phases turn into a disordered phase.

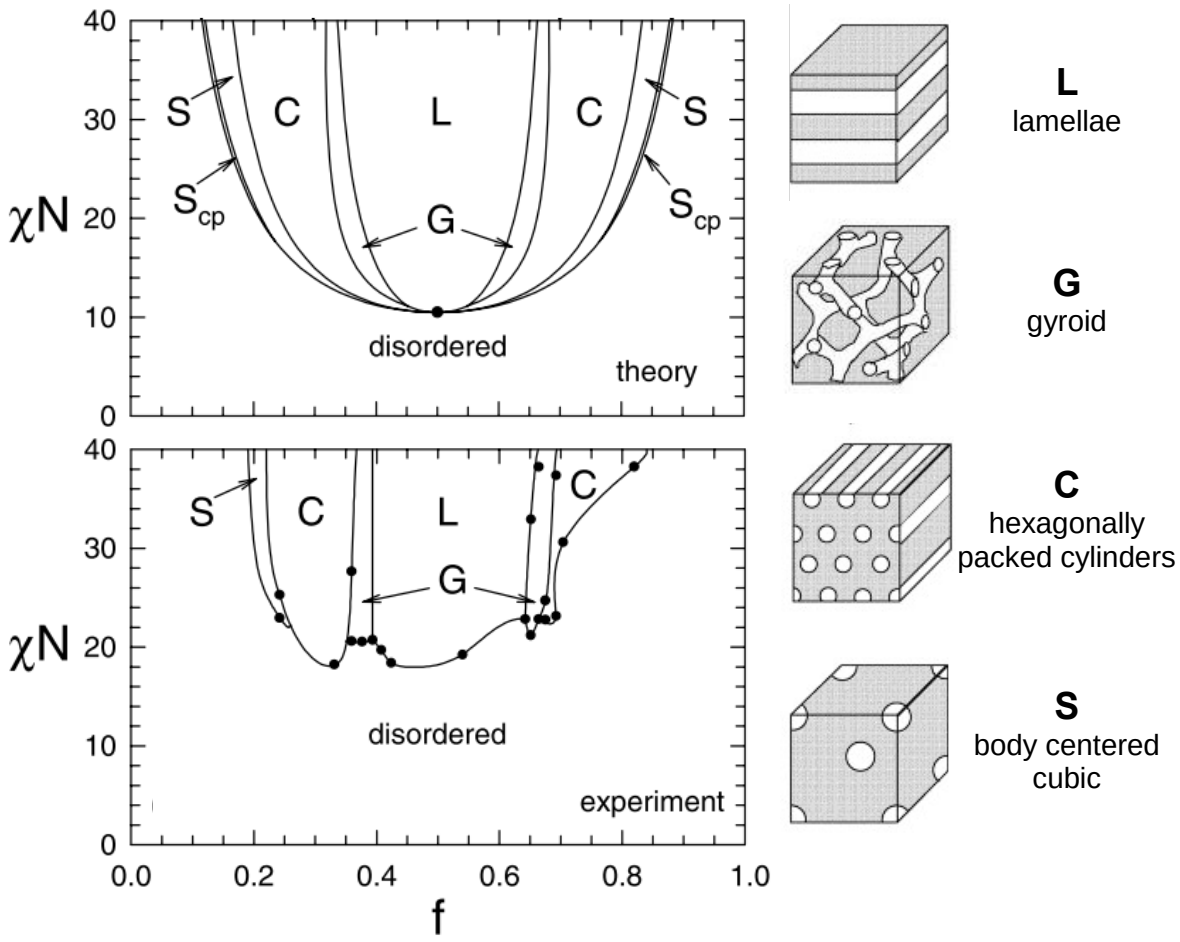

Figure 1.5: Theoretical and experimental phase diagrams for poly(styrene-*b*-isoprene). The theoretical diagram is calculated using self-consistent field theory. Examples of the phase morphology are shown in cartoon form on the right with corresponding labels. Figures were reproduced from [44,45].

Some polymers exhibit additional, more complex phases including Frank-Kasper and quasicrystalline morphologies.[46-48] Quasicrystals exhibit rotational symmetry but lack translational symmetry, making them unique candidates for applications in photonics, heat insulating materials, and brittle but hard and low friction coatings.[49-52] Examples of some of these morphologies are presented in Figure 1.6.

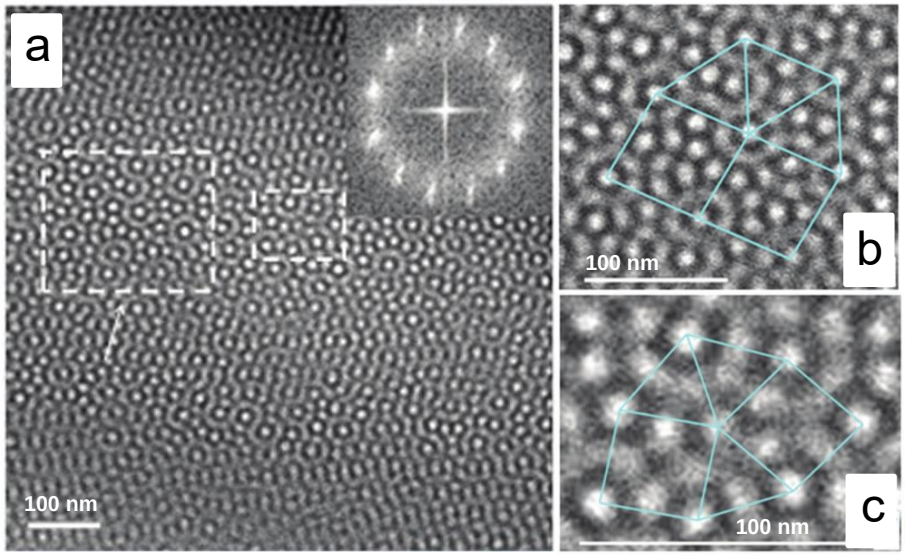

Figure 1.6: TEM micrographs of a poly(styrene-*b*-isoprene-*b*-styrene-*b*-ethylene oxide) tetrablock terpolymer stained with osmium tetroxide (OsO_4). (**a**) Although no long-range translational order is apparent, 12-fold rotational symmetry is revealed in the inset Fourier transform, consistent with dodecagonal quasicrystalline order. (**b**) A section of the film is highlighted to demonstrate the H Frank Kasper phase ordering (quasicrystal approximant). (**c**) Another section is highlighted to show the σ Frank Kasper phase (another quasicrystal approximant). Images were reproduced from [48].

1.2.2 Nanoparticle-Polymer Composites

The rich breadth of polymer phases offers new opportunities for organizing QD composites. If QDs can be effectively localized to specific regions of a given polymer phase, complex ordering of QDs across a range of length scales may be achieved. Polymer phase domain size scales as $L \sim \chi^{1/6} N^{2/3}$ for lamellar, hexagonally closed packed cylinders, and body-centered cubic morphologies; thus, as the polymer chain length increases, the domain size increases. In practice, polymers ranging from < 1 kg/mol to several hundreds of kg/mol can be prepared, allowing access to a large range of domain sizes.

In practice, there are three common methods for nanoparticle integration in polymer matrices:

1. Nanoparticle synthesis *in situ* in a polymer[53-59]
2. Polymer synthesis from a dispersion with nanoparticles already incorporated[60-64]
3. Co-assembly of separately synthesized nanoparticles and polymer[65-69]

Method (1) is commonly coined the 'microreactor' approach: a nanoparticle precursor is loaded into the polymer matrix and often confined to one polymer domain. The nanoparticles are grown with the addition of another reactant (often in gas form), or via heating and reaction with functional groups on the host polymer.[70] The resulting particles are often only kinetically localized; thus, particle movement and aggregation is not uncommon. Additionally, it is difficult to control the nanoparticle growth via this method, which usually leads to many small and polydisperse nanoparticles.[39] This approach is limited to compatible chemistries of nanoparticle and polymer materials.

Method (2) is also limited to compatible reaction chemistries. UV-activated polymer chemistries are frequently used in this method as they typically do not affect the incorporated nanoparticles' properties.[15,71] The resulting composites usually exhibit randomly-dispersed nanoparticles. This method is more common for growing homopolymers rather than block copolymers around nanoparticles.

Method (3) is reliant on thermodynamics to successfully incorporate nanoparticles in a polymer matrix. Typically, the nanoparticles are stabilized with surface ligands that are selected for their favorable enthalpic interactions with the host polymer or one of the host polymer components. Furthermore, entropic constraints of polymer chain packing affect the localization of nanoparticles in the polymer matrix. Due to the universality of this approach for different polymer and nanoparticle chemistries, this method was chosen for the work presented in this thesis.

Section 1.3 – Motivation and Thesis Overview

The dispersion of nanoparticles or QDs in a polymer matrix is dictated by the competition of enthalpic interactions between ligands on the particle surface and a given polymer component and entropic constraints of polymer chains packing around solid particles.[72,73] Experimental and theoretical studies often attempt to explain behavior based on the enthalpic driving forces (polymer-ligand chemistry) and the entropic driving forces (particle size compared to polymer domain size or chain size).[74]

QD dispersion in a polymer matrix is affected by the enthalpic interaction between the ligands on the QD surface and the polymer component in theoretical and experimental studies. When the ligands have no affinity for either polymer component or have a relatively equivalent affinity for both polymer components in a block copolymer, nanoparticles populate the interface between polymer components.[75] If the ligands have significant affinity for only one of the polymer components, the nanoparticles are localized in that component's subdomain.[69,76] An example of this is given in Figure 1.7. In the latter case, ligand length plays an additional role in dictating the placement of nanoparticles inside the preferred polymer subdomain: nanoparticles with long and densely packed ligands are mainly confined to center of the subdomain. When the ligands on the nanoparticles' surfaces are shorter and less dense, the nanoparticles are more commonly found distributed throughout the subdomain.[77] However, it can be difficult to overcome particle aggregation in some cases, as saturated alkane ligands experience enthalpic gain with ligand packing, resulting in nanoparticle aggregation.[78]

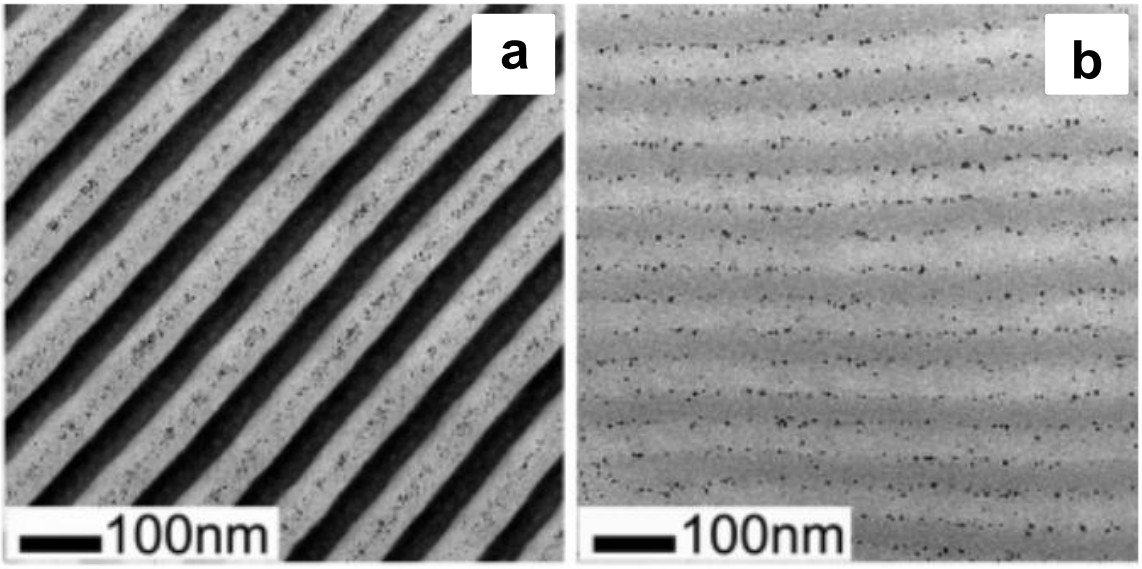

Figure 1.7: TEM micrographs of gold nanoparticles in a poly(styrene-*b*-2 vinyl pyridine) diblock copolymer. (**a**) Gold nanoparticles with polystyrene ligands prefer the center of the polystyrene domains. The poly(2 vinyl pyridine) domain is stained by iodine. (**b**) Gold nanoparticles with a mixture of polystyrene and poly(2 vinyl pyridine) ligands prefer the interface between polymer domains. Images were reproduced from [69].

Favorable enthalpic interactions between ligands on the nanoparticle's surface and a polymer component are insufficient for nanoparticle dispersion in the polymer matrix. The polymer's loss of conformational entropy when forced to fill space near a nanoparticle surface can outweigh the enthalpic gains of ligand-polymer interactions, and result in nanoparticle aggregation. One solution is to help preserve some of the polymer's conformational freedom near the nanoparticle surface with lower ligand density near the edge of the nanoparticle, as is common for 'brush' forming ligands.[72]

The relative size of the nanoparticles in comparison to the polymer domain size also affects nanoparticle dispersion. When the particles are considerably smaller than the targeted polymer subdomain size, the polymer can more readily accommodate the particle volume without severe chain packing penalties.[73,79] As the particle size

approaches the polymer subdomain size, the polymer encounters dramatic conformational entropic penalties for accommodating a hard object, which induces particle aggregation to minimize these packing constraints. Nanoparticles have been shown to localize in the center of a polymer subdomain when the particle size is considered 'large,' and are otherwise randomly dispersed across a polymer subdomain when the particle size is considered 'small.' The designation of 'small' versus 'large' nanoparticles has been cited to range anywhere from a d/L ratio of less than 0.2 to greater than 0.4 where d is the particle diameter and L is the polymer domain length.[66,73,80]

Experimentally, the number of parameters influencing the dispersion of QDs in polymer matrices is large, which makes it difficult to make generalized statements on dispersity. There still remains much to be understood about the factors dictating nanoparticle dispersion and aggregation in polymer matrices. In this work, I sought detailed experimentation of new approaches for integration of QDs in polymer matrices. This thesis is broken into four additional chapters describing the various efforts made towards this goal:

In chapter two, I review the development of a robust synthesis technique for well-stabilized quantum dots in nonpolar solvents. The important characterization techniques for QDs including optical properties, crystal structure, QD size, dispersity in solvents, and packing in dried films, are reviewed and presented with representative data of the many batches of QDs made throughout this project.

In chapter three, I discuss the first approach considered for QD integration in polymer matrices: ligand exchange. Native ligands from QD synthesis were exchanged for a thiolated poly(ethylene glycol) chain to enable QD dispersion in polar solvents. The

extent of ligand exchange is qualitatively and quantitatively analyzed, with discussion on the resulting effect of QD stability in various solvents.

In chapter four, I communicate the extent of QD integration in homopolymer films. Three examples are given: QDs with native ligands integrated in poly(lactic acid) and poly(butadiene) matrices, and QDs with poly(ethylene glycol) ligands integrated in poly(lactic acid). The extent of QD dispersion is evaluated and the resulting implications for QD integration in different polymer chemistries are discussed. Enthalpic forces between ligands on the QD surface and the host polymer affect the extent of QD dispersion in the homopolymer matrices.

In chapter five, I review the results of attempted QD integration in block copolymer matrices. Three different polymer chemistries are examined for QD dispersion: poly(ethylene-*b*-cyclohexylethylene), poly(styrene-*b*-butadiene), and poly(lactic acid-*b*-butadiene), and two composite preparation techniques are explored. The extent of QD dispersion in polymer composites is evaluated and discussion on potential improvements to an innovative integration method using the inversion of polymer micelles follows.

Chapter Two - Quantum Dot Synthesis

In this chapter, the synthesis and characterization of cadmium selenide (CdSe) quantum dots (QDs) will be discussed. CdSe QDs are among the most well-studied quantum dots and exhibit high fluorescence yields, which enables their use in optical applications. Furthermore, CdSe QDs are small (2-6 nm in diameter) and various sizes may be prepared by solely changing reaction time.[81] These characteristics lend themselves well to polymer matrices featuring small size domains. The main objective was to ensure a robust and repeatable synthesis procedure of QDs that maintained stable dispersions in nonpolar solvents. The crystal structure, QD shape and size, and stability were all evaluated for consistency. The quantum dots reported here were used in the experiments described in later chapters. Small portions of this chapter are copied from the author's work published in Langmuir.[82]

Section 2.1 - Synthesis Procedure

2.1.1 Materials

Cadmium oxide (CdO) (99.999% purity) from Strem Chemicals, trioctylphosphine (TOP) (97% purity) and selenium pellets (~2 mm, ≥99.999% purity) from Sigma Aldrich, trioctylphosphine oxide (TOPO) (99% purity) from Acros Organic, and octadecylphosphonic acid (ODPA) (97% purity) from Alfa Aesar were all used as purchased.

2.1.2 Colloidal CdSe QD Synthesis

Cadmium selenide quantum dots were synthesized via a hot-injection reaction in a nitrogen environment.[81] Various similar procedures were evaluated for consistency in quantum dot synthesis[83-85] and the following procedure was found to be most repeatable.

Three grams of TOPO, 280 milligrams ODPA, and 50 mg of CdO were added in air to a three necked flask. The flask was connected to a Schlenk line and heated to 40-50°C under stirring to allow the materials to melt before undergoing three vacuum-nitrogen cycles to purge air from the flask. During these cycles, the temperature was gradually raised to 150°C, at which point it was kept under vacuum for an hour to pull off water and air. During this time, a syringe of 1 mL of TOP and 0.5 mL of 1.52 M selenium in TOP (TOPSe) were prepared in a nitrogen glovebox. The TOPSe was typically prepared days to months ahead of time by mixing 1.8 g of selenium pellets in 15 mL of TOP and stirring until the pellets dissolved (several hours to days). After one hour at 150°C under vacuum, the three necked flask containing TOPO, CdO, and ODPA was introduced to nitrogen again and the temperature was raised to 320°C over the course of 10-20 minutes. At this temperature, the CdO is complexed by the TOPO and ODPA, evidenced by the red-brown opaque solution turning clear and colorless. Once the solution was clear, the syringes containing TOP and TOPSe were removed from the glovebox and the 1 mL of TOP was injected into the three necked flask. The temperature was then raised to 370-380°C over the course of a few minutes, at which point the TOPSe solution was swiftly injected into the flask. Upon the injection of the TOPSe, nucleation occurs followed by a period of quantum dot growth. To achieve particles of the same size, the nucleation events should occur almost simultaneously. Thus, it is imperative for

the injection to be swift and under considerable stirring to distribute the TOPSe evenly across the solution as fast as possible.

The reaction was quenched 0-2 minutes after TOPSe injection by removing the heating mantle and squirting acetone on the outside of the flask. The reaction was almost immediately evident by the solution turning from colorless to yellow, orange, and then red. The solution reacted quickly at T > 350°C but continued to slowly change color until the temperature reached somewhere in the mid 200s°C. When the solution was cooled to ≈150°C, the flask was lowered into a water bath to continue cooling. Upon reaching ≈70°C in the flask, the water bath was removed, stirplate stopped, and the reaction contents were transferred to a centrifuge tube.

2.1.3 Synthesis Procedure Variations

When the reaction was allowed to proceed for longer times to make larger quantum dots (diameter > 3.5 nm), the final product was prone to aggregation. With the assistance of Luis Sosa, the procedure was modified to test for better stability of larger quantum dots. Through a series of experiments, it was determined that increasing the amount of ODPA to 373 mg (1.3× the original 280 mg) yielded a more stable product at reaction times exceeding 20 s. CdSe QDs prepared with extra ODPA at longer reaction times (> 20 s) were less prone to aggregation than those prepared with 280 mg ODPA. This difference is attributed to the role that ODPA plays in complexing Cd and in breaking down TOPSe. Increasing the amounts of TOP and TOPO had no beneficial effect on the stability of the product.

Section 2.2 - Cleaning after Synthesis

The resulting product dispersion containing the largest dots (those synthesized for 20−120 s) was transferred into a centrifuge tube and acetone was added as an antisolvent until the dispersion turned turbid. The turbid dispersion was centrifuged for 8−10 min at 4000 rpm. After centrifugation, the supernatant was discarded and the solid product was redispersed in hexane before repeating the same acetone addition and centrifugation cycle twice more. For smaller QDs, 5 mL of toluene was added to the reaction flask at approximately T = 100°C as it cooled to ease product recovery. The resulting product dispersion was transferred into a centrifuge tube and centrifuged for 8−10 min at 4000 rpm after adding 10−15 mL of ethanol as an antisolvent. After centrifugation, the supernatant was discarded and 5 mL of toluene was added to the precipitate to redisperse the product. The ethanol addition and centrifugation were repeated a second time before redispersing the QDs in hexane. In the final cleaning step, acetone was added to the quantum dots dispersed in hexane until the dispersion turned turbid. This turbid dispersion was centrifuged at 4000 rpm for 8−10 min. If the dispersion did not separate after any given centrifuge cycle, additional antisolvent was added and the mixture centrifuged until the QDs separated from the solvents.

2.2.1 Storage and Separation

The end product was typically still high in excess ligand concentration after cleaning and centrifugation cycles. When allowed to rest undisturbed over time, the QD product commonly split into two layers. The top layer was colored and transparent and contained stabilized particles. The bottom layer was colored but opaque and contained aggregated particles and excess ligands. This separation typically occurred over the

course of a couple days to a couple weeks. Once the layers separated, the top layer was stable and well-dispersed for years at a time. Additional washing steps immediately after synthesis sometimes reduced the amount of aggregated material in the bottom layer but more commonly led to increased aggregation problems. Upon each cycle of washing, more ligands are removed from the solution. If the solution is washed too vigorously, the particles shed ligands, which ultimately led to particle aggregation. In general, performing one to three washing steps typically led to a stabilized product with a bottom aggregated layer. Occasionally, a dispersion would appear the same, visually, with two separated layers, but dynamic light scattering revealed that the top layer was aggregated. In these cases, further washing steps at this stage did not effectively separate aggregated particles from unaggregated particles.

All QD samples were stored dispersed in a solvent - typically hexane but occasionally toluene - where the vials were capped in air. To better preserve QD fluorescence properties, the QDs can instead be stored under an inert gas to prevent surface oxidation. When performance is the main objective, a core-shell QD structure where a protective coating is grown over the CdSe core (often CdS or ZnS) is preferred.[86-88] For this work, fluorescence efficiency is less critical and thus CdSe QDs were sufficiently robust.

Section 2.3 - Characterization

There are a myriad of techniques available for evaluating the end product QDs;[2] here, the relevant techniques are briefly described and demonstrated. QD size is determined by absorbance, small angle x-ray scattering, and TEM, the latter two of which

also reveal QD shape. The QD crystallinity is found via wide angle x-ray scattering. QD fluorescence is also evaluated using a fluorometer and/or microscope. The ligands on the QD surface are studied via Fourier transform infrared spectroscopy. QD stability in various solvents is determined with dynamic light scattering.

2.3.1 Absorbance

The band gap of the QDs can be determined by their first absorption peak energy. Jasieniak *et al.* relate the QD diameter to the absorption peak by

$$D = 59.60816 - 0.54736\lambda + 1.8873 \times 10^{-3}\lambda^2 - 2.85743 \times 10^{-6}\lambda^3 + 1.62974 \times 10^{-9}\lambda^4 \quad (2.1)$$

where D is the QD diameter in nm and λ is the first absorption peak wavelength in nm.[89] The Beer-Lambert law can also be arranged to extract the concentration of QDs in dispersion:

$$[CdSe] = \frac{Abs}{l\varepsilon} \times \frac{\Delta E_{HFHM}}{0.06} \quad (2.2)$$

where $[CdSe]$ is the concentration of CdSe QDs in molar, Abs is the intensity of absorbance at the first absorption peak, l is the path length of the sample in cm, ε is the molar extinction coefficient in $M^{-1}cm^{-1}$, and ΔE_{HFHM} is the half-width-half-maximum of the first absorption peak in eV on the low energy, or high wavelength, side. The molar extinction coefficient is determined by

$$\varepsilon = 155{,}507 + 6.67054 \times 10^{13} \exp\left(\frac{-E_1}{0.10551}\right) \quad (2.3)$$

where E_1 is the first absorption peak energy in eV.

Optical absorption of the QDs dispersed in toluene, hexane, or chloroform was recorded using a Cary 5000 UV-vis spectrophotometer. Absorbance of the QDs was

determined by subtracting the absorption of the neat solvent in a quartz cuvette from that of the QDs dispersed in the same solvent in the same cuvette. Example absorbance of CdSe QDs in hexane is given below in Figure 2.1.

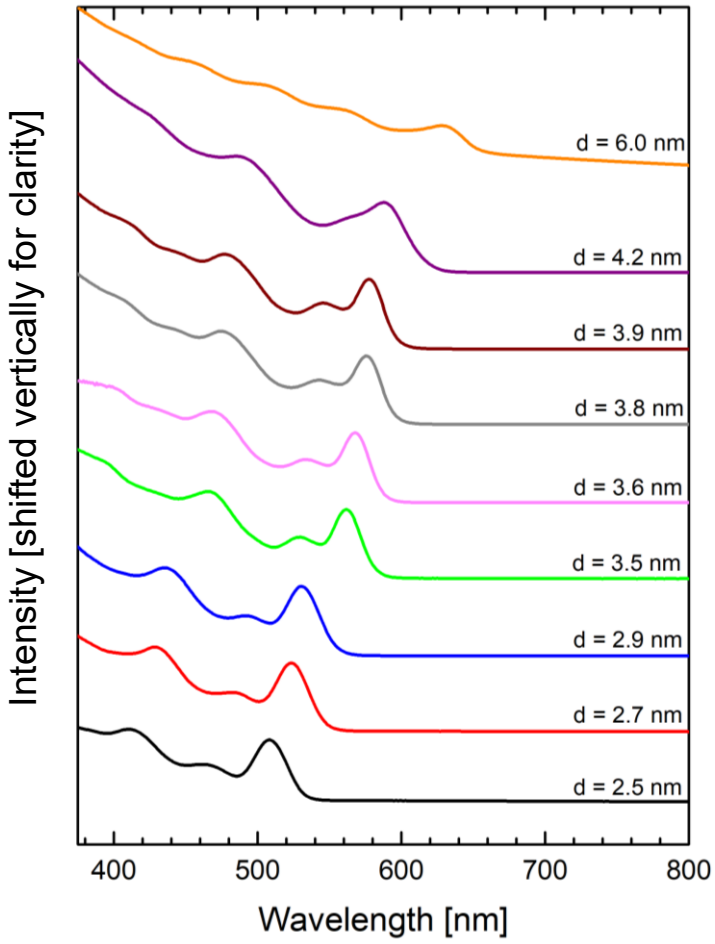

Figure 2.1: Absorbance of various CdSe QD samples in hexane. The QD diameters listed are as calculated from Eqn. 2.1 and the absorption peak wavelength.

Note that some absorption curves demonstrate additional peaks at lower wavelength or higher energy. These are secondary excitation peaks, which become prominent when the sample is monodisperse. In general, the narrower the primary peak, the more monodisperse the sample is.

2.3.2 Fluorescence

CdSe QDs fluoresce when excited with energy above the band gap. When a QD absorbs high energy light, an electron is excited from the valence band to the conduction band, leaving behind a hole. This energy can be emitted as light when the electron and hole recombine. Defects such as trap states on the surface of the QDs can lead to lower fluorescence or "blinking" by enabling non-radiative decay pathways for the exciton.[90] Experimentally, the excitation energy should be chosen to be higher than the first absorption peak energy and high enough to avoid overlap of the incident excitation beam and the fluorescing sample peak.

Fluorescence of the QDs dispersed in hexane or chloroform was measured using a Photon Technology Inc. (PTI) fluorometer; fluorescence of QD thin films and QD-polymer composite films were studied using a Zeiss Axio Observer D1M microscope. The excitation wavelength for fluorescence was chosen between 480 and 520 nm, depending on the QD size. An example of CdSe QD fluorescence and absorbance (for comparison) in hexane is given below in Figure 2.2.

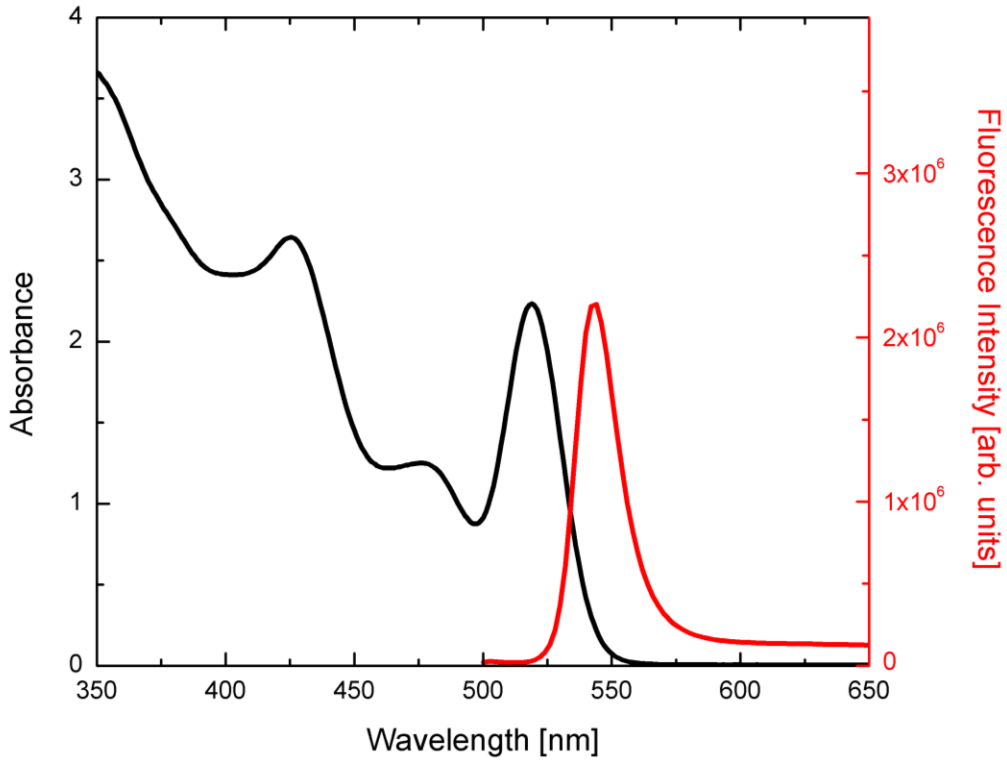

Figure 2.2: Absorption (left) and fluorescence (right) of CdSe QDs in hexane. From the absorption peak, d = 2.7 nm.

2.3.3 Fourier Transform Infrared Spectroscopy

Fourier transform infrared spectroscopy (FTIR) is instrumental in identifying ligands present on or near the surface of QDs by measuring the rotational and vibrational energy of bonds in the infrared region. Ligand coverage on the QD surfaces was determined using a Nicolet Magna 550 spectrophotometer equipped with a Harrick Scientific Horizon Attenuated Total Reflectance-FTIR attachment. To measure the spectra of neat, unbound ligands, TOPO was dispersed in hexane and dropcast onto a 1 cm × 5 cm × 0.2 cm germanium trapezoidal ATR crystal with 45° beveled edges. Spectra were taken as the solution dried on the crystal to monitor the solvent absorption peaks. TOP is a liquid at room temperature and thus was directly deposited on the ATR crystal and spectra taken immediately. The neat ligands were compared to the spectra obtained

from a concentrated solution of QDs in hexane as the QDs dried from dispersion. All infrared spectra were taken with reference to the bare ATR-FTIR crystal.

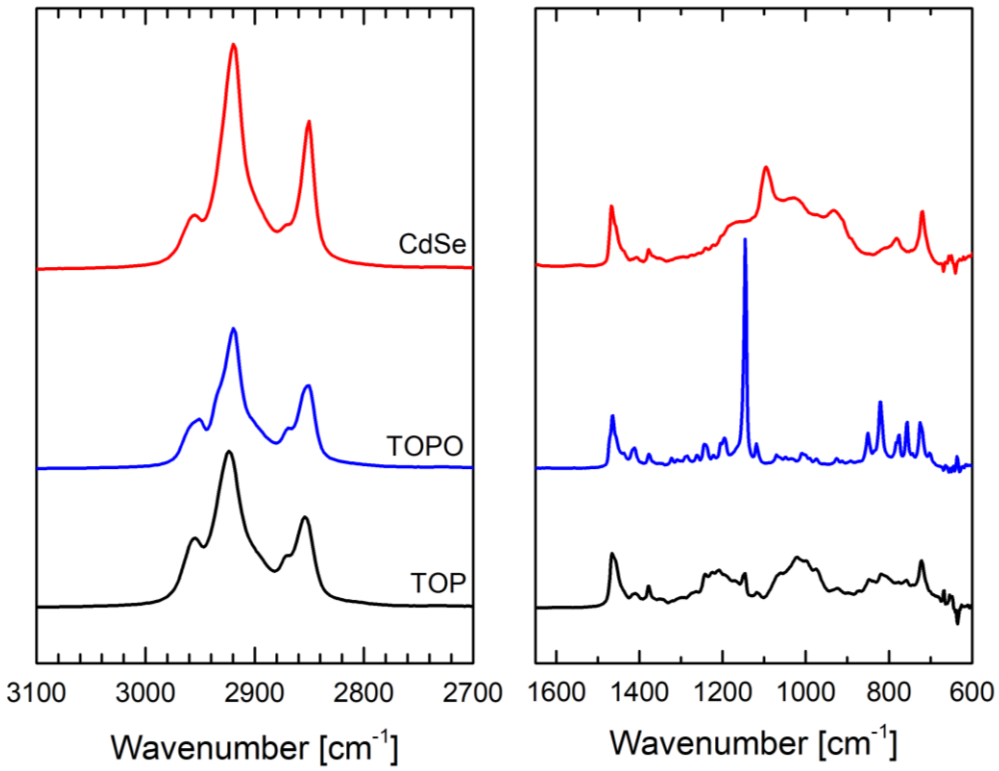

Figure 2.3: FTIR spectra of TOP, TOPO, and CdSe QDs at low and high wavenumbers.

The spectra of TOP and TOPO (shown in Figure 2.3) both display C-H stretches at 2852 cm^{-1} and 2921 cm^{-1} and these same modes are apparent in the QD sample. The P=O stretch of the neat TOPO at 1144 cm^{-1} is narrow. In the QD sample, this peak shifts and broadens, which is indicative of the TOPO binding and coupling to the QD surface.[91-94] The absence of an appreciable peak at 1144 cm^{-1} indicates that most, if not all, of the TOPO observed in the QD sample is bound to the surface, and not free.

2.3.4 Small and Wide Angle X-Ray Scattering

X-ray scattering reveals structural information about the QDs.[2] Small angle x-ray scattering (SAXS) can reveal QD shape and size and polydispersity. The intensity, $I(q)$, of non-interacting particles is given by

$$I(q) = N(\rho - \rho_o)^2 F^2(q) \tag{2.4}$$

where N is the number of particles, ρ is the electron density of the particles, ρ_o is the electron density of the medium, and $F(q)$ is the particle form factor for a given scattering vector q. For monodisperse spheres, $F(q)$ is given by

$$F(q) = \frac{4}{3}\pi R^3 \left(3\frac{\sin(qR) - qR\cos(qR)}{(qR)^3}\right) \tag{2.5}$$

where R is the sphere radius. The scattering vector is given by

$$q = \frac{4\pi}{\lambda}\sin(\theta) \tag{2.6}$$

where λ is the x-ray wavelength and θ is the angle between the incident x-ray and the scattering planes. Figure 2.4 shows SAXS and wide angle x-ray scattering (WAXS) patterns of CdSe QDs dispersed in toluene. SAXS and WAXS patterns were obtained from the DND-CAT 5-ID-D beamline at Argonne National Laboratory.

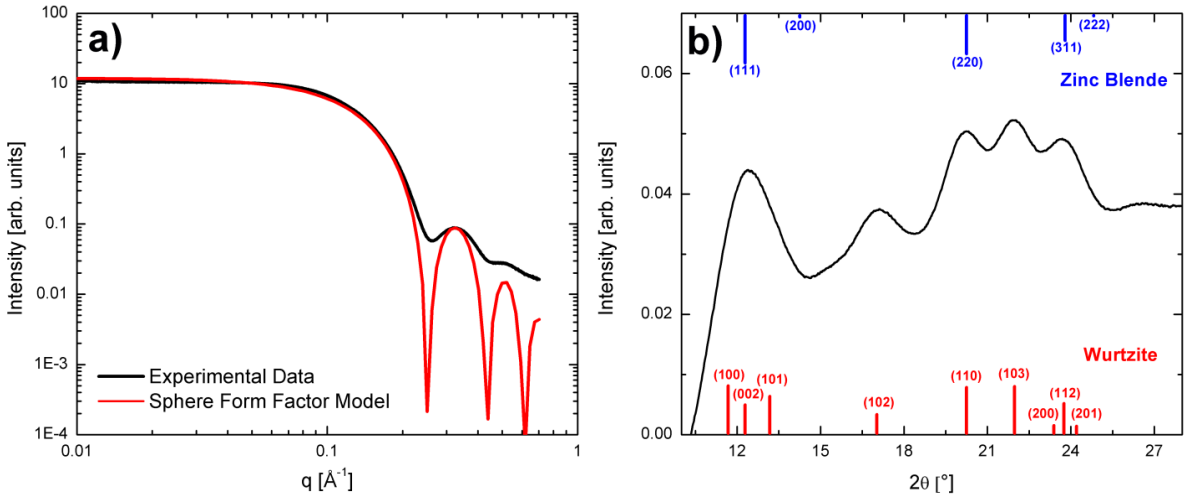

Figure 2.4: (**a**) SAXS and (**b**) WAXS spectra of CdSe QDs in toluene. In (**a**), the SAXS data is modeled used a single size sphere form factor. In (**b**), the WAXS data is shown with expected peaks for zinc blende and wurtzite crystal structures, where the line lengths indicate relative expected intensity.

When fit with Eqn. 2.4, the SAXS data in Figure 2.4 gives R = 1.77 nm. The peaks in the data are broadened in comparison to the model due to small polydispersity in QD size.

WAXS reveals the crystalline structure of QDs. CdSe QDs can grow in zinc blende or wurtzite crystal structures. The WAXS pattern in Figure 2.4 matches well with the most prominent wurtzite peaks, including the (102) and (103) peaks, and correlates with XRD patterns reported in other works.[25,95-98] This is the expected crystal structure for the high temperature synthesis reported here. In general, a mixture of zinc blende and wurtzite crystals is common in most QD syntheses; the relative ratio of the two can be controlled by precursor choice and reaction temperature.

2.3.5 Transmission Electron Microscopy

Transmission electron microscopy (TEM) allows access to important spatial information on scales as small as Angstroms. TEM is used to probe QD size and shape, and at sufficient resolution, can also be used to image crystal lattices.[99] In this work,

TEM was used to identify QDs and construct a spatial understanding of QD-polymer composites.

QD TEM samples were prepared by dropcasting a small amount (typically 2 uL) of dilute dispersions of QDs in hexane onto copper TEM grids or copper TEM grids coated with a thin sheet of carbon or a sheet of lacey carbon. While most samples were allowed to dry freely in air, this process can be slowed down to allow better ordering of QDs on the TEM grid by using a less volatile solvent to disperse the QDs and/or maintaining a solvent vapor pressure by allowing the grid to dry in partially enclosed space. Figure 2.5 shows some examples of TEM images of CdSe QDs synthesized in these studies.

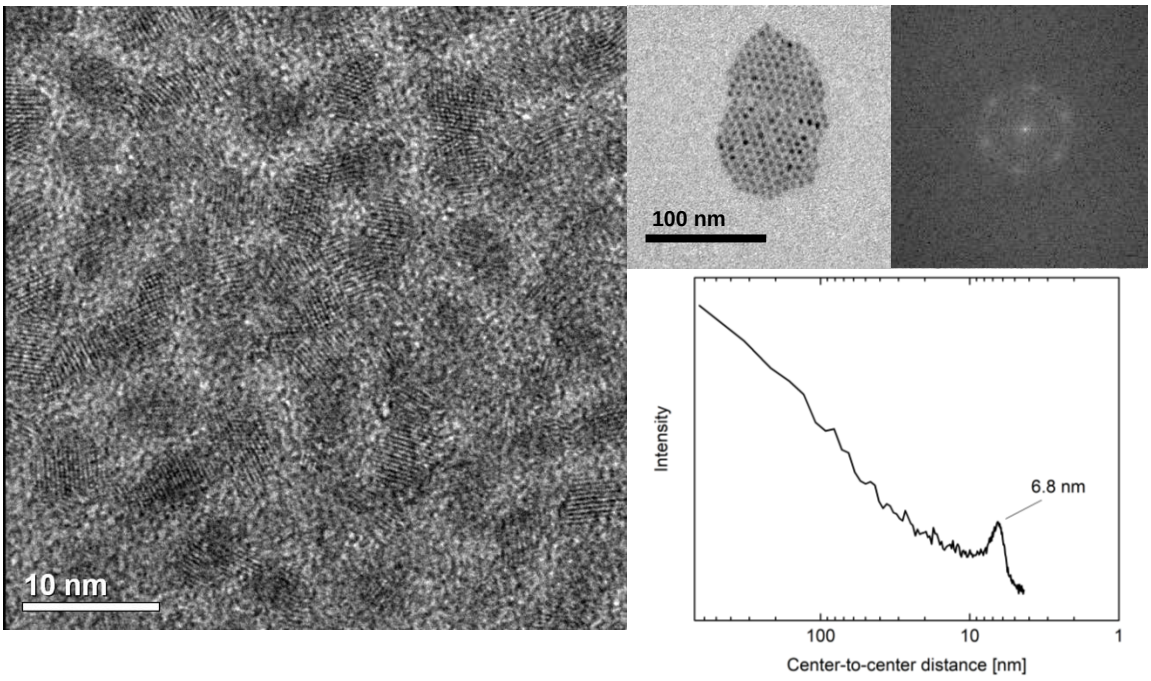

Figure 2.5: TEM images of CdSe QDs. On the left are large (d ≈ 5.5 nm) QDs with visible lattice fringes. On the right, ordered QDs (d ≈ 4.7 nm), as confirmed in the corresponding FFT. The center-to-center distance between QDs is plotted below, with a peak at 6.8 nm.

At sufficient resolution, the images of larger QDs show lattice fringes, which confirm crystalline order. Limitations in instrument resolution make it difficult to confirm similar lattice fringes in smaller QDs. The Fourier transform of the ordered QD assembly reveals a pattern consist with face centered cubic or hexagonally close packed structures. The Fourier transform can be radially averaged to estimate the center-to-center distance between QDs. On average across multiple images, for QDs roughly 4.7 nm in diameter, this center-to-center distance is ~6.8 nm. The spacing between QDs is attributed to the space occupied by the ligands on the surface of the QDs. The longest ligand, TOPO, can be estimated as roughly 1 nm long, given its chemical structure. The expected center-to-center distance is roughly (2 × QD radius) + (2 × ligand length), or 6.7 nm in this case, thus, closely matching the observed value in TEM.

2.3.6 Dynamic Light Scattering

Dynamic Light Scattering identifies the hydrodynamic radius of particles in dispersion. Light passed through the dispersion scatters off of the particles and interferes constructively or destructively with light scattered by nearby particles. As the particles undergo Brownian motion, the subsequent scattered light contains information about the time scale of this movement. The resulting intensity versus time data gathered by the instrument can be autocorrelated to generate a decay function indicative of the relevant time scale. When the time delay is very short, the particles have not moved appreciably; thus, the original signal is very similar to the signal after the short time delay. As the time delay grows larger, the correlation between the two time points exponentially diminishes as particles continue to move. The decay of the autocorrelation function is related to the diffusion coefficient of the particles in dispersion.

Hydrodynamic radius (R_H) distributions of QD dispersions in hexane, toluene, chloroform, or tetrahydrofuran were determined using a Brookhaven BI-200SM DLS instrument equipped with a 637 nm Mini-L30 laser as the light source and a BI-9000AT autocorrelator (Brookhaven Instrument Corporation). All dispersions were filtered twice through 0.2 μm PTFE or GHP filters and diluted to 0.1−1 μM to avoid multiple scattering events, prior to DLS collection. DLS from each dispersion was collected at room temperature and at five different detector angles ranging from 60° to 120° using an automated goniometer. Scattered light intensities were time-averaged for a minimum of 2 min at each angle. The autocorrelation function was interpreted using the REPES model to detect the presence of multiple particle sizes.[100] In general, DLS from each sample appeared similar in peak width and symmetry across all angles, whereas the peak width and symmetry may vary from sample to sample.

Example DLS data of CdSe QDs synthesized in this work is given in Figure 2.6. The hydrodynamic radius is larger than the radius of the QDs determined by absorbance or TEM; this is in part due to the ligands on the QD surface contributing to the size observed in DLS (but not in absorbance or appreciably in TEM). Additionally, the hydrodynamic radius samples an average of the particles in movement in a solvent.

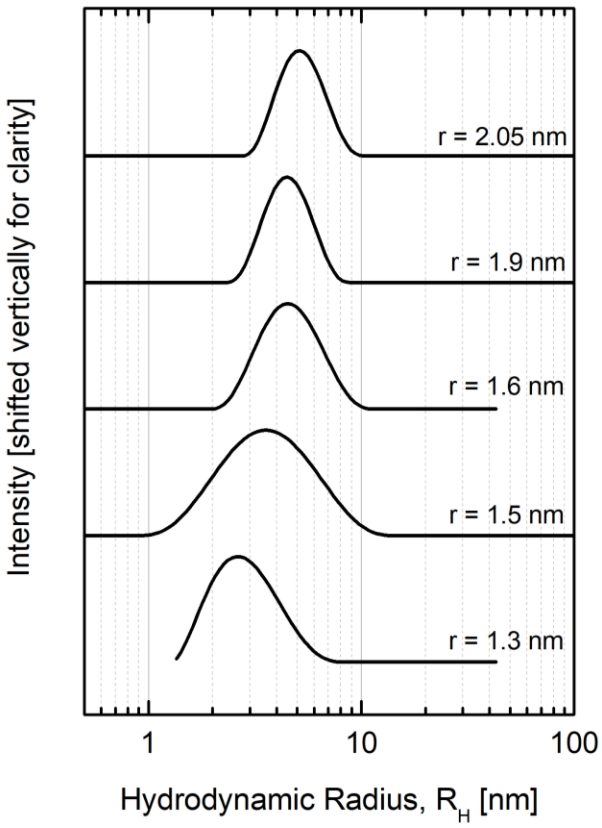

Figure 2.6: Hydrodynamic radii distributions of CdSe QDs in hexane obtained via DLS, where 'r' is the corresponding QD radius determined via absorbance using Eqn. 2.1.

2.3.6a Discussion of DLS Models

In general, the autocorrelation function, ACF, is given by

$$ACF = g^2(q,\tau) = \frac{< I(t)\, I(t+\tau) >}{< I(t) >^2} \tag{2.7}$$

where $g^2(q,\tau)$ is the order autocorrelation function, q is the wave vector, τ is the time delay, and I is the intensity. If the population is monodisperse, the autocorrelation function can be described by a single exponential. In this case, the Siegert equation then relates the second-order autocorrelation function, $g^2(q,\tau)$, to the first-order, $g^1(q,\tau)$, by

$$g^2(q,\tau) = 1 + \beta[g^1(q,\tau)]^2 \tag{2.8}$$

where β is a correction factor accounting for alignment and geometry of the scattering setup. The first-order autocorrelation function can be related to the decay rate, Γ, as follows:

$$g^1(q,\tau) = \exp(-\Gamma\tau) \tag{2.9}$$

The decay rate is then related to the translational diffusion coefficient, D_T:

$$\Gamma = q^2 D_T \tag{2.10}$$

The wave vector is calculated by

$$q = \frac{4\pi n_o}{\lambda} \sin\left(\frac{\theta}{2}\right) \tag{2.11}$$

where n_o is the refractive index of the solvent. The hydrodynamic radius, or the Stokes radius, represents the radius of a perfect, hard sphere that diffuses at the same speed of the particle under investigation and is calculated by

$$R_H = \frac{k_B T}{6\pi\eta_s D_T} \tag{2.12}$$

where k_B is the Boltzmann constant, T is the temperature of the sample, and η_s is the solvent viscosity. When the sample is monodisperse, the cumulant method may be used to fit the data:

$$g^2(q,\tau) = A \times \exp(-2\Gamma\tau) \times \left(1 + \frac{\mu_2}{2} \times \tau^2 - \frac{\mu_3}{6} \times \tau^3 + \cdots\right) + B \tag{2.13}$$

where A is an intensity scaling factor, μ_m are moments about the mean with μ_2 as the variance of the mean and μ_3 as the measure of asymmetry about the mean, and B is the background. The cumulant method may be extended to samples with multiple size populations by considering a summation of single exponentials, but this requires some

knowledge about expected particle sizes and has small error differences in appreciably different estimates of particle sizes.

Instead, an alternative method is suggested for more complex systems with greater polydispersity or multiple size populations: REPES or its predecessor, CONTIN. REPES and CONTIN use inverse Laplace transforms to analyze the autocorrelation function. These methods use numerical methods to determine the general sizes and dispersities of a given sample. To concretely distinguish separate populations, the difference in relative intensities between the populations should be less than $1{:}10^{-5}$. Additionally, the two particle populations should be different in size by a factor of 5. For most of the work reported here, the REPES model was used.

Chapter Three - Quantum Dot Ligand Exchange

Quantum dots (QDs) are typically synthesized using rapid mixing of precursors by injection into a solution of coordinating solvents and surfactants. The surfactants not only mediate nucleation and growth but also adsorb onto and sterically stabilize the quantum dots in dispersions. Typical surfactants include trioctylphosphine, trioctylphosphine oxide, oleic acid, and oleylamine. Often, however, these surfactants on the QDs must be exchanged with another ligand. For example, in biodiagnostics, the ligand must be biocompatible, and ligands such as trioctylphosphine oxide (TOPO) are often exchanged with poly(ethylene glycol) (PEG).[7, 81,101] In optoelectronic applications, films are cast from dispersions and the ligands determine the interparticle spacing, an important property that affects the electronic and optical coupling between the quantum dots: in these cases, long ligands are often exchanged with shorter ones to facilitate charge and exciton transport.[22,102] In photonic applications such as solar concentrators, the goal is to construct a composite material comprising QDs dispersed in a host material (e.g., a polymer): in this case, the ligands are exchanged with molecules that have favorable interactions with the host.[103,104]

In only a few cases the surfaces of the QDs before and after ligand exchange have been quantified and studied in some detail. For example, PEG is a commonly chosen ligand used to create water-soluble CdSe particles. Uyeda et al.[11,105] synthesized bidentate thiol-capped PEG ligands and attached them to CdSe−ZnS core−shell QDs to disperse them in aqueous and polar solvents. Similar strategies are common,[106] with an emphasis on how this functionalization affects biocompatibility[7,107] and how to preserve high fluorescence yields.[81,108] While most of these studies infer dispersion from the presence

of fluorescent QDs in hydrophilic and polar solvents, only a few show the state of aggregation via dynamic light scattering,[81] and none have quantitatively studied the extent of ligand exchange and coverage.

In this chapter, we investigate the extent of ligand exchange of trioctylphosphine oxide, trioctylphosphine, and phosphonic acids to a thiolated poly(ethylene glycol) (PEG-SH) on the surface of CdSe QDs. We quantify the extent of ligand exchange by determining ligand surface concentration (number of ligands per unit area of QD surface) using attenuated total reflectance Fourier transform infrared spectroscopy (ATR-FTIR) and identify the resulting effect on QD dispersion in different solvents via dynamic light scattering (DLS). Sections of this chapter are taken from a publication in Langmuir detailing these results.[82]

Section 3.1 - Exchanging Trioctylphosphine Oxide for Poly(ethylene glycol)

The ligand exchange procedure was based on a modified version of the protocol reported by Chen et al.[81] CdSe QDs in hexane were diluted and their concentration determined from UV−vis absorbance via the relationship reported by Jasieniak et al.[89] A known volume of this solution was dried to recover a specific amount of QDs (typically 2−4 nmol), which were redispersed in 200−400 μL of chloroform to make 10 nmol/mL dispersions. This dispersion was added to a 0.3 mg/mL solution of 2000 g/mol PEG−SH dissolved in chloroform (30 mg of PEG per 1 nmol of CdSe) and stirred at room temperature overnight in a septum capped vial. Following, hexane (typically ∼5 mL) was added to the solution until it turned turbid. The solution was centrifuged for 3 min at 4000 rpm, and the supernatant was discarded. This rinsing process was repeated 0-2

times. The QDs collected at the bottom of the vial were dried in air before redispersing them in chloroform. In some cases QDs did not separate to the bottom of the vial and remained dispersed in chloroform with hexane forming a second liquid phase above the chloroform. In these cases, the clear portion of the supernatant was removed, fresh hexane added, and the centrifugation repeated until the QDs separated from the supernatant.

3.1.1 Procedure Variations

Other modifications to the exchange process were tested. The original procedure from Chen et al. included the use of a small quantity of $NaBH_4$ during the exchange process.[81] There was no discernable change in ligand exchange with or without $NaBH_4$; thus, the NaBH4 was removed from the procedure.

The exact amount of PEG-SH added to the QDs seemed to be largely inconsequential as long as PEG-SH was in relative abundance compared to the surface concentration of native ligands. The lowest concentration of PEG ligands tested was 2 orders of magnitude larger in the total number of PEG ligands added than the total number of expected surface trioctylphosphine oxide (TOPO) ligands; no change in the PEG functionalized QDs was observed at this concentration or any higher concentrations tested.

Section 3.2 – Effect of Ligand Exchange on Quantum Dot Optical Properties

Figure 3.1 shows the absorbance and fluorescence spectra from CdSe QD dispersions before and after exchanging the native TOP, TOPO, and ODPA ligands with

PEG-SH. The QDs are dispersed in hexane before ligand exchange and in chloroform after the exchange.

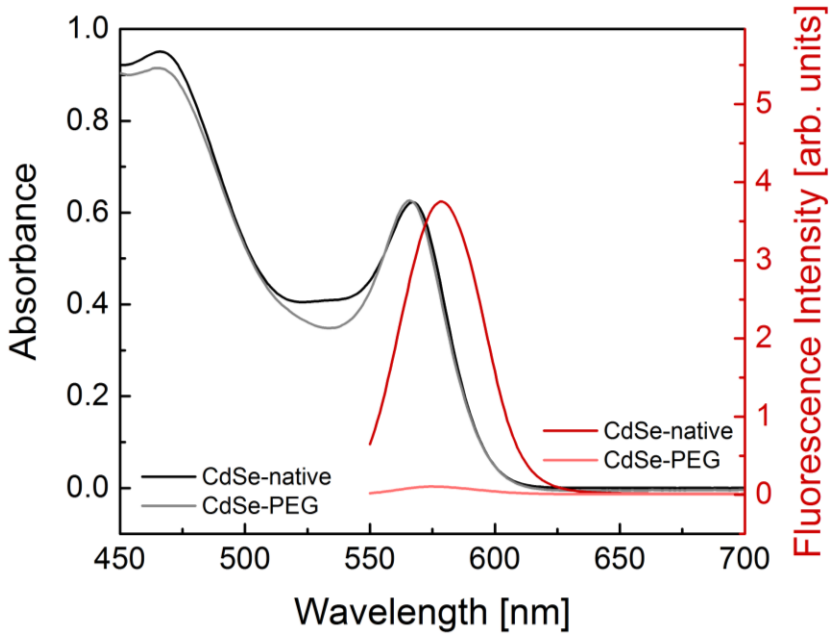

Figure 3.1: Absorbance and fluorescence of 1.8 nm diameter CdSe quantum dots before (labeled as CdSe-native, in hexane) and after ligand exchange (multiplied by 3.5) with thiol-functionalized poly(ethylene glycol) (labeled as CdSe-PEG, in chloroform). The peak absorbance shown here is 567 nm.

The absorption spectra nearly overlap, indicating that the QD structure remains unaffected. However, there is about an order of magnitude drop in fluorescence intensity after ligand exchange. This fluorescence quenching is expected as ligand exchange often leads to the creation of surface trap states where photogenerated carriers can access nonradiative recombination pathways.[109,110] The drop in fluorescence suggests that although the core structure of the QDs remains intact, the QD surfaces have been modified.

Section 3.3 – Effect of Ligand Exchange on QD Hydrodynamic Radius & Solvent Preferences

Distributions of hydrodynamic radius, R_H, before and after ligand exchange were consistent with the presence of PEG-SH molecules on the QD surfaces. Figure 3.2 shows the hydrodynamic radius distributions of QDs in various solvents as determined from DLS using the REPES model.

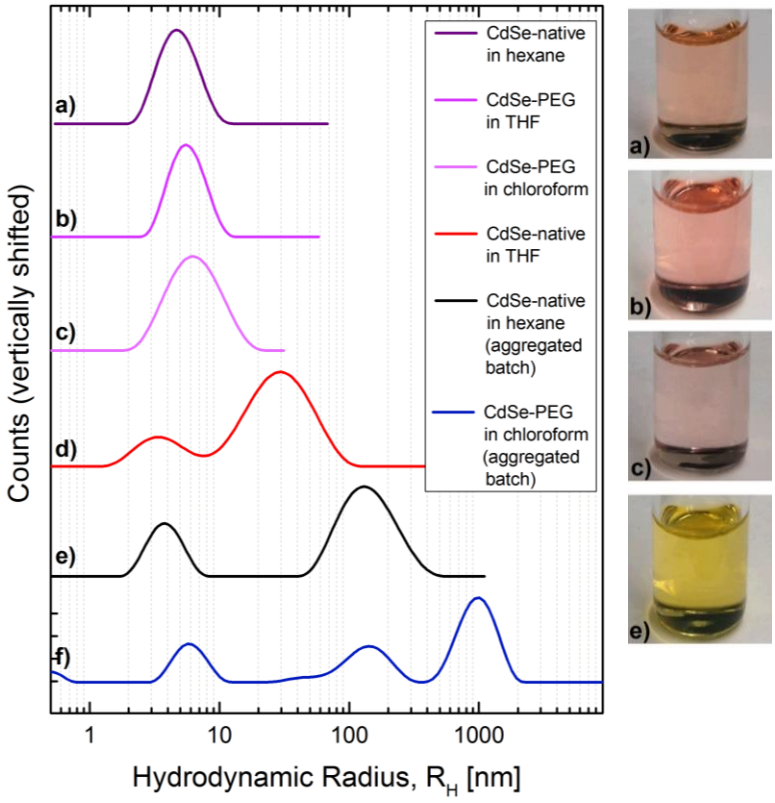

Figure 3.2: Hydrodynamic radius distributions of CdSe quantum dots dispersed in various solvents before and after ligand exchange from dynamic light scattering interpreted using the REPES model. Four quantum dot dispersions are shown here: dispersions a-c are a batch of QDs before (in hexane) and after ligand exchange (in tetrahydrofuran and chloroform), dispersion d is a batch of quantum dots aggregated in tetrahydrofuran, dispersion e is a batch of quantum dots aggregated in hexane, and dispersion f is a batch of aggregated quantum dots after ligand exchange. CdSe QDs with native ligands show beginning stages of aggregation in dispersion e but this aggregation is not yet visible to the naked eye, as shown in the digital photograph also labeled e. Photographs a-c show examples of well-dispersed quantum dots, which appear clear, similar to the aggregated dispersion in photograph e. The DLS data displayed here were chosen as representative of a larger set of data acquired at multiple detector angles, all of which showed similarly shaped distributions (no significant asymmetry and similar widths) across all angles.

As-synthesized CdSe QDs covered with native ligands form stable dispersions in organic solvents such as hexane (Figure 3.2a), but they aggregate over time in polar solvents such as tetrahydrofuran (Figure 3.2d). In contrast, after ligand exchange with PEG-SH, the QDs could not be dispersed in hexane but they readily formed dispersions in polar solvents such as tetrahydrofuran (Figure 3.2b) and chloroform (Figure 3.2c). The R_H distribution of QDs with native ligands in hexane peaks at 4.5 nm. After ligand exchange, the peak of the distribution shifted to 5.5 nm in tetrahydrofuran (Figure 3.2b) and to 6.5 nm in chloroform (Figure 3.2c). From batch to batch, and depending on the solvent, the location of the peak of the R_H distribution consistently grew larger by 1-4 nm. This shift is on the same length scale as the radius of gyration, R_g = 2 nm, of PEG-SH. For example, if we envision the PEG-SH to be tethered to the QD surface and coiled on a length scale $2R_g$, we would expect the hydrodynamic radius distribution to shift approximately by this amount, or 4 nm. However, the configuration of the PEG-SH attached to the QD is expected to depend on the surface coverage of PEG-SH and the solvent, either extending outward from the QD surface in a loose coil or confined to a tight coil near the surface of the QD, possibly explaining the range of hydrodynamic radii measured using DLS.

Making stable dispersions of QDs in polar solvents after ligand exchange is not trivial and depends critically on the steps used to separate the as-synthesized QDs from the reaction solution. Specifically, it is necessary to achieve well-dispersed QDs both before ligand exchange, which depends on the number of washing steps performed after synthesis. If the QDs were washed inadequately, only once after synthesis, excess TOP and TOPO remained in the solution and solidified over time. On the other extreme, too

many washing steps often led to aggregation and unstable dispersions, likely because ligands were stripped from the surface and the QD surface coverage decreased. For example, Figure 3.2e shows the hydrodynamic radius distribution of a batch of QDs with native ligands in hexane. Even before ligand exchange, these QDs have aggregated: the R_H distribution is bimodal, showing the primary particle distribution peaking at 4 nm, but also aggregates that are 100-200 nm in radius. This particular batch was washed too many times. Often in the literature visual clarity of a dispersion is interpreted to mean that the individual QDs are well-dispersed and not aggregated. This is insufficient evidence. A digital photograph of the dispersion with aggregates shows that it is transparent and appears well-dispersed to the eye despites the obvious aggregation evident in the DLS data. This aggregation is not noticeable in the absorption spectra, but it is significant because it is irreversible and often leads to further aggregation with time. Attempting ligand exchange with QDs that have already aggregated is futile precisely because the aggregation is irreversible and the PEG-SH has limited access to the surfaces of the individual QDs within an aggregate. As an example, Figure 3.2f shows the R_H distribution of QDs after ligand exchange when these QDs were aggregated even before ligand exchange. Predictably, the QDs remain aggregated and form secondary particles as large as 1 μm.

If the QDs are well-dispersed before ligand exchange, they remain well-dispersed in chloroform and tetrahydrofuran for weeks after ligand exchange (as in Figure 3.2a – c). Furthermore, we consistently see a 1-4 nm increase in the hydrodynamic radius of the QDs after ligand exchange and the dispersions with the larger increase tend to be more stable. We attribute this increase to the presence of PEG on the surface.

Section 3.4 - Quantifying Extent of Ligand Exchange

ATR-FTIR was used to determine ligand coverage on the QD surface before and after ligand exchange. The model used to quantify ligand coverage is discussed in the beginning of this section and followed by experimental data.

3.4.1 ATR-FTIR Model

Ligand coverage on the QD surfaces was determined using a Nicolet Magna 550 spectrophotometer equipped with a Harrick Scientific Horizon ATR-FTIR attachment. To determine native ligand coverage prior to ligand exchange, concentrated dispersions of QDs in hexane were dropcast onto a 1 cm × 5 cm × 0.2 cm germanium trapezoidal ATR crystal with 45° beveled edges. Spectra were taken as the dispersions dried on the crystal to monitor the solvent absorption peaks. All infrared spectra were taken with reference to the bare ATR-FTIR crystal. Once the QD coating on the ATR crystal was dry to the eye and the solvent absorbance peak height fell to a small fraction of the ligand absorbance, additional QDs were dropcast on to the existing coating. This process was repeated multiple times until the thickness of the coating exceeded the penetration depth of the infrared radiation (>0.7 μm at 1000 cm^{-1}) and the absorbance saturated (i.e., absorbance changed less than ∼5%).[110] The coating was then allowed to dry overnight. The procedure to determine the ligand coverage after exchange was identical except the QDs were dispersed in chloroform. The infrared spectra of TOPO and PEG−SH were collected for reference using a similar procedure: TOPO was dried on the ATR crystal from a hexane solution, while PEG−SH was dried from a chloroform solution. The infrared spectrum of TOP was collected from a neat liquid TOP layer on the ATR crystal. The surface concentration, or absolute number of ligands per unit area of the QD surface, was

determined by following the method conceived by Tosun et al.[111] for determining the surface coverage of copper zinc tin sulfide nanocrystals. The infrared absorbance, A_{QD}, of the ligands on the QDs cast as a coating is given by

$$A_{QD} = N_s \varepsilon S_{QD} \tag{3.1}$$

where N_s is the number of ligands per unit area on the QD surface, ε is the absorptivity of the ligands, and S_{QD} is the total surface area of the QDs within the thickness sampled by the evanescent infrared radiation. Assuming spherical QDs with radius r form a randomly packed coating with solid fraction f (e.g., f = 0.63) with thickness larger than the penetration depth, d_p^{QD} , the surface area, S_{QD}, can be replaced and Eqn. 3.1 becomes

$$A_{QD} = \frac{3N_s f \varepsilon a_c d_p^{QD}}{r} \tag{3.2}$$

where a_c is the area that the QD coating covers on the ATR crystal. The penetration depth can be calculated, the values of A_{QD} and a_c are measured, and the QD radius, r, can be determined from the peak of the exciton absorbance. Thus, to calculate the number of ligands per unit area, N_s, only ε needs to be determined. We find ε by measuring the infrared absorbance of the ligands alone, which is given by

$$A_l = N_l \varepsilon a_l d_p^l \tag{3.3}$$

where A_l is the infrared absorbance of the ligands on the ATR crystal, N_l is the density of the ligands, a_l is the area that the ligands cover on the ATR crystal, and d_p^l is the infrared radiation penetration depth into the ligand coating. Substitution of ε in Eq. 3.2 gives an expression for the number of ligands per unit area:

$$N_s = \frac{A_{QD} r d_p^l a_l N_l}{3 A_l f d_p^{QD} a_c} \tag{3.4}$$

The penetration depth of the infrared radiation into a coating of *i* (e.g., *i* = quantum dots, ligands, etc.) can be calculated from

$$d_p^i = \frac{\lambda}{2\pi n_{Ge}\sqrt{\sin^2\theta - \left(\frac{n_i}{n_{Ge}}\right)^2}} \tag{3.5}$$

where λ is the absorption wavelength, n_{Ge} is the refractive index of the germanium ATR crystal, θ is the total internal reflection angle, and n_i is the refractive index of the film. The refractive index of the CdSe QD film can be calculated using the Bruggeman effective medium theory by considering the film as a composite of QDs and void spaces. The coatings formed from TOP and TOPO ligands and the CdSe QDs with native ligands covered the entire crystal surface so that a_c = 5 cm^2. However, coatings formed from PEG ligands and the CdSe QDs after ligand exchange covered only a fraction of the germanium ATR crystal's surface. The areas, a_c, in these cases were determined from digital photographs by first tracing the boundaries of the coating and then using ImageJ: this was repeated five times and the results were averaged.

3.4.2 Ligand Coverage Quantification

Figure 3.3 shows the infrared absorption spectra of the ligands anticipated to be on the QD surface after the synthesis, TOP and TOPO, and after ligand exchange, PEG-SH. TOP and TOPO show the same characteristic absorption due to C-H stretches at 2852 and 2921 cm^{-1} while the C-H absorption in PEG-SH appears at 2884 cm^{-1}, resolvable between the two C-H absorption peaks in TOP and TOPO. The C-O absorption peak in PEG-SH at 1110 cm^{-1} is prominent and serves as another marker of the presence of PEG. Figure 3.3 also shows infrared spectra from two different sizes of QDs (labeled 1 and 2; 2 and 1.6 nm radii, respectively) before and after exchanging the

native ligands with PEG-SH. Before ligand exchange, the infrared spectra of the QDs (labeled CdSe-native 1 and CdSe-native 2) in the C-H stretching region (2800-3000 cm^{-1}) mirror the infrared spectrum of TOP and TOPO, confirming that these ligands are present on the surface of the QDs. The spectra are dominated by the ligands on the surface of the QDs and there is no interference from free ligands, as evidenced by the absence of the sharp P=O stretching absorption at 1144 cm^{-1} in the infrared spectrum of the QDs. The P=O peak has shifted and split into several broad peaks, indicative of binding and coupling to the QD surface.[91-94] Quantifying the surface coverage using the peaks marked 1 and 3 in Figure 3.3 yields a surface concentration of $(1.57 \pm 0.08) \times 10^{14}$ TOP or TOPO molecules/cm^2 before ligand exchange for both 1.6 and 2 nm radius QDs. If we assume that the QD surface is densely packed with ligands and use the frequently invoked cone model[112,113] of ligand adsorption, this surface concentration corresponds to a cone area of 0.67 nm^2 or a ("swept-out") cone radius of 0.46 nm, in reasonable agreement with previous estimates (0.55 nm): the cone model conceptualizes the ligand and its time-averaged molecular configurations on the surface to sweep out and exclude a conical region with a narrow footprint on the QD surface and a wider base above the surface. Converting this measurement to fractional coverage of surface sites requires assumptions about the number (concentration) of surface sites per unit area, and various assumptions have led to nanocrystal radius-dependent values ranging from 20% to 100%: the fractional coverage decreases with increasing radius because adsorption is sterically hindered on surfaces with high curvature. The IR measurements given here indicate approximately 50 and 80 TOP/TOPO ligands on 1.6 and 2 nm radius nanocrystals, respectively.

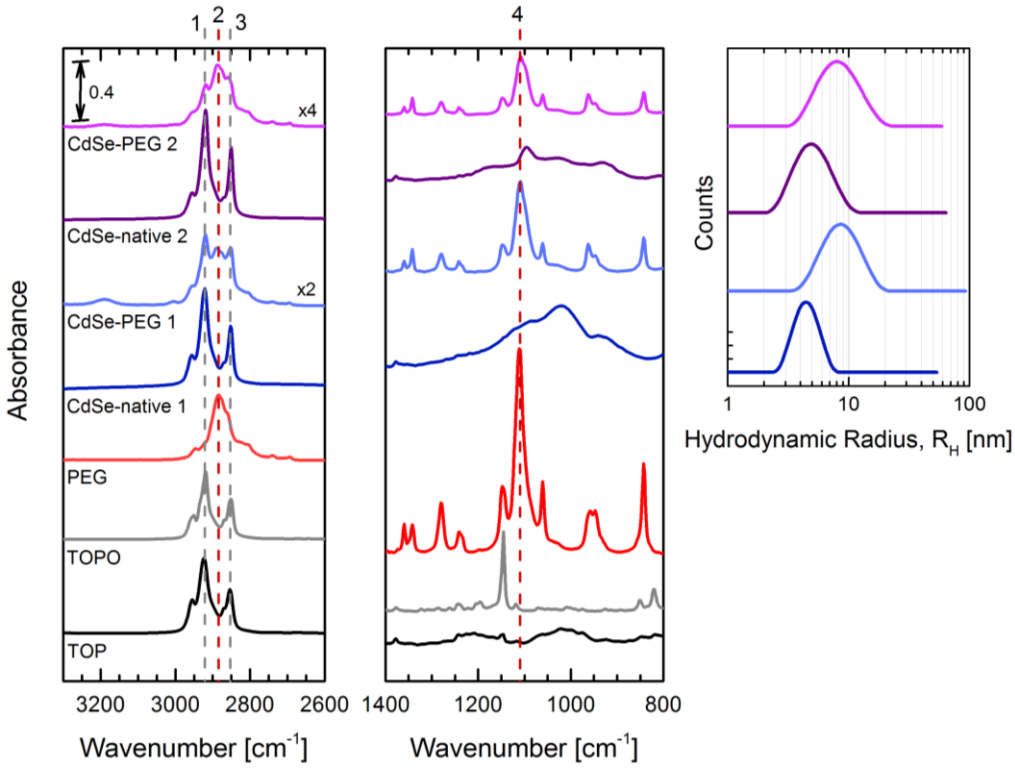

Figure 3.3: Fourier transform infrared spectroscopy (FTIR) of ligands and CdSe QDs before and after ligand exchange. Two different batches of CdSe QDs are shown here (labeled as 1 and 2, with radii of 2 and 1.6 nm, respectively) with accompanying dynamic light scattering results shown on the far right. Peaks of interest are labeled 1-4, with 1 and 3 corresponding to the C-H alkane stretches from the trioctylphosphine and trioctylphosphine oxide ligands, 2 corresponding to the C-H alkane stretches from PEG-SH ligands, and 4 corresponding to the C-O stretch from the PEG-SH ligands. All spectra are shifted vertically for visual clarity. The scale bar shown on the left applies to both IR graphs.

After ligand exchange the infrared spectra show presence of both PEG-SH and the native TOP and TOPO ligands, indicating that some of the native ligands have been replaced by PEG-SH. Specifically, the C-H absorption peak in PEG-SH (labeled 2 in Figure 3.3) increases while C-H peaks in TOP and TOPO (peaks 1 and 3) decrease. The surface concentration of the TOP/TOPO molecules has decreased from 1.57×10^{14} to 7×10^{13} ligands/cm^2 for the 2 nm radius QDs and to 2×10^{13} ligands/cm^2 for the 1.6 nm radius QDs. Quantifying the surface coverage using the C-H and C-O absorption peaks

for PEG-SH (peaks 2 and 4 in Figure 3.3) yields a surface concentration of 6×10^{12} PEG molecules/cm^2 for the 1.6 nm and 8×10^{12} PEG molecules/cm^2 for the 2 nm radius QDs. This corresponds to an average of 2 and 4 PEG-SH ligands on the surface of each 1.6 and 2 nm QD, respectively. We anticipate that these PEG-SH bind to cadmium sites on the QD surface. Remarkably, there are still, on average, approximately 7 and 35 TOPO ligands on the 1.6 and 2 nm radius QDs, respectively, many more than the PEG-SH molecules. However, the presence of only a few PEG molecules on the surface is sufficient to alter the interactions of the QDs with solvent, rendering them dispersible in polar solvents.

Section 3.5 – Interpreting Results of QD Dispersions

Figure 3.4 shows a conceptual illustration of the surfaces of the QDs before and after ligand exchange in solvents with different polarities, ranging from nonpolar hexane to polar water that can also form hydrogen bonds. Before ligand exchange, the surface is covered with TOP and TOPO ligands. After ligand exchange, 50-85% of the TOP/TOPO ligands are removed, but only a few are replaced with PEG. These few PEG ligands, however, are sufficient to change the interactions between the QDs and the solvent, causing the QDs to aggregate in nonpolar solvents such as hexane but disperse in polar solvents such as chloroform and tetrahydrofuran; this is despite TOP/TOPO ligands outnumbering the PEG ligands. Clearly, even a few PEG molecules alter the net interaction energy between the QDs and the solvent molecules.

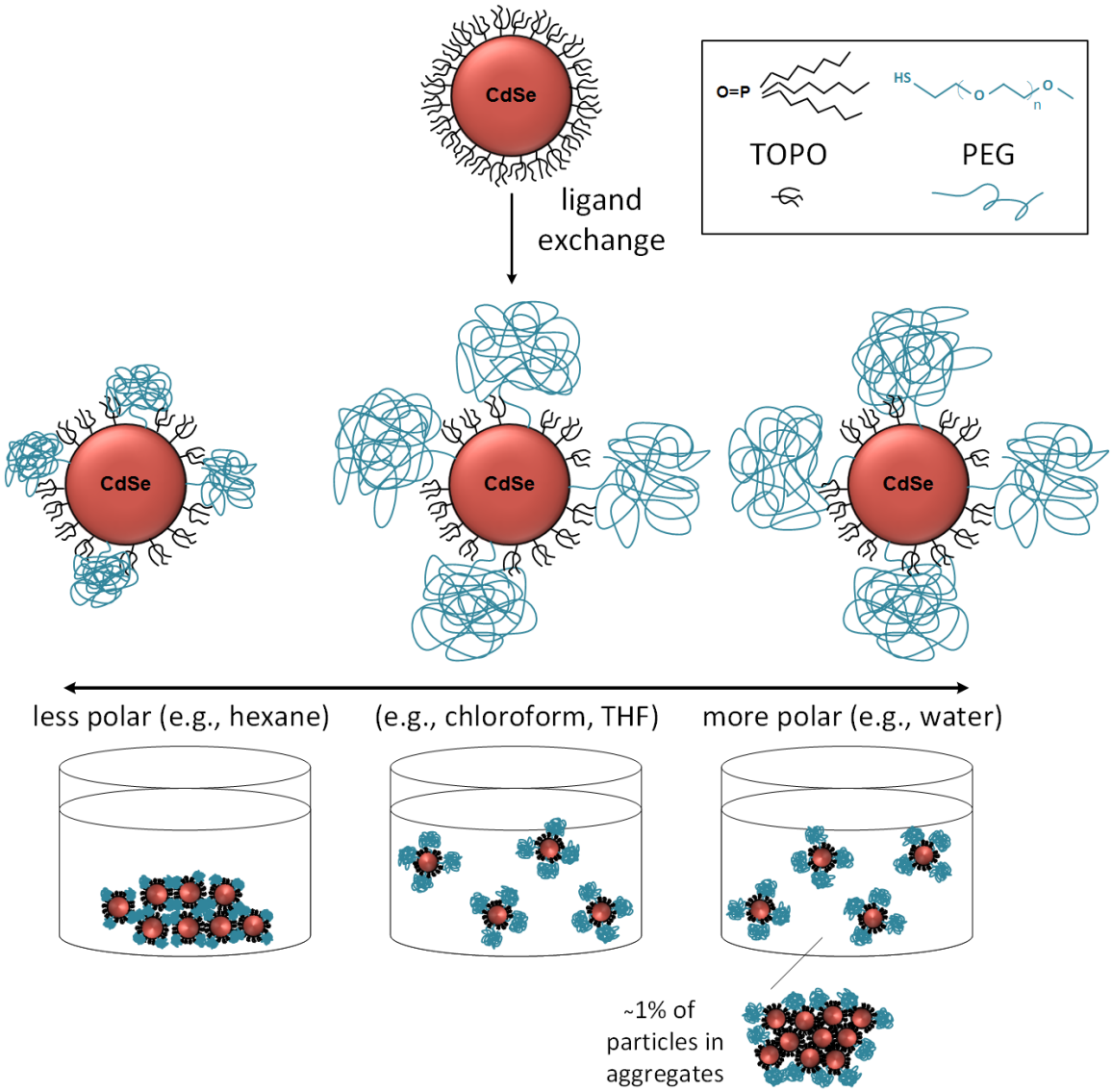

Figure 3.4: Illustration of the QD (2 nm radius) surfaces before and after ligand exchange with PEG-SH with examples of their behavior in solvents with different polarity.

Whether the QDs disperse or aggregate is determined by the Gibbs energy difference between these two states, and this difference depends on (i) the energy of the interaction between the TOP/TOPO and the solvent, (ii) the energy of interaction between the PEG and the solvent, and (iii) the entropic penalty of limiting the PEG configurations by tethering it to the QD surface and confining it near the QD. The DLS

data in Figure 3.2 show that a balance is achieved between these interactions to keep CdSe quantum dots dispersed in chloroform and tetrahydrofuran. In good solvents for PEG, such as chloroform and tetrahydrofuan [the solubility parameters are 9.9, 9.3, and 9.1 $(cal/cm^3)^{1/2}$, respectively][114] the PEG chains are expected to behave as ideal chains, swelling to maximize the favorable interactions with the solvent while excluding the solvent in the space near TOP/TOPO ligands. Once a few PEG molecules are adsorbed on the surface, they sterically hinder the exchange of the remaining TOP/TOPO ligands with PEG. The radius of gyration of 2000 g/mol molar mass PEG chain is 2 nm, comparable to the radius of the QDs plus the TOPO ligand length (2.6-3 nm in this study). Even if these coils behaved like hard spheres and packed tightly around the QDs without distorting we would expect ≈ 12 PEG molecules around each QD. The PEG molecules could spread and assume configurations that average to spherical caps to shield the remaining TOP/TOPO from the polar solvent. Assuming 1 nm TOP/TOPO shell around a 2 nm radius QD,[113] 4 PEG-SH ligands can shield as much as 45% of the surface; ignoring the TOP/TOPO shell, much of which has been stripped, 4 PEG molecules shield the entire surface of a 2 nm QD. Just a few PEG molecules on the surface in a good solvent coupled with reduced coverage of TOP/TOPO ligands on the surface leads to net favorable interactions between the QD and solvents such as chloroform.

In nonpolar solvents (far left in Figure 3.4) such as hexane, this balance is disturbed: the PEG tethered on to the QDs collapses, expelling the solvent and leading to aggregation via favorable PEG-PEG interactions between nearest neighbors in aggregates. We estimate that in hexane PEG would collapse to a sphere with 0.9 nm radius comparable to the extended length of the TOP/TOPO ligands, protruding

approximately 1 nm from in between the TOP/TOPO ligands. In hexane, these protruding PEG ligands can attract PEG ligands on other QDs, leading to aggregation.

The photograph in Figure 3.5 shows two vials with hexane separated on top of water and QDs before and after ligand exchange.

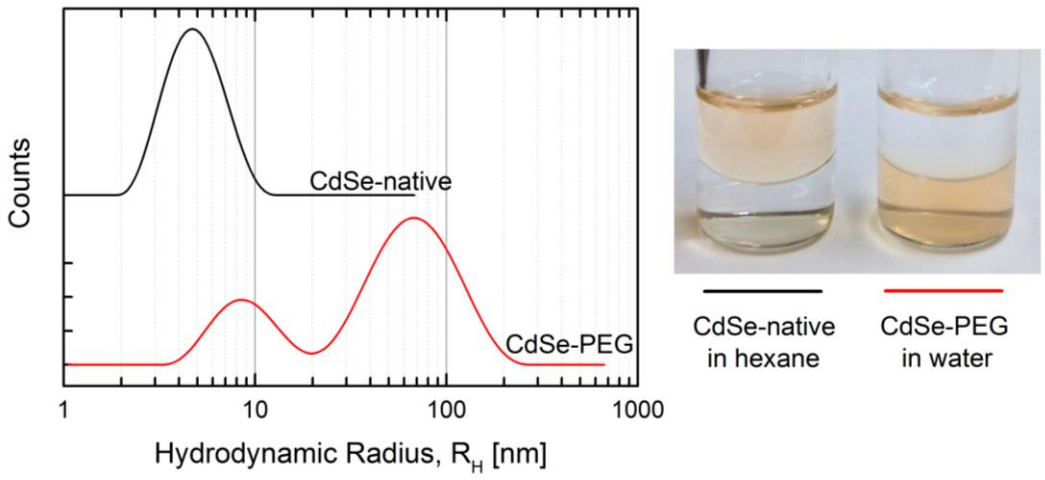

Figure 3.5: Hydrodynamic radius distributions of CdSe QDs before (in hexane) and after (in water) ligand exchange, determined via dynamic light scattering (left), and a photograph showing the solvent preference of the QDs before and after ligand exchange (right). In the photograph, hexane sits on top of water in both vials. There are, on average, 2 PEG ligands per QD after ligand exchange for this QD size (1.6 nm radius).

Before ligand exchange, the QDs prefer hexane (the phase on the top), while after ligand exchange, the QDs prefer water (the phase on the bottom). Figure 3.5 also shows the hydrodynamic radius distribution in hexane, before ligand exchange, and in water, after ligand exchange. Some fraction of the CdSe QDs have aggregated in water as evidenced by presence of a peak at $R_H \approx 70$ nm. When the solvent polarity is even higher than that of tetrahydrofuran and chloroform (e.g., water), the balance between favorable PEG-solvent and unfavorable TOP/TOPO-solvent interactions is again disturbed: while PEG ligands on the surface of the QD interact favorably with water, the remaining TOP/TOPO ligands on the surface are insoluble in water, making it thermodynamically favorable to

form aggregates that minimize the TOP/TOPO-water interactions. These opposing interactions are balanced with only a few (2-4) PEG molecules attached to the QD surface. It is reasonable to expect that there is a distribution of PEG molecules on the surface, and we surmise that the fraction of QDs that have aggregated are those that have fewer PEG molecules than the average. Assuming that the index of refraction of the aggregate is comparable to that of an individual QD, we estimate that there is approximately only one 70 nm aggregate for every 10^5 unaggregated QDs in this dispersion, despite the fact that the DLS intensity for the aggregate peak at $R_H \approx 70$ nm is larger than that for the individually dispersed QDs: the intensity of the peaks in the distribution is proportional to particle volume squared. Each 70 nm aggregate comprises $\approx 10^3$ QDs so that only ~1% of the original QDs have aggregated.

Section 3.6 – Films Prepared from QD Dispersion

Micrographs of dropcast CdSe QDs after ligand exchange with PEG-SH no longer exhibit the well-ordered packing evident in CdSe QDs before ligand exchange. Figure 3.6 shows micrographs of 2.3 nm radius CdSe QDs functionalized with PEG. In these micrographs, the QDs do not appear to form any ordered structures but are instead randomly distributed on the carbon-coated copper TEM grid. Overall, the spacing between QDs increases after ligand exchange, which is consistent with the presence of PEG on the QD surface. Given the small number of PEG molecules expected to be on the surface of each QD (≈4, if compared to the 2 nm radius QDs), it is unsurprising that small variations in the number of PEG ligands on the surface could have a big effect on the resulting packing of the QDs. For example, while on average, if roughly 4 PEG

molecules are on the surface of each QD, a large population of the QDs might have 3 or 5 PEG molecules instead, resulting in a change of 20-25% of the surface PEG ligands. Additionally, the few PEG ligands on each QD may not be distributed evenly around the QD surface, resulting in a non-spherical ligand 'shell' that affects the QD's packing. Because the PEG ligands (radius of gyration ~ 2 nm) are roughly the same size as the QDs themselves (2.3 nm radius), variations in the number and position of PEG ligands attached to the QD surface have a large role on the resulting shape of the QD and its ligand shell. Additionally, chloroform has a slightly higher vapor pressure than hexane – 197 mmHg for chloroform at room temperature versus 151 mmHg for hexane at room temperature – which could result in the QDs having insufficient time to order before solvent evaporation. The FFT of the left image in Figure 3.6 does not indicate a clear average center-to-center QD distance; this is attributed to the irregularity of the QD spacing.

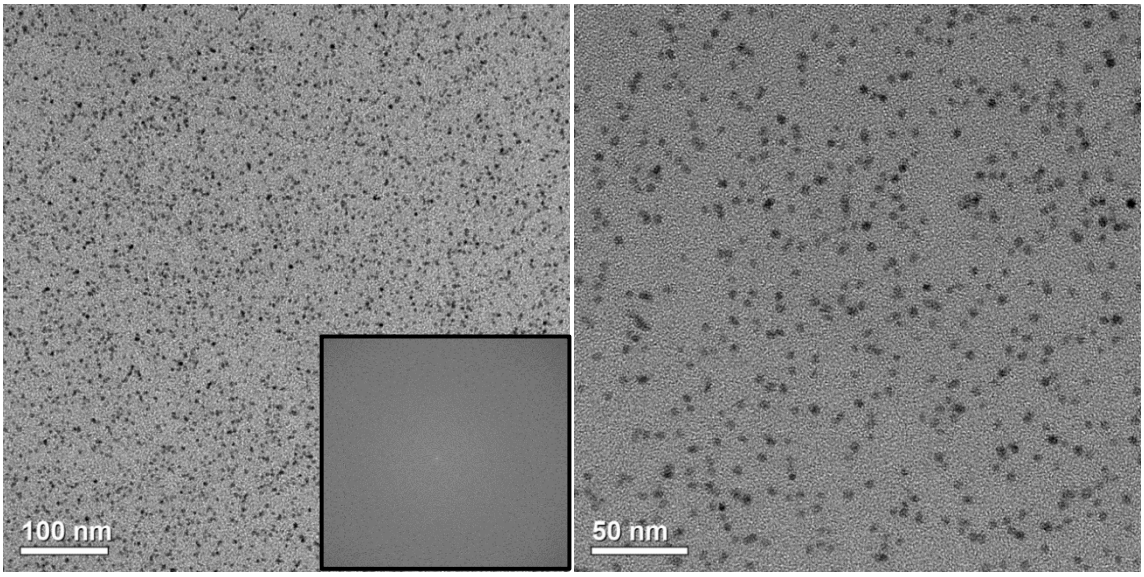

Figure 3.6: Micrographs of CdSe QDs (2.3 nm radius) functionalized with PEG-SH dropcast from chloroform onto carbon coated TEM grids. The FFT of the left image is included as an inset.

Section 3.7 – Ligand Length vs. Quantum Dot Size and Effect on Stability

The ligand length is expected to play a role in the resulting stability of the CdSe QDs. To investigate this effect, QDs were exchanged with different PEG ligand lengths. The effect of ligand length on QD dispersion was tested using 1000 g/mol and 5000 g/mol PEG-SH ligands in comparison to 2000 g/mol PEG-SH ligands.

3.7.1 Results & Discussion

Figure 3.7 shows the hydrodynamic radius of CdSe QDs before ligand exchange and after ligand exchange with 1000 g/mol, 2000 g/mol, or 5000 g/mol PEG-SH, evaluated using the REPES model.

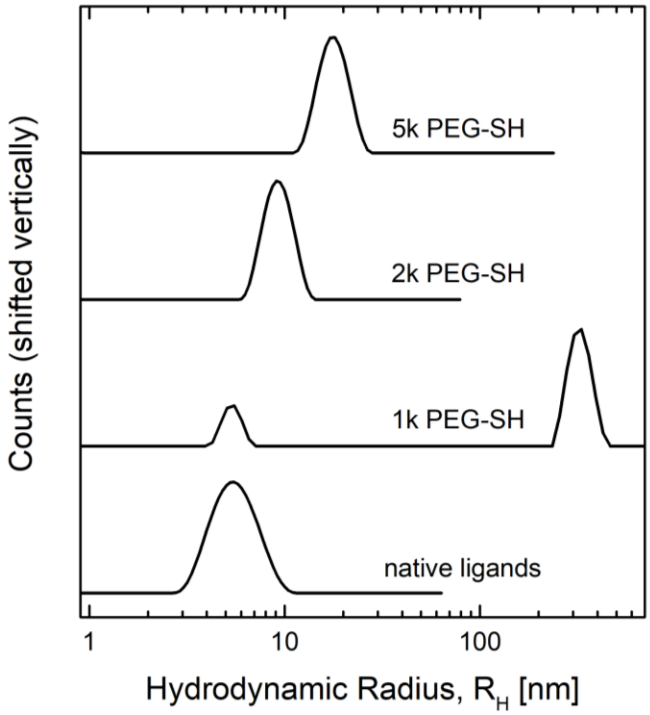

Figure 3.7: Hydrodynamic radius distributions of CdSe QDS (2.4 nm radius) before ligand exchange (native ligands, in hexane) and after ligand exchange with 1000 g/mol, 2000 g/mol, or 5000 g/mol PEG-SH (in chloroform), evaluated using dynamic light scattering.

Before ligand exchange, the QDs are stable in hexane, with a hydrodynamic radius of approximately 5.4 nm. After ligand exchange with 2000 g/mol PEG-SH, the

QDs are dispersible in chloroform and the hydrodynamic radius increases to 9 nm, a 3.6 nm shift in hydrodynamic radius consistent with the results described in earlier sections of this chapter. When the QDs instead undergo ligand exchange with 5000 g/mol PEG-SH, the hydrodynamic radius increases to 18 nm, which is larger than the hydrodynamic radius of QDs with native ligands and QDs with 2000 g/mol PEG-SH. However, when the QDs are exchanged with 1000 g/mol PEG-SH, a portion of the particles aggregate, as evidenced by the emergence of a peak in the hydrodynamic radius distribution at $R_H \approx$ 300 nm. There is a second, smaller peak in the 1000 g/mol PEG-SH spectrum at $R_H \approx 5.5$ nm. The radius of gyration of each polymer in a good solvent is approximately 1 nm, 2 nm, and 3.5 nm, for the 1000 g/mol PEG-SH, 2000 g/mol PEG-SH, and 5000 g/mol PEG-SH, respectively.

At first glance, the smaller, 1000 g/mol PEG-SH ligand length appears insufficient to stabilize the particles in more polar solvents, due to the presence of the peak at $R_H \approx 300$ nm. However, if it is assumed again that the index of refraction of the aggregate is comparable to that of an individual QD, there is approximately only one ≈ 300 nm aggregate for every 10^9 unaggregated QDs. Again, the intensity of the peaks in the hydrodynamic radius distribution is proportional to the particle volume squared. A single 300 nm aggregate contains ≈ 10^5 QDs; thus, less than 0.001% of the QD have aggregated. The second peak at ≈ 5.5 nm is comparable to QDs before ligand exchange. The radius of gyration for 1000 g/mol PEG-SH (1 nm) is on the same length scale as the native ligands on the QD surface. Thus, it is possible some ligand exchange has occurred, but the hydrodynamic radius does not shift appreciably as the short PEG-SH chain is comparable to the native TOPO ligands.

The shift in hydrodynamic radius from 9 nm to 18 nm between QDs functionalized with 2000 g/mol PEG-SH and 5000 g/mol PEG-SH is larger than would be expected given the radii of gyration of the polymers in a good solvent like chloroform: 2 nm for 2000 g/mol PEG-SH, and 3.5 nm for 5000 g/mol PEG-SH. The hydrodynamic radius shift from 5.4 nm to 9 nm for CdSe QDs covered with native TOPO ligands compared to CdSe QDs exchanged with 2000 g/mol PEG-SH is 3.6 nm, which is consistent with a polymer coil adopting the expected 2 nm radius of gyration (or 4 nm diameter). Thus, a change of roughly 7 nm would be expected between QDs with native ligands and QDs functionalized with 5000 g/mol PEG-SH. However, the difference in hydrodynamic radius between these two (5.4 nm for QDs with TOPO and 18 nm for QDs with 5000 g/mol PEG-SH) is 13.6 nm, roughly double the expected shift. One interpretation is that the 5000 g/mol PEG-SH on the surface of the QDs adopt less of a coiled conformation than the 2000 g/mol PEG-SH, and extend more as a chain. This would be expected if the ligands are densely packed near the QD surface and are forced to spread further away from the surface. Given that the QDs (2.4 nm radius) are smaller than the PEG-SH molecule (3.5 nm radius of gyration), the 5000 g/mol PEG-SH ligands cannot pack as densely around the QD as 2000 g/mol PEG-SH ligands (2 nm radius of gyration) around the same QD (2.4 nm radius). The larger chains may extend to avoid crowding near the QD surface, resulting in a larger shift in hydrodynamic radius than is expected from the difference in polymer size alone.

Section 3.8 – Conclusions

We studied exchanging TOP and TOPO ligands on as-synthesized CdSe QDs with a thiolated PEG polymer. Changes in QD fluorescence, dispersibility in various solvents, hydrodynamic radius, and FTIR absorption are consistent with the presence of PEG on the QD surface. Quantitative ATR-FTIR measurements show that only a few (2−4) PEG molecules on the QD surface are adequate to change their interactions with solvents, making them dispersible in polar solvents, even when there are still TOP and TOPO ligands present on their surface and the ligands outnumber the PEG molecules. Favorable interactions between the PEG ligands and polar solvents such as chloroform and tetrahydrofuran allow the PEG molecules to swell and cover a significant fraction of the QD's surface. These favorable interactions outweigh the energetically unfavorable interactions between the TOP/TOPO ligands and polar solvents. As polarity of the solvent increases, however, these unfavorable interactions can become strong enough to cause aggregation of the QDs that do not have adequate PEG coverage. Nevertheless, even partial ligand exchange is sufficient to stabilize CdSe QD dispersions in solvents in which CdSe with native ligands aggregate.

Chapter Four – CdSe Quantum Dots in Homopolymers

Nanoparticle dispersions in polymers have been studied for different properties for more than a century.[35] Whereas the first explorations of this kind delved into the resulting mechanical properties of the polymer host material,[36,37] the development of finely tuned quantum dot synthesis procedures has sparked renewed interest in nanoparticle-polymer composites, with an emphasis on the resulting electrical and optical properties of the matrix.[16,38,74,79,115] Towards this goal, an understanding of the thermodynamics of QD dispersion in homopolymers is an important stepping stone to achieving QD dispersion in more complicated block copolymers.

Nanoparticle dispersion in homopolymers is not a trivial matter, as many theoretical and experimental studies have demonstrated.[73,79,116-119] Many competing factors contribute to the extent of nanoparticle dispersion or aggregation in a homopolymer film. Nanoparticle aggregation is frequently attributed to van der Waals forces between particles or exclusion of the polymer chains from the volume occupied by the QDs and free energy losses associated with fitting around the impenetrable nanoparticle surfaces (so-called 'depletion' interactions) for particles without considerable surface coverage of stabilizing ligands.[117,120-123] These interactions have been cited as the cause of aggregation of carbon nanotubes and silica particles in polymer matrices.[124-126] In practice, these factors are mitigated with the addition of surface ligands on the nanoparticle surface. The interaction between the polymer matrix and the particles is then mediated by these surface ligands and, for a given polymer matrix, can be manipulated through the chemistry of the ligands, the size of the ligands, the ligand surface density on the nanoparticle surface, and the nanoparticle shape and size.[117]

When the chemistry of the ligand is the same as the host polymer ligand, the ligand size and ligand surface density on the nanoparticle surface greatly affect the miscibility of the particles.[127-129] "Wet brush" nanoparticles feature optimized ligand surface densities and ratios of ligand length to polymer matrix chain length that allow polymer matrix chains to penetrate the ligand brush. "Dry brush" nanoparticles instead prevent appreciable penetration of the polymer matrix chains in the ligand brush, typically through higher ligand densities than wet brush particles or when the polymer matrix chains are large compared to the ligand length. The transition from wet to dry brush conditions occurs for a flat surface with a ligand brush when the ligand surface density is greater than $1/N_{polymer}^{1/2}$ when the ligand degree of polymerization, N_{ligand}. is greater than the polymer matrix chain degree of polymerization, $N_{polymer}$, or when the ligand surface density is greater than $N_{polymer}/N_{ligand}^{3/2}$ when $N_{polymer} > N_{ligand}$.[117,127,130] Here, where the interest lies in spherical nanoparticles, the curved nanoparticle surface enables spreading of the ligands, reducing chain crowding away from the particle surface. This effect increases with curvature, or with decreasing nanoparticle size.[131] In general, wet brushes enable dispersion of nanoparticles in a polymer matrix via wetting of the polymer chains in the ligand brush, whereas dry brushes are more likely to induce particle aggregation.[117,127] In the dry brush case, there is unfavorable interfacial tension between the polymer matrix chains and the ligands, which results in a long-range attraction between nanoparticles. Furthermore, the polymer chains face a conformational entropy loss to fit in the space between dry brush nanoparticles. As a result, phase separation of the nanoparticles from the polymer matrix is common in the dry brush case.

The wet brush-dry brush model has been used to describe the behavior of polystyrene-coated gold nanoparticles in polystyrene matrices.[116,132]

The conditions for nanoparticle dispersion in homopolymer matrices become increasingly complicated when the ligands on the nanoparticle surface have a different chemistry than the polymer matrix. In this case, the enthalpic interactions between the host polymer and the ligands on the particle's surface play an important role. Here, the Hildebrand solubility parameters and the Flory-Huggins interaction parameter χ can provide some insight. Recall from Chapter One that χ_{AB} between components A and B is calculated by

$$\chi_{AB} = \frac{\hat{V}_{ref}}{RT}(\delta_A - \delta_B)^2 \tag{4.1}$$

where $\hat{V}_{ref}$ is the molar reference volume, T is the temperature, and δ_A and δ_B are the Hildebrand solubility parameters of components A and B, respectively.[114] When χ_{AB} < 0.5, mixing of A and B components is favorable. As χ_{AB} increases, the enthalpic interactions between components A and B become increasingly unfavorable for mixing. Thus, the difference in Hildebrand solubility parameters of the polymer A and the ligands B reflects the enthalpic environment. Borukhov and Leibler extended the polymer brush model to systems featuring attractive forces between the polymer and the ligands (χ < 0), and predicted a transition from dry brush to wet brush conditions.[130] When the solvent is poor (χ ≥ 1, in these studies), grafted brushes on a planar surface are expected to bundle with one another to make "dimpled" surfaces.[133,134] These theoretical treatments of grafted polymer chains on a flat surface in unfavorable solvents may translate to the case

of nanoparticles coated with ligands that experience unfavorable enthalpic interactions with a host polymer, which acts as the solvent for the nanoparticles.

The studies presented here explore the dispersion of QDs in homopolymers in thin films, where the interfaces can play a role in the extent of QD dispersion. There are a number of forces that are believed to drive nanoparticle segregation to these interfaces; nanoparticles may displace polymer matrix chains to mitigate the conformational entropic loss of the host polymer chains experienced at the interface when $\chi = 0$.[135,136] Green also suggests that the entropic penalty of grafted ligands at the substrate is less than the entropic penalty experienced by the host polymer chains by drawing analogies to theoretical results demonstrating that multi-arm molecules absorb to surfaces more readily than their linear counterparts.[117,137] Chen and Green demonstrated that gold nanoparticles functionalized with polystyrene ligands aggregated near the interfaces of, or were dispersed, in a thin film of tetramethyl bisphenol-A polycarbonate polymer matrix based on the nanoparticle size and the relative length of the polystyrene ligands compared to polymer matrix chains.[138] In general, dispersion of the gold nanoparticles increased for larger ratios of $N_{ligand}/N_{polymer}$, and when the nanoparticle size was decreased (*i.e.* particles featured high curvature). These results were similar to a prior example of polystyrene-functionalized gold nanoparticles in a polystyrene thin film, where the localization of nanoparticles at the thin film interfaces was diminished via tuning the relative ratio $N_{ligand}/N_{polymer}$ and the nanoparticle size.[116] Typically, the driving force for dispersion of nanoparticles in the polymer matrix (as opposed to nanoparticle migration to the interfaces) is believed to be the gain in translational entropy of the polymer matrix chains upon mixing with the ligand chains (wet brush conditions) as well as the

translational entropy gain of (small) nanoparticles in no longer being confined to the interfaces.[117] When the enthalpic interaction between the nanoparticle ligands and the host polymer chain is favorable, the ligands shift towards a wet brush state, enabling mixing.

In this chapter, we explore QD dispersion in various homopolymers. The results from this chapter guide our selection of block copolymers chosen for QD composites (described in Chapter 5). The mixtures described here represent a variety of enthalpic interactions between the polymer matrix and the QD ligands, ranging from $\chi < 0$ to $\chi \approx 0.5$. As such, we frame the results in a dialogue of competing enthalpic and entropic forces dictating the extent of QD dispersion in different polymer matrices.

Section 4.1 – CdSe QDs in Poly(L-lactic acid)

This section explores the resulting structure of composites prepared from QDs in a poly(L-lactide) (PLLA) homopolymer, where the native ligands on the QD surface are not enthalpically driven to mix with PLLA. The ligands on the QD are non-polar alkane chains compared to the polar nature of PLLA. The resulting QD-homopolymer composites are studied using TEM.

4.1.1 Preparation of Composites

QD-polymer composites were prepared from dispersions of polymer and CdSe QDs in chloroform. A specific volume of QDs were dried from hexane after determining the QD concentration via absorbance.[89] A weighed quantity of PLLA was dispersed in chloroform and subsequently mixed with dried CdSe QDs at room temperature. The resulting QD-polymer mixture in chloroform was agitated to ensure mixing and quickly

dropcast onto carbon coated copper TEM grids in 1-2 uL portions. Care was taken to ensure the samples were dropcast immediately after mixing the QDs because the QDs are unstable in chloroform over time (see Chapter Three). The TEM grids were dried in air. Two PLLA homopolymers synthesized via ring-opening polymerization by Dr. Michael Maher were used: M_n = 21k g/mol and M_n = 12k g/mol.[139] These homopolymers are semicrystalline and feature a wide dispersity, based on their synthesis method.

4.1.2 Results

Micrographs of the prepared QD-polymer TEM grids are shown of 1 vol% CdSe QDs mixed with 21k g/mol PLLA (Figure 4.1) and 12k g/mol PLLA (Figure 4.2). Notably, there is some variance of structure in these micrographs for a given sample; the following images were chosen as representative of the range of structures observed across the entire grid. Fast Fourier transforms (FFT) of higher magnification images are also shown.

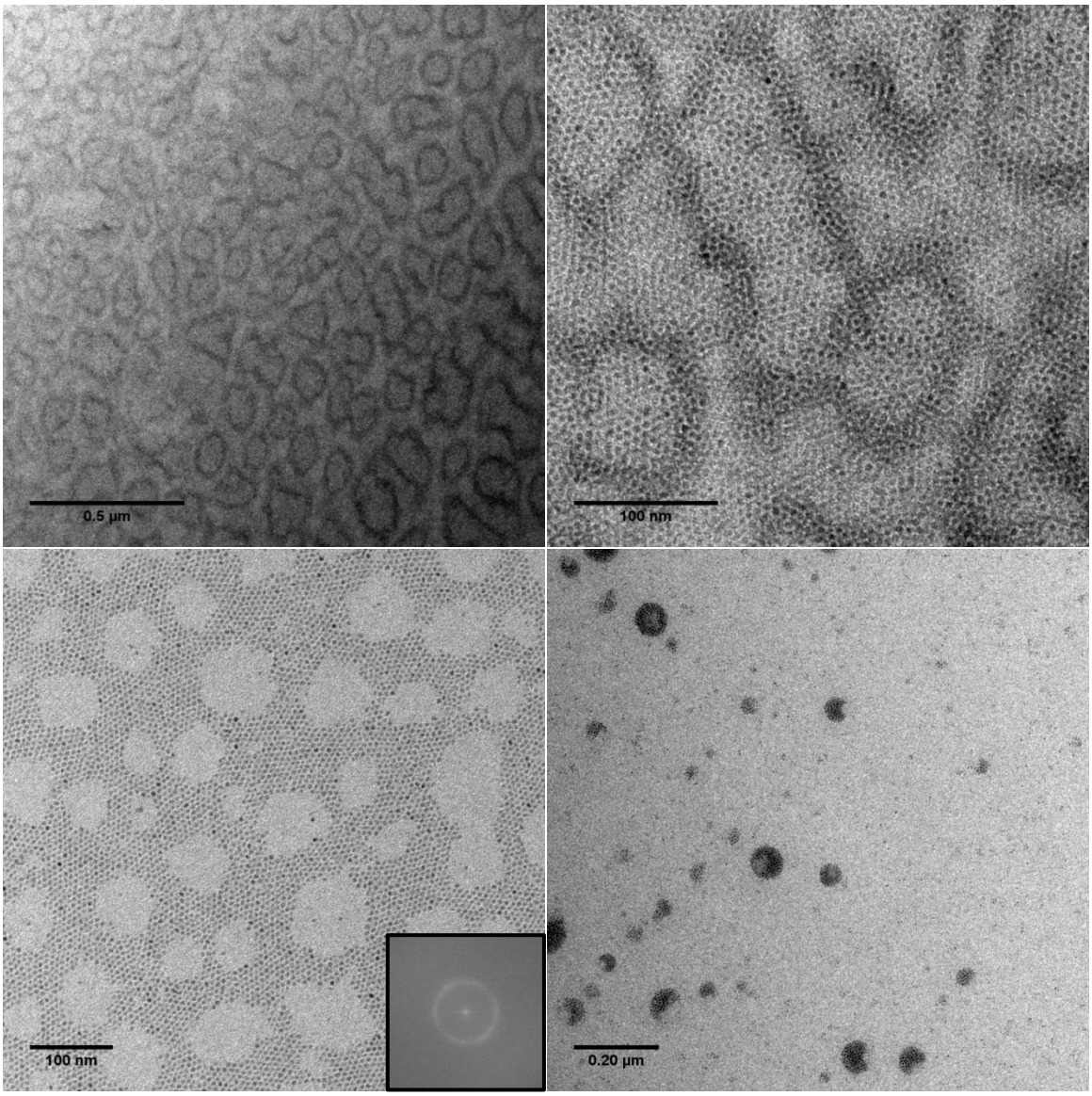

Figure 4.1: Micrographs of 1 vol% CdSe quantum dots with 21k g/mol poly(L-lactide) dropcast from chloroform. The fast Fourier transform of the bottom left image is shown in the bordered inset.

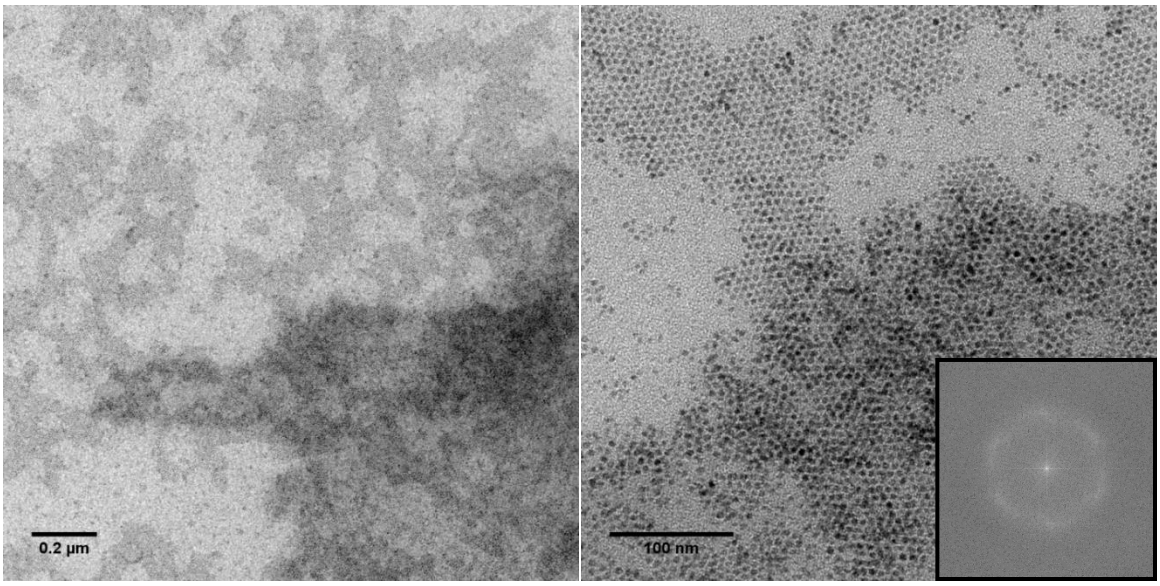

Figure 4.2: Micrographs of 1 vol% CdSe QDs with 12k g/mol poly(L-lactide) dropcast from chloroform. The fast Fourier transform of the right image is shown in the bordered inset.

Center-to-center spacing between QDs is given in Table 4.1. These results were obtained from averaging the FFT results from multiple micrographs.

Composite	Average Spacing between QDs
CdSe QDs (dropcast from hexane)	6.8 ± 0.4 nm
CdSe QDs with 21k g/mol PLLA	6.3 ± 0.1 nm
CdSe QDs with 12k g/mol PLLA	7.1 ± 0.5 nm

Table 4.1: Center-to-center spacing of 1 vol% CdSe QDs in 21k g/mol and 12k g/mol PLLA, as compared to neat QDs. These results were averaged from Fourier transforms of a series of micrographs.

4.1.3 Discussion

From the TEM images of both the 21k g/mol and 12k g/mol PLLA with QDs, it appears there is little mixing of QDs and polymer. The images largely show islands of QDs, with some QD layering apparent in the more concentrated areas of the TEM grids. The QD spacing (shown in Table 4.1) confirms that the spacing between QDs does not increase with the addition of the polymer. Thus, it is concluded that the polymer is

largely phase separated from the QDs. In the top images in Figure 4.1 of the 21k g/mol PLLA with QDs, the QDs appear to form a densely packed, single layer with irregular layering of additional QDs on top or bottom. This is attributed to the presence of the polymer; as the mixture of QDs and polymer in chloroform dries, some of the polymer may get trapped between sections of QDs, making this incomplete layer of the QDs appear to form rings.

Given the difference in chemical nature between the ligands on the QD surface and PLLA and the relative ligand length compared to matrix polymer chain length, it is unsurprising that the polymer failed to disperse the QDs. The ligands on the QD surface are nonpolar, saturated alkane chains (depicted in Figure 4.3) and are comparable to short poly(ethylene) (PE) chains. If we compare PLLA ($\delta = 9.9$ $(cal/cm^3)^{1/2}$) to PE ($\delta = 7.9$ $(cal/cm^3)^{1/2}$), PLLA is essentially a theta solvent for the PE ($\chi \approx 0.5$ using Eqn. 4.1).[114,140] In this case, the PLLA and the ligands do not experience favorable enthalpic effects upon mixing. However, the PLLA is not expected to swell the ligands, either. Here, $N_{polymer}$ is 166 (12k g/mol) and 291 (21k g/mol) for the two PLLA homopolymers. If we again compare the TOPO molecules decorating the QD surfaces to short, PE chains, each 8-carbon chain bound to the phosphorous group in the TOPO molecule is approximately $N_{ligand} = 4$ (or 12, if we consider all three carbon chains on a TOPO molecule). Thus, $N_{polymer} > N_{ligand}$. The grafting density of TOP and TOPO on the QD surface is approximately 1.6 nm^{-2}, based on the results described in Chapter Three (50 and 80 ligands per 1.6 nm radius and 2 nm radius QDs, respectively). Here we may draw analogies to a thin film system of gold nanoparticles with polystyrene ligands in a polystyrene matrix where $\chi = 0$ (thus, mixing is more favorable than in the $\chi \approx 0.5$ case

here), and the particle size (radius 2.2 nm, as compared to 2.3 nm here) and the grafting density (1.5 chains per nm^2, compared to 1.6 chains per nm^2 here) are comparable.[117,141] In this example, the nanoparticles phase separated to the interface when $N_{ligand} \approx 10$, acting like hard spheres. The conformational entropy gain of the polymer matrix chains in phase separating from the QDs is larger than the entropy loss of QD aggregation. Note that, given an average QD spacing of 6.8 nm and QD radius of 2.3 nm, we calculate a van der Waals attraction of roughly $0.5k_BT$ at room temperature, based on the Hamaker constant for CdSe particles in chloroform;[142,143] since this value is small in comparison to thermal fluctuation energy, we do not attribute the QD aggregation to van der Waals forces. The relatively high surface density (1.6 nm^{-2}) in combination with the short ligand length compared to the long polymer matrix chains is consistent with dry brush conditions. Thus, it is unsurprising that the TEM images here show also separation of the QDs and the PLLA.

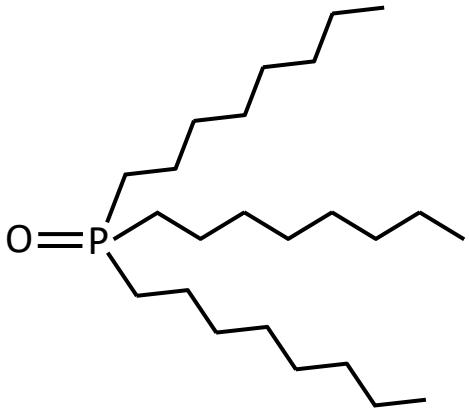

Figure 4.3: Cartoon schematic of trioctylphosphine oxide (TOPO). TOPO and trioctylphosphine (TOP, a molecule similar to TOPO without the oxygen) feature most prominently on the CdSe QD surface.

Section 4.2 – CdSe QDs in Poly(butadiene)

This section discusses the results of mixing QDs with a polymer that is similar in chemical nature to the ligands on the QDs' surface. The resulting composites are studied with TEM and fluorometry.

4.2.1 Preparation of Composites

A certain volume of QDs in n-hexane were dried based on the concentration of the QDs in hexane as determined via absorbance. Massed quantities of poly(1,4-butadiene) (1,4-PB) and poly(1,2-butadiene) (1,2-PB) were dispersed in n-hexane and subsequently added to dried QDs. The resulting QD-PB mixture in n-hexane was agitated and then dropcast in 1-2 uL portions onto carbon coated copper TEM grids. The TEM grids were allowed to dry in air. Two PB homopolymers were used: 1.1k g/mol 1,4-PB, and 1.3k g/mol 1,2-PB. These homopolymers were synthesized by Ronald Lewis via anionic polymerization.[144] Relevant characteristics are given in Table 4.2.

Polymer	M_n [g/mol]	% 1,4-PB	% 1,2-PB	Dispersity
1,4-PB	1100	88	12	< 1.1
1,2-PB	1300	11	89	< 1.1

Table 4.2: Characteristics of 1,4-poly(butadiene) and 1,2-poly(butadiene) homopolymers synthesized and characterized by Ronald Lewis. M_n was determined by proton NMR spectroscopy by end group analysis, 1,4-PB and 1,2-PB percentages were determined by proton NMR spectroscopy. Dispersity was estimated based on the synthesis procedure.

4.2.2 Results

Micrographs of the resulting QD-PB composites are shown for 0.5 vol% CdSe QDs in 1.1k g/mol 1,4-PB (Figure 4.4) and 1 vol% CdSe QDs in 1.3k g/mol 1,2-PB (Figure 4.5). Fast Fourier transforms of the images are included.

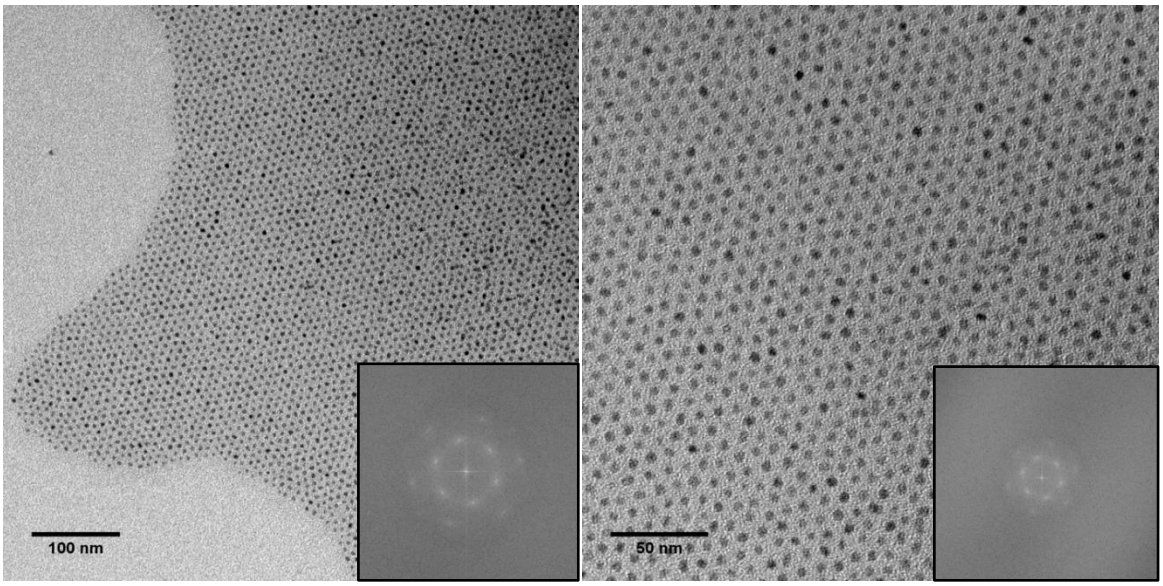

Figure 4.4: Micrographs of 0.5 vol% CdSe QDs in 1.1k g/mol poly(1,4-butadiene) dropcast from n-hexane, shown with corresponding fast Fourier transforms in the bordered insets.

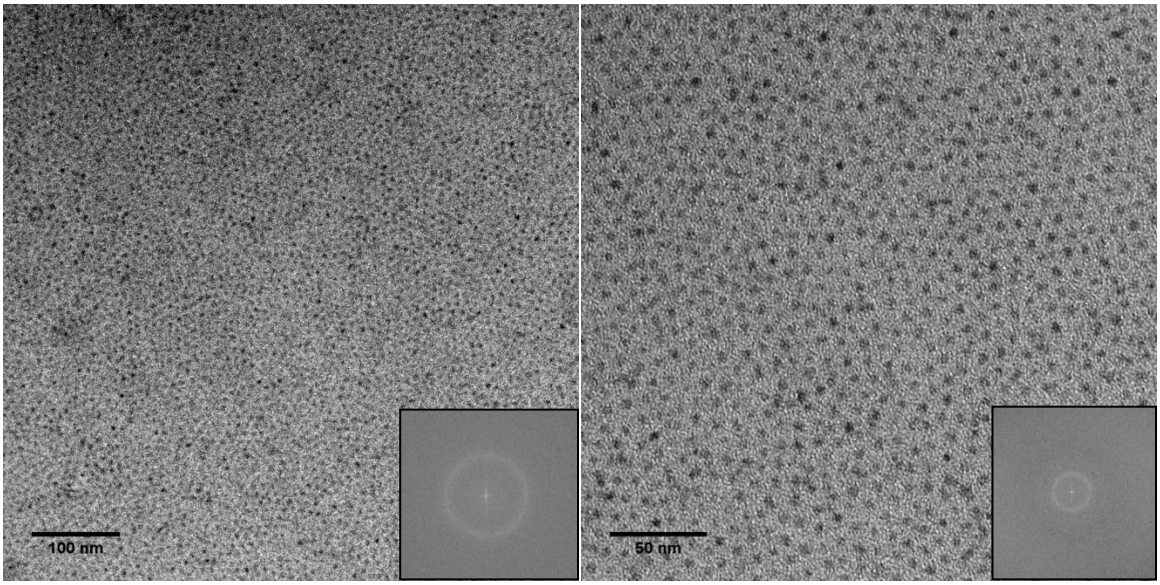

Figure 4.5: Micrographs of 1 vol% CdSe QDs in 1.3k g/mol poly(1,2-butadiene) dropcast from n-hexane, shown with corresponding fast Fourier transforms in the bordered insets.

Center-to-center spacing between QDs is given in Table 4.3 for neat QDs as compared to QDs dispersed in PB. These results were averaged from Fourier transforms of a series of micrographs.

Composite	QD center-to-center spacing
CdSe QDs (dropcast from hexane)	6.8 ± 0.4 nm
CdSe QDs with 1.1k g/mol 1,4-PB	8.7 ± 0.5 nm
CdSe QDs with 1.3k g/mol 1,2-PB	9.3 ± 0.1 nm

Table 4.3: Center-to-center spacing of 0.5 vol% CdSe QDs with 1.1k g/mol 1,4-poly(butadiene) and 1 vol% CdSe QDs with 1.3k g/mol 1,2-poly(butadiene), as compared to neat QDs. The results were taken from an average across Fourier transforms of multiple micrographs.

The fluorescence of the CdSe QDs in a 1,4-PB film (4 vol%) was measured using a Zeiss Axio Observer D1M microscope in conjunction with a Princeton Instruments IsoPlane ISO-160 spectrometer and a Princeton Instruments PIXIS:400B Digital CCD Camera and compared to CdSe QD films dropcast from n-hexane and CdSe QDs dispersed in n-hexane. The resulting emission curves are given in Figure 4.6; these curves are fit with Gaussian functions where the Gaussian fitting parameters are given in Table 4.4.

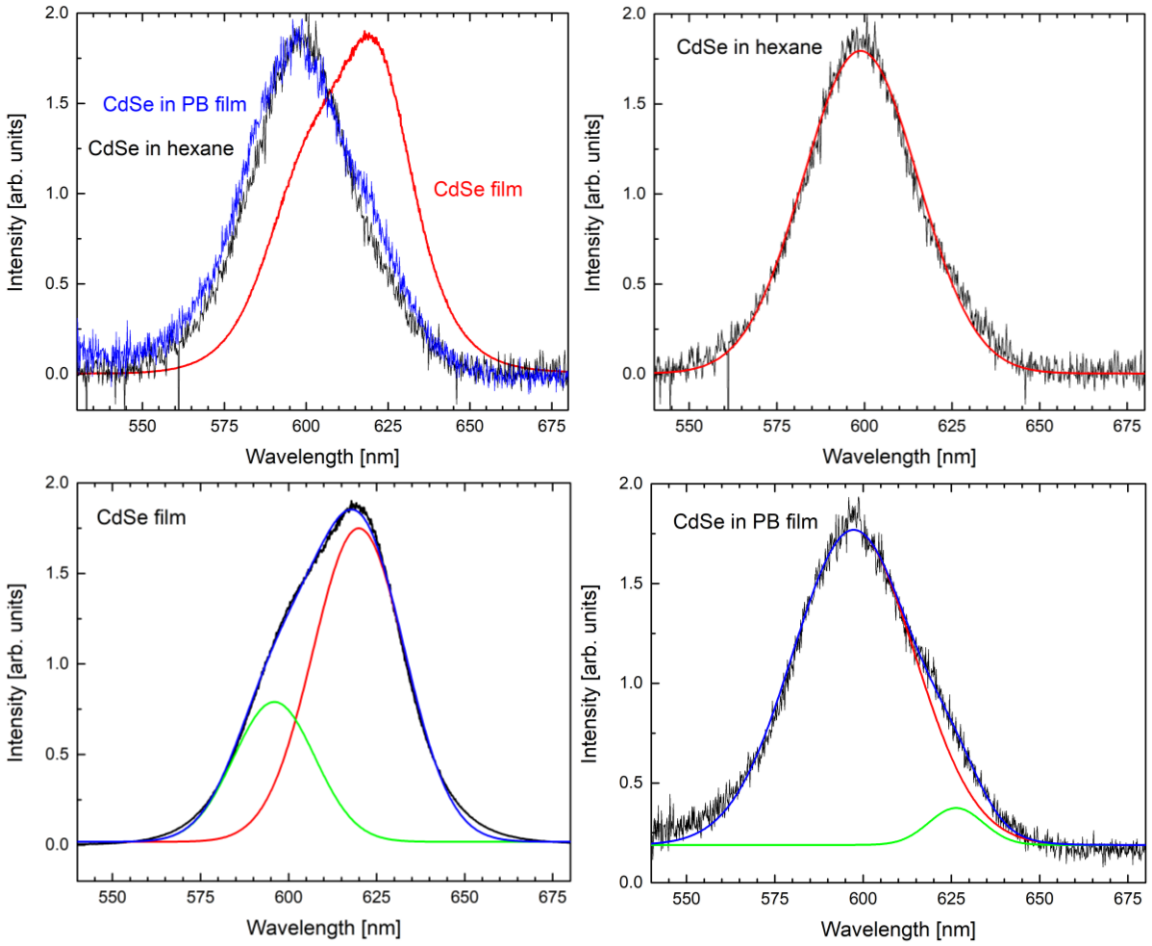

Figure 4.6: Fluorescence spectra of CdSe QDs dispersed in n-hexane, dried into a film, and dried from a solvent dispersion with 1,4-PB (4 vol%, 17 wt% CdSe QDs) (top left). Individual traces are shown (top right, bottom row) with Gaussian fits; individual Gaussian curves are shown in red and green where the resulting sum of the curves is given in blue. The spectra were normalized for comparison.

		CdSe in hexane	**CdSe film**	**CdSe in PB film**
Equation		$y = y_o + \frac{A}{w\sqrt{\pi/2}} e^{-2\left(\frac{x-x_c}{w}\right)^2}$		
Peak 1	y_o	0.004 ± 0.001	0.0181 ± 8×10^{-4}	0.00119 ± 1×10^{-5}
	x_c	598.90 ± 0.07	596.0 ± 0.3	597.3 ± 0.2
	w	32.7 ± 0.1	23.0 ± 0.3	34.6 ± 0.3
	A	73.4 ± 0.3	22.3 ± 0.7	0.432 ± 0.004
Peak 2	y_o	--	0.0181 ± 8×10^{-4}	0.00119 ± 1×10^{-5}
	x_c	--	620.0 ± 0.2	626.3 ± 0.5
	w	--	26.1 ± 0.2	15 ± 1
	A	--	56.7 ± 0.7	0.022 ± 0.003
R^2		0.967	0.998	0.988

Table 4.4: Gaussian fitting parameters for CdSe QDs in n-hexane, dried into a film, and dried from a solvent dispersion with 1,4-PB. The films are modeled as the summation of two Gaussians.

4.2.3 Discussion

From the micrographs and QD spacing information given in Table 4.3, the spacing between QDs increases in the presence of the PB. The QDs visually appear well-dispersed, and the QD center-to-center spacing increases on average by 1.9 nm and 2.5 nm when mixed with 1.1k g/mol PB and 1.3k g/mol PB, respectively. For comparison, the radius of gyration, R_g, of the two PB homopolymers is 1.3 nm for the 1.1k g/mol 1,4-PB and 1.2 nm for the 1.3k g/mol 1,2-PB, given statistical segment lengths of 0.69 nm for 1,4-PB and 0.59 nm for 1,2-PB.[114,145] For sufficiently large degrees of polymerization, $N \gg 1$, radius of gyration of a Gaussian coil is calculated as

$$R_g{}^2 = \frac{Nb^2}{6} \tag{4.2}$$

where b is the statistical segment length of the polymer. Thus, the change in spacing between QDs is on the same order of magnitude as the homopolymer diameter. Even in the extreme cases given the standard deviations in spacing, the QD spacing increases by a minimum of 1 nm (7.2 nm spacing for neat QDs vs. 8.2 nm spacing for 1.1k g/mol 1,4-PB), or as much as 3 nm (6.4 nm for neat QDs vs. 9.4 nm for 1.3k 1,2-g/mol PB). Interestingly, the face centered cubic morphology of QDs is retained in the 1.1k g/mol 1,4-PB composite. The six point FCC pattern is distinctly clear from the fast Fourier transforms shown in Figure 4.4. However, most of this order seems to be lost in the case of 1.3k g/mol 1,2-PB composite, as shown in Figure 4.5. Given the similarity in the chemical structure of PB and the ligands on the surface of the QDs, it is unsurprising that the PB has favorable enthalpic interactions with the ligands on the QD surface. The QD surface is largely decorated with trioctylphosphine oxide and trioctylphosphine ligands (Figure 4.3); if these ligands are again compared to PE ($\delta = 7.9$ $(cal/cm^3)^{1/2}$), PB is

similar in chemical nature ($\delta = 8.3$ $(cal/cm^3)^{1/2}$ for 1,4-PB and $\delta = 8.0$ $(cal/cm^3)^{1/2}$ for 1,2-PB); thus, recalling Equation 4.1, χ is close to 0. However, neither 1,4-PB or 1,2-PB disperses the QDs. While the spacing between QDs increases with the addition of PB, the total volume of PB represented by the increase in spacing is only a fraction of the total volume of PB in the mixture. If we consider $(6.8\ nm)^3$ (from Table 4.3) to represent 100% volume packing of neat QDs, the resulting mixtures of QDs with 1.1k g/mol 1,4-PB and 1.3k g/mol 1,2-PB are $(6.8\ nm / 8.7\ nm)^3 = 48$ vol% QDs and $(6.8\ nm / 9.3\ nm)^3 = 39$ vol% QDs, respectively. However, the mixtures of QDs in PB were prepared to 0.5 vol% QDs in 1.1k g/mol 1,4-PB and 1 vol% QDs in 1.3k g/mol 1,2-PB. Thus, the majority of the polymer is not found between the QDs. Here, two phases are formed: one ordered QD, or crystal, phase, where some small amount of PB has entered the ordered lattice and contributed to increased spacing between the QDs, and a second, neat polymer phase without QDs. Indeed, there are sections of the TEM grids immediately surrounding the QDs that do not contain QDs and are attributed to neat PB homopolymer; neat PB homopolymer may also phase separate and form a layer above or below the QD ordered phase. If roughly 100% of the QDs present in the mixture form the ordered phase (as is expected based on surveying the area of the TEM grid), only 1% of the total volume of 1,4-PB is present in the crystal QD phase (99% of the 1,4-PB is in the neat phase) for 0.5 vol% QDs with 1.1k g/mol 1,4-PB, and 3% of the total volume of 1,2-PB is present in the crystal QD phase (97% of the 1,2-PB is in the neat phase) for 1 vol% QDs with 1.3 k g/mol 1,2-PB.

In these mixtures, $N_{polymer} = 20$ (1.1k g/mol 1,4-PB) and $N_{polymer} = 24$ (1.3k g/mol 1,2-PB), again compared to $N_{ligand} = 4$. Thus, the ratio of $N_{ligand}/N_{polymer}$ is closer to 1 than

in the last example of QDs in PLLA, but still $N_{polymer} > N_{ligand}$. The ligand packing density on the QD surface is again 1.6 nm^{-2}. The presence of some PB around the QDs (evidenced by the shift in packing distance between QDs) may indicate that these QDs are somewhere in the transition from dry brush to wet brush conditions. At ideal wet brush conditions, the QDs would be well-dispersed throughout the PB matrices; however, given the entropic penalties of polymer chains fitting between dry brush particles, it is unlikely that the QDs are entirely in the dry brush state. Indeed, experimental studies of particles functionalized with polymer ligands in a polymer matrix of the same type noted transitions from dispersed composites to aggregated particles when $N_{polymer}/N_{ligand}$ was 4, for 13.4 nm radius silica particles with polystyrene ligands in a polystyrene matrix[146] or when $N_{polymer}/N_{ligand}$ was 5 – 6 for 5 nm radius silica nanoparticles with poly(ethylene glycol) ligands in a poly(ethylene glycol) matrix.[147] Two separate studies on gold nanoparticles demonstrated a transition phase from dispersion to aggregation over $3 < N_{polymer}/N_{ligand} < 8$ for 2.4 nm gold particles with polystyrene ligands in a polystyrene matrix,[141] and over $4 < N_{polymer}/N_{ligand} < 10$ for 3 nm gold particles with polystyrene (or poly(methyl methacrylate)) ligands in a polystyrene (or poly(methyl methacrylate) matrix.[119] These intermediate phases were characterized by the beginning of nanoparticle aggregated conglomerates in the polymer matrix. Thus, given our ratio of $N_{polymer}/N_{ligand} \approx$ 5-6 and $\chi \approx 0$ between the ligands and the PB matrix, this system is expected to be in the intermediate phase between dry and wet brush conditions.

The capacity for polymers to mix with the ligand shell is in part diminished by the ligand shape. The TOPO and TOP molecules' branched structure results in a conal shape where the top of the cone is localized at the QD's surface and the broader base occupies

space away from the QD surface (a more detailed description is given in Chapter Three). Thus, this short and rigid structure cannot stretch to create space near the QD surface like a linear polymer chain can to accommodate mixing of polymer matrix chains. In short, the ligand structure, although well-designed for dispersing QDs in various nonpolar solvents, may prove detrimental to developing wet brush conditions where the longer (compared to solvent molecules) host polymer chains may wet and mix with the ligands.

The QD fluorescence is dependent on the QD surface states. QDs in dispersion are well isolated (at dilute QD concentrations) and when excited, emit light at a given wavelength. This behavior is evident in the example of QDs in hexane given in Figure 4.6 where the QDs exhibit a single, symmetric peak in the emission spectra at $\lambda \approx 599$ nm. However, the QDs, once dried into a film, or when incorporated in PB, demonstrate a red-shift in fluorescence and exhibit two peaks (or a primary peak with a broad shoulder). In Figure 4.5, QDs dried in a film exhibit a shift in the dominant peak to $\lambda \approx 620$ nm, with a broad shoulder peaking at $\lambda \approx 596$ nm. When the QDs are dried with PB, the emission spectrum shows a primary peak at $\lambda \approx 597$ nm, with a broad shoulder at longer wavelengths ($\lambda \approx 626$ nm). This behavior is often attributed to QD aggregation and trap emission.[16,148,] One potential cause is the oxidation of the QD surface; in the case of neat QD films, the surface is prone to oxidation over time, resulting in surface trap states that lower the emission energy.[149,150] However, when the QDs are incorporated in a PB matrix, the polymer may help prevent QD surface oxidation and/or help passivate the QD surface. This would explain the significant change in emission energy between the neat QD film and QDs dispersed in a PB matrix.

Section 4.3 – CdSe-PEG in Poly(L-lactic acid)

This section explores the results of mixing CdSe functionalized with PEG ligands with poly(L-lactic acid). The QDs used in this study were prepared in the same manner as described in Chapter Three. PLLA has been previously shown to favorably interact with PEG, given the negative Flory-Huggins interaction parameter between PLLA and PEG ($\chi < 0$).[151]

4.3.1 Preparation of Composites

CdSe-PEG QDs were prepared as described in Chapter Three, and verified to be well-dispersed in chloroform via DLS. A small volume (~200 μL) of dilute CdSe-PEG in chloroform (~0.5 micromolar) was added to ~3 mg of PLLA. The resulting dispersion was agitated to ensure mixing, and then 1-2 μL was dropcast onto a carbon-coated copper TEM grid. The TEM grids were allowed to dry in air. CdSe QDs were mixed with a 12k g/mol PLLA homopolymer and a 21k g/mol PLLA homopolymer. The homopolymers used in this study were the same described in section 4.1.

4.3.2 Results

Micrographs of the PEG-functionalized CdSe QDs in PLLA are shown for 12k g/mol PLLA (Figure 4.7) and 21k g/mol PLLA (Figure 4.8).

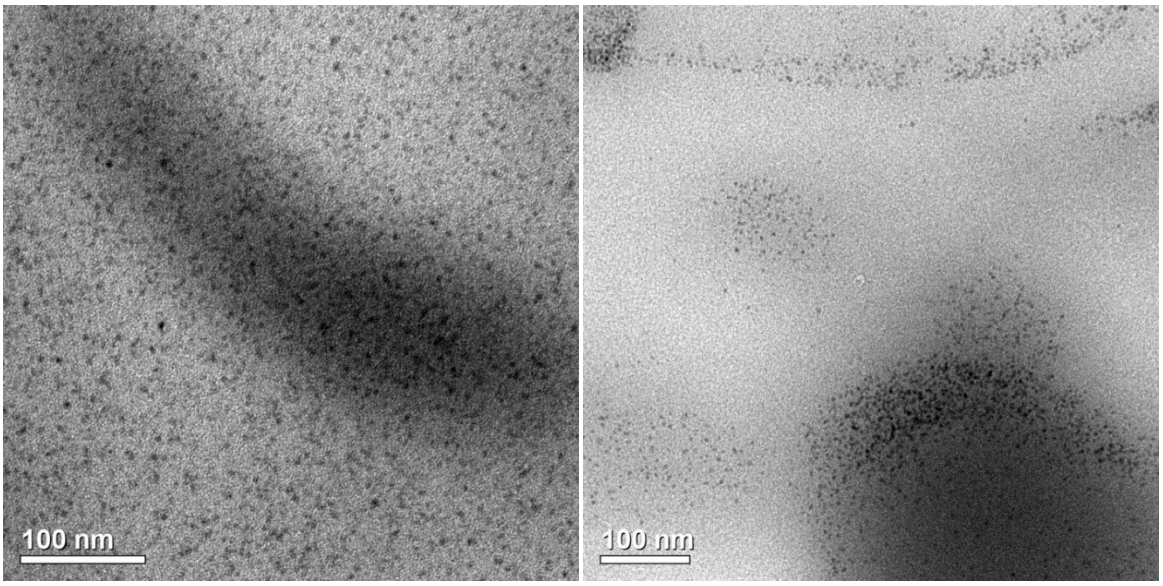

Figure 4.7: Micrographs of 0.4 vol% CdSe QDs functionalized with poly(ethylene glycol) in 12k g/mol poly(L-lactide) dropcast from chloroform onto carbon coated copper TEM grids.

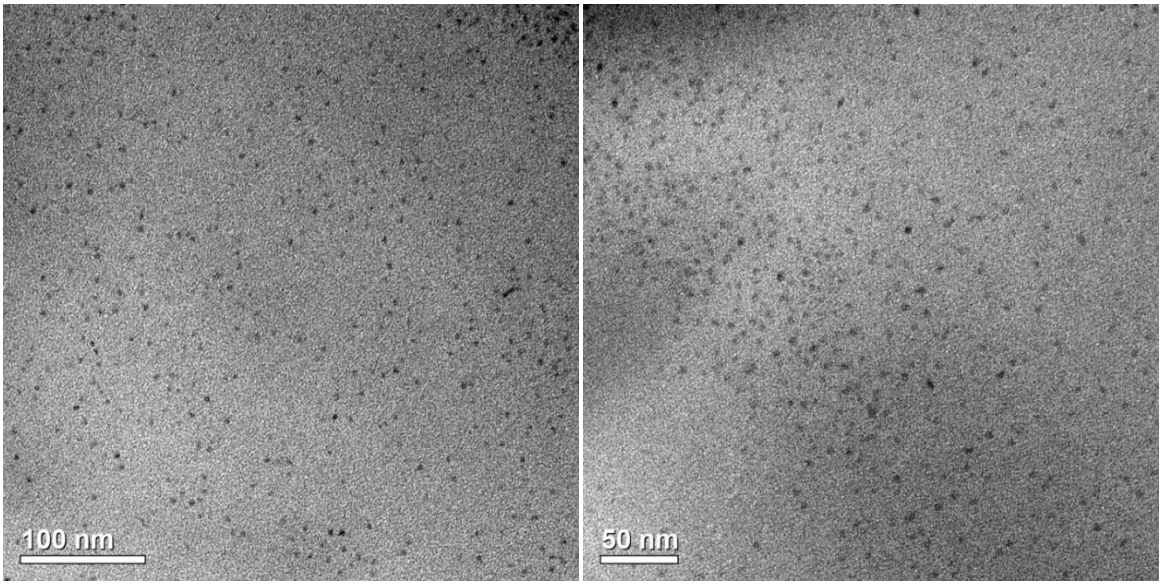

Figure 4.8: Micrographs of 0.4 vol% CdSe QDs functionalized with poly(ethylene glycol) in 21k g/mol poly(L-lactide) dropcast from chloroform onto carbon coated copper TEM grids.

For reference, micrographs of CdSe QDs functionalized with poly(ethylene glycol) without PLLA are shown in Figure 4.9.

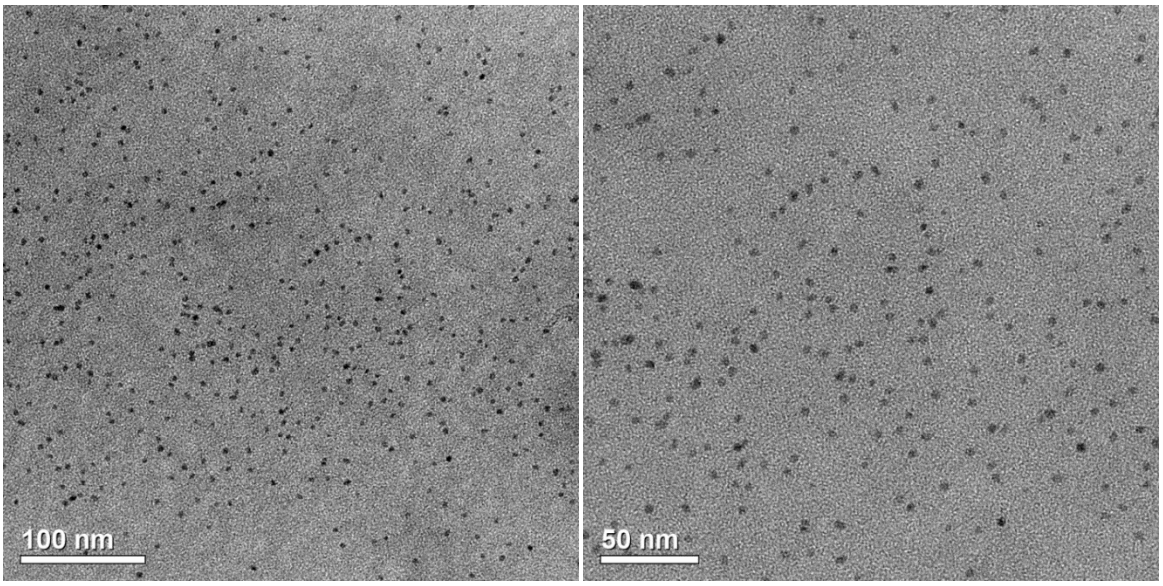

Figure 4.9: Micrographs of CdSe QDs functionalized with poly(ethylene glycol) dropcast from chloroform onto carbon coated copper TEM grids.

4.3.3 Discussion

At first impression, there is little difference in the micrographs of PEG-functionalized CdSe QDs with or without PLLA. In all cases, there is no clear order between QDs. However, in the case of CdSe QDs mixed with 12k g/mol PLLA, groupings or lines of QDs are apparent in some images (Figure 4.7). These groupings and lines tend to follow darker sections of the image, which are associated with an area of thicker film. In general, the number of electrons that passes through the film to compose an image depends on the electron density of the material measured as well as the thickness of the material. Thus, the large, darker areas on these micrographs are attributed to thicker sections of PLLA. For comparison, consider the case of CdSe QDs without the presence of PLLA (Figure 4.9): the background is relatively uniform, unlike the examples given in Figure 4.7. In Figure 4.7, the density of QDs per projected area is higher in the darker sections of these films as compared to the density of QDs per projected area in the

lighter regions. This suggests that the QDs are either dispersed in the PLLA, or decorate the PLLA surfaces. In the former case, the QDs should appear uniformly, but randomly, dispersed in the darker regions, whereas in the latter case, the number of QDs on the edge of the darker regions should increase as the TEM captures a projected image of the film. Interestingly, there appear to be examples of both in Figure 4.7. In the left micrograph, the QDs appear randomly dispersed all over the darker region in the middle, without any increase in QD density near the edges of the darker region. In the right micrograph, however, there is a congregation of QDs near the edge of the bottom right darker region. Thus, it is possible both circumstances are represented in this film: in some areas, the QDs disperse randomly in the PLA, whereas in other areas, the QDs are confined closer to the PLA surfaces.

It is important to recall that the ligand exchange process of PEG for native trioctylphosphine and trioctylphosphine oxide ligands on the QD surface is incomplete. In general, 15-50% of the original ligands remain on the QD surface, and only 2-4 PEG ligands attach to each QD. As such, the ligand density is lower for CdSe QDs functionalized with PEG than as-synthesized CdSe QDs with TOPO and TOP ligands. In general, as the ligand density decreases, depletion interactions and van der Waals forces may induce particle aggregation.[152] However, based on the results shown in Figure 4.7 and Figure 4.8, some QD dispersion is achieved. The reduction in ligand coverage may enable better host polymer chain mixing with the remaining ligand shell, which would be consistent for wet brush conditions where the polymer matrix chains are longer than the ligands. As before, $N_{polymer}$ is 166 (12k g/mol) and 291 (21k g/mol), compared to the $N_{TOPO/TOP} = 4$ and $N_{PEG} = 45$. One recent study on polydisperse nanoparticle brushes

suggests that polydisperse ligands may help stabilize particles in polymer matrices as compared to monodisperse ligands by creating a broader ligand interface for polymer matrix chain mixing.[119] When the ligands are polydisperse, the longer ligands can extend further than the short ligands on the particle surface, enabling space near the particle surface for polymer matrix chain wetting, thus delaying the transition from wet brush to dry brush for increasing ratios of $N_{polymer}/N_{ligand}$. Enthalpically, the host polymer matrix is driven to mix with the PEG chains on the QD surface, owing to the negative χ between PLA and PEG.[151] The PEG molecules on the QD surface are thus expected to swell like they do in solvents like chloroform (Chapter Three). The remaining TOPO/TOP do not feature favorable enthalpic interactions with PLLA (as discussed in section 4.1), but they are now less densely packed on the QD surface, allowing better host polymer mixing near the QD surface. Unfortunately, given the random nature of the neat QDs functionalized with PEG and the inability to definitively identify the PLLA in these micrographs, it is difficult to truly assess the level of dispersion of PEG-functionalized QDs in PLLA.

Section 4.4 – Summary & comparison of QD dispersion in homopolymers

The results discussed in this chapter help guide selection of block copolymers in which to test QD dispersion (as described in Chapter Five). Through the experiments detailed in this chapter, we confirm that CdSe QDs functionalized with native ligands trioctylphosphine (TOP) and trioctylphosphine oxide (TOPO) do not disperse in poly(lactic acid) owing to the enthalpic penalties associated with mixing and the QDs acting essentially like hard spheres in the long chain polymer matrix. When the native ligands are partially exchanged for poly(ethylene glycol), the QD dispersion in PLLA

improves to some degree. The small number of PEG molecules on the QD surface (2-4 per QD, on average) is sufficient to better balance the enthalpic interactions between QD ligands and host polymer. This mimics the behavior seen in Chapter Three, where PEG functionalized QDs disperse well in polar solvents as the PEG ligands swell to block some of the unfavorable enthalpic interactions between the remaining native ligands and the solvent. Reduced ligand density may also enable better host polymer chain mixing in the ligand shell. An intermediate case between complete phase separation and dispersion is observed for CdSe QDs with native ligands in homopolymer PB. In these composites, the native ligands (TOP and TOPO) do not experience strong enthalpic penalties for mixing with PB. However, the ideal wet brush condition is not achieved, as observed by the lack of complete dispersion of QDs in the PB matrix. Regardless, the simpler interactions between TOPO/TOP and polymer matrices (as compared to the multi-faceted CdSe functionalized with PEG, where enthalpic interactions are complicated by remaining TOPO/TOP ligands) provide a robust system for study of QD dispersion in polymers. Thus, QDs functionalized with their native ligands were the primary subject of study for block copolymer-QD composites. These studies are detailed in Chapter Five.

Chapter Five – CdSe Quantum Dots in Diblock Copolymers

The dispersion of nanoparticles or quantum dots in block copolymer matrices has been demonstrated to varying degrees of success. Many methods utilized in these studies rely on specific chemistry between the polymer system and the ligands on the particle surface, which can make them difficult to adapt to new materials.[27,57,80,153] While some theoretical studies offer insight into the governing forces dictating dispersion or aggregation of particles in block copolymer matrices, the path dependency of reaching dispersed states is largely uncharted.[76,118,154] Furthermore, most experimental studies have focused on the integration of particles in a lamellar polymer morphology, which face different entropic constraints of space filling than sphere-forming polymer morphologies.[66,69]

In Chapter Four, we discussed several parameters which continue to be relevant here, including enthalpic interactions between ligands on the QD surface and the polymer matrix (χ), the relative ligand length compared to the polymer matrix chain length, and ligand surface density. Here, we consider more complex systems of QDs in block copolymer matrices, where polymer phase morphology and interactions between the block components also play a role in the resulting composite. We discussed the overarching enthalpic and entropic interactions dictating nanoparticle dispersion in block copolymers in Chapter One and use this as a framework for our work presented here.

A range of theoretical treatments and modeling techniques have been utilized to predict the extent of nanoparticle dispersion in block copolymer matrices, including molecular dynamics,[75] Monte Carlo simulations,[154,155] dissipative particle dynamics,[156-158] and combined self-consistent field theory and density functional theory.[73,159-165] Early

studies considering the dispersion of hard particles in a lamellar diblock copolymer matrix indicated that particle size and particle preference for a given polymer block component dictated particle location in the polymer matrix.[74,166] When the particle prefers block A of an A-B diblock copolymer (*i.e.* the Flory Huggins interaction parameter $\chi_{A\text{-particle}} = 0$, whereas $\chi_{AB} = \chi_{B\text{-particle}} \neq 0$), large particles (particle radius = $0.3bN^{1/2}$, where b is the polymer statistical segment length and N is the degree of polymerization) are localized in the center of the A-block lamellae domain, whereas smaller particles (particle radius = $0.15bN^{1/2}$) are localized near the interface between A and B; this is attributed to different entropic competitions.[73] When the particles are large, the conformational entropy losses of polymers stretching to accommodate the hard spheres are minimized when the particles reside in the center of the A block lamellae. The placement of large spheres in the center of the compatible domain allows polymer chains to move apart to accommodate particles, instead of forcing polymer chain stretching. When the particles are small, the translational entropy gain of the particles outweighs the diminished polymer conformational entropy losses. As the particle volume fraction is increased, the large particles become more strictly localized to the center of the A block lamellae, whereas the smaller particles are more uniformly dispersed across the A domain. When the particle does not prefer either polymer block, the particles are localized at the interface between lamellae forming block copolymers.[157,163]

These theoretical predictions have generally been consistent with experimental results.[74,115,167,168] Iron oxide particles functionalized with polystyrene ligands in a symmetric poly(styrene-*b*-butylmethacrylate) polymer matrix were observed at the interfaces of the lamellae for small particles (4 nm diameter) and at the center of the

polystyrene lamellae domains when the particle diameter was increased to 6 nm.[169-171] When 3.5 nm diameter gold and 21.5 nm diameter silica nanoparticles were added to a poly(styrene-*b*-ethylene propylene) polymer, the small gold particles were observed at the interfaces between the domains, whereas the larger silica particles were primarily localized in the center of the poly(ethylene propylene) domain.[66] Here, the authors indicate the ligands on the particles' surfaces should drive them to favor poly(ethylene propylene). Another study on gold nanoparticles functionalized with polystyrene in a poly(styrene-*b*-ethylene propylene) polymer demonstrated the expected random dispersion of particles in the preferred block domain, as predicted for higher volume fractions of particles.[172]

Additional experimental studies have demonstrated the effect of ligand type on nanoparticle dispersion in block copolymers. Gold nanoparticles with polystyrene ligands were observed in the center of the polystyrene lamellae domain in a poly(styrene-*b*-2-vinyl pyridine) polymer matrix, whereas gold nanoparticles with a mixture of polystyrene and poly(2-vinyl pyridine) ligands were found at the polymer domain interface.[69] This result highlights the potential tunability of particle placement: by careful and quantitative ligand exchange, a given size of nanoparticles may be manipulated to reside in specific regions of a polymer morphology. In a study on titanium dioxide particles in a poly(styrene-*b*-methyl methacrylate), the particles dispersed in the poly(methyl methacrylate) (PMMA) domain when particles were functionalized with ligands featuring favorable enthalpic interactions with the PMMA. When the particles were ionically functionalized with ligands preferring the polystyrene domain, the particles were found in small aggregates in the polystyrene domain. Here, the aggregation was attributed to the

ionic bonds allowing rearrangement of the ligands, leading to aggregation during the drying process.[173] Finally, gold nanoparticles were found to uniformly disperse in the polystyrene domain of a poly(styrene-*b*-ethylene propylene) polymer, or to localize at the interface between the lamellae domains, depending on the gold particle surface ligands.[174] In many of these studies, the enthalpic interactions between the ligands and the polymer matrix help guide particle dispersion, where the relative particle size dictates whether the particles are confined to the interfaces between polymer domains (small particles), confined to the center of a given polymer domain (large particles), or randomly dispersed in a polymer domain (small particles, more often at large volume fractions). Here, the qualification of small and large particles is made in reference to the polymer domain size and varies considerably from experiment to experiment. In general, when the particle diameter approaches ~0.15 to 0.5 of the domain size, the particle is considered large.[63,73,80,169,175]

Overall, many studies have focused on symmetric, or near symmetric, diblock copolymers, where the polymer typically exhibits lamellar structure. The investigation of sphere-forming block copolymer composites is comparatively lacking. Our work here begins with an exploration of CdSe QDs in a lamellae-forming block copolymer where the ligands on the QD surface are expected to demonstrate favorable enthalpic interactions ($\chi < 0.5$) with both polymer components. Following, we explore different routes towards QD-block polymer composites in sphere-forming polymers in bulk structures as well as thin films. As part of this investigation, we pursue a novel method for effective integration of QDs in a block copolymer via polymer micellization.

In this chapter, we explore the integration of quantum dots in block copolymers by formation of bulk composites and thin films using various polymers.

1) In the first section we consider the resulting structure of a composite formed by mixing QDs with a lamellar-forming poly(ethylene)-*b*-poly(cyclohexylethylene) and subsequently heating the composite to order the polymer with the QDs present.
2) In the second section we explore differences in QD dispersion by examining QD-polymer composites made from mixing QDs with a sphere-forming poly(styrene)-*b*-poly(1,4-butadiene) polymer and ordered at an elevated temperature as compared to films of the same QD-polymer mixture dried from dispersion.
3) In the third section we investigate the formation of inverted poly(lactic acid)-*b*-poly(1,4-butadiene) polymer micelles in dispersion and whether the inversion of the micelles during the drying process can capture QDs inside polymer sphere forming phases.

Section 5.1 – CdSe in Poly(ethylene)-*b*-Poly(cyclohexylethylene)

This section addresses the result of mixing CdSe QDs with a polymer where both polymer components are similar in chemical nature to ligands on the QD surface. A composite is prepared by drying the QD-polymer mixture from dispersion, heating the composite above the polymer T_{ODT}, and then slowly cooling the composite to an appropriate temperature to induce polymer ordering.

5.1.1 Neat Polymer Characteristics

The poly(ethylene)-*b*-poly(cyclohexylethylene) (PE-*b*-PCHE) block copolymer used in these studies was synthesized by Dr. Robert Hickey, Dr. Brian Habersberger, and Dr. Timothy Gillard.[176,177] Important PE-*b*-PCHE characteristics are given in Table 5.1.

PE-*b*-PCHE	M_n	f_{PCHE}	T_{ODT}
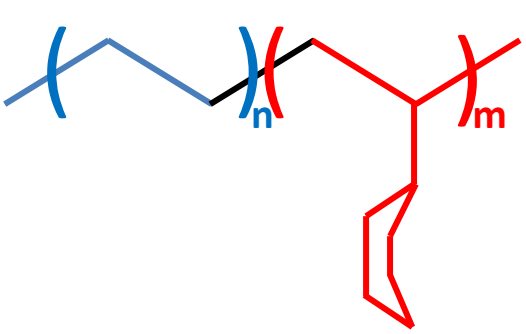	**13.6 kg/mol**	**0.52**	**189°C**

Table 5.1: PE-*b*-PCHE characteristics; all were experimentally measured by Dr. Robert Hickey, Dr. Brian Habersberger, and Dr. Timothy Gillard. M_n was determined from size exclusion chromatography, volume fraction, *f*, was determined via proton nuclear magnetic resonance spectroscopy using the melt densities at 140°C[178], and T_{ODT} was determined from dynamic mechanical spectroscopy on heating (1°/min).

The polymer is expected to form lamellae based on the approximately symmetric volume fraction (f_{PCHE} = 0.52).[40] The lamellar structure is confirmed by the peak locations in a SAXS measurement, shown in Figure 5.1. The peaks occur at integer multiples of q^*, the location of the first peak, which is consistent with lamellar morphology. In general, the ratio of peaks with respect to q^* is indicative of the underlying morphology. The peaks in Figure 5.1 are narrow, indicating nearly uniform domain lengths in a well-ordered structure. The morphology domain length, L, is related to the scattering vector at the first peak:

$$q^* = \frac{2\pi}{L} \tag{5.1}$$

The data in Figure 5.1 gives a domain length of 17 nm from q^* = 0.037 Å^{-1}.

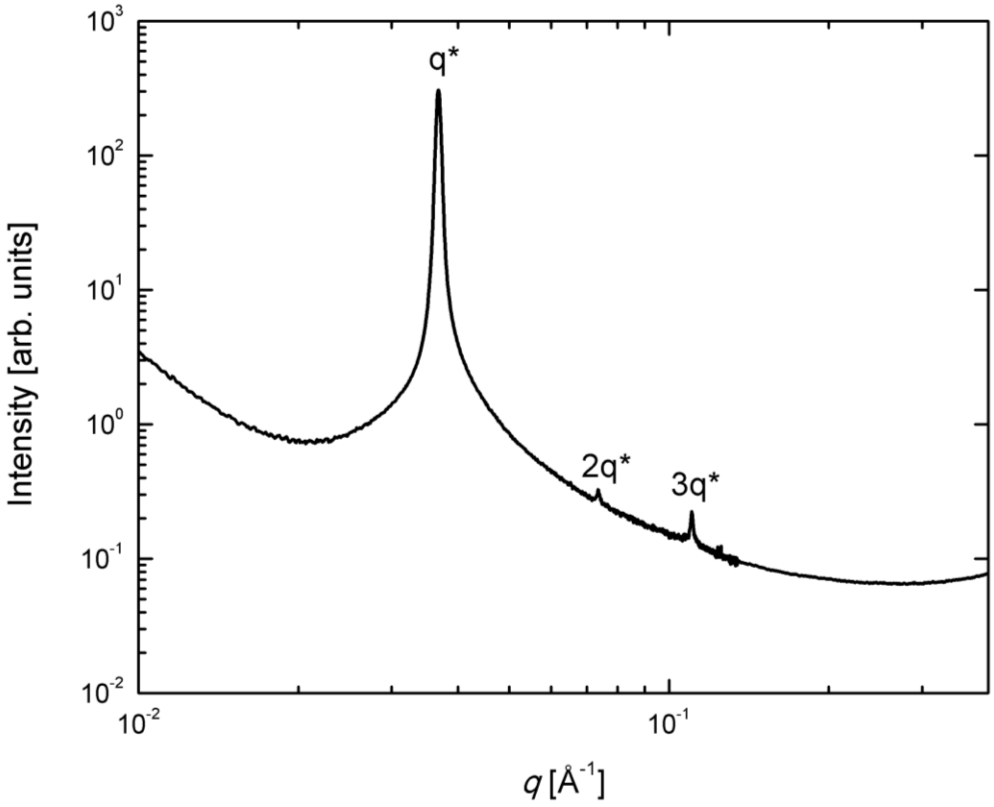

Figure 5.1: Synchrotron SAXS data of PE-*b*-PCHE polymer taken at T = 140°C with a source beam wavelength λ = 0.756 nm. The higher *q* angles are labeled with respect to $q^* = 0.037$ Å^{-1}.

5.1.2 Composite Preparation

Four concentrations of CdSe QDs in PE-*b*-PCHE were prepared: 1.1 wt%, 2.9 wt%, 7.6 wt%, and 18 wt%. Massed quantities of PE-*b*-PCHE and dried QDs were dispersed in benzene and heated to ~85°C to solubilize the polymer. The dispersion at this temperature appeared clear and colored orange, indicating good mixing. The dispersion was then quickly frozen in liquid nitrogen to preserve the random mixing. The resulting solid mixture was transferred to a vacuum oven to allow the benzene to sublime at low pressure. At this stage, the solid was porous, orange, and opaque. The sample was then heated above the polymer T_{ODT} under vacuum to produce a denser and less porous solid.

For SAXS measurements, the samples were then cooled and ground into a fine powder. The powder was transferred into closed-end quartz capillaries. The capillaries were subsequently heated above T_{ODT} under vacuum to allow polymer flow to fill the bottom of the capillaries. The melt at this stage appeared orange and translucent. To further induce sample movement to the bottom of the capillary, the capillaries were removed from the oven and briefly centrifuged for ~10 seconds before being returned to the oven. The vacuum oven was then cooled from T ≈ 200°C to T = 140°C at a rate of <1 °/min. The samples were held under vacuum at 140°C for ~15 hours to allow for polymer ordering. Afterwards, the samples were removed and quenched to room temperature to preserve the ordered polymer state (glass transition temperatures: $T_{g,PCHE}$ = 140°C and $T_{g,PE}$ = -120°C, melting temperature: $T_{m,PE}$ = 135°C). At this stage, the 1.1 wt%, 2.9 wt%, and 7.5 wt% samples appeared uniformly orange and transparent. The highest concentration sample (18 wt%) was similarly orange but appeared translucent. All samples exhibited fluorescence uniform to the naked eye under UV illumination.

For TEM measurements, the remaining composite solid of the 1.1 wt% CdSe in PE-*b*-PCHE was heated under vacuum above T_{ODT}. The sample was then cooled to T = 140°C and held at this temperature for ~ 15 hours before being quenched to room temperature. Afterwards, a small piece of colored and transparent composite was imbedded in epoxy and microtomed to form thin film sections ~100 nm thick. The film sections were floated on water and transferred onto copper TEM grids for study.

5.1.3 Results

The CdSe QD and PE-*b*-PCHE composites in capillaries were studied with SAXS (Figure 5.2). The samples were heated to 140°C on the beamline. The source had a beam wavelength of λ = 0.756 nm.

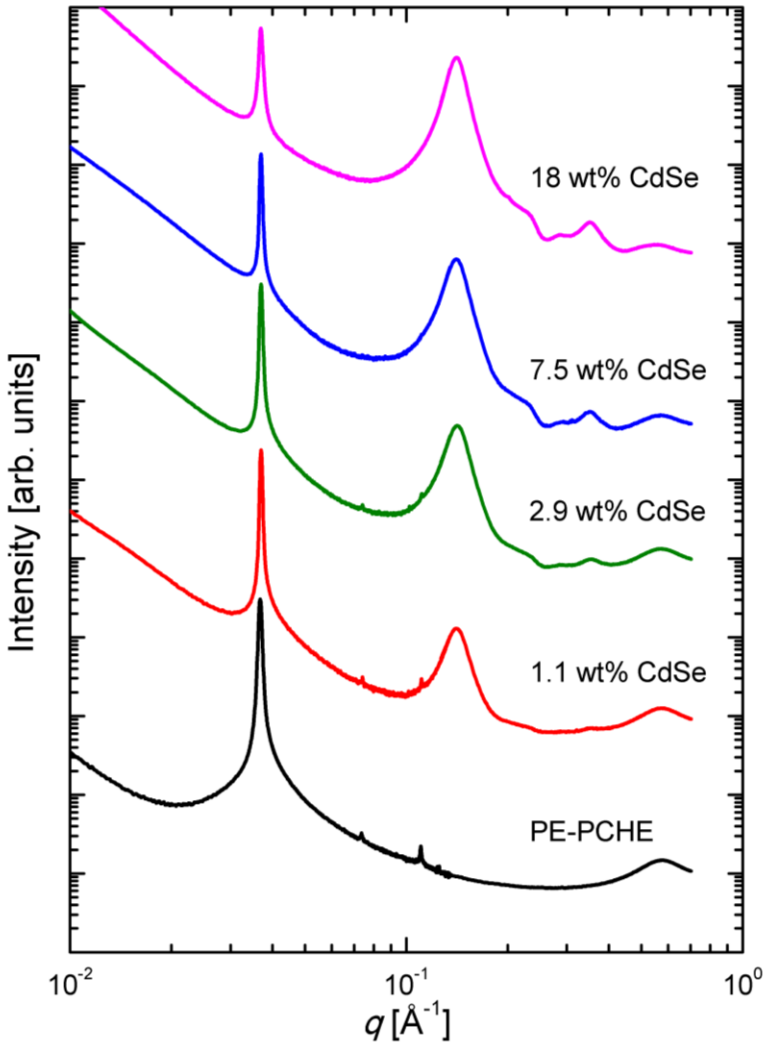

Figure 5.2: SAXS patterns of neat PE-*b*-PCHE polymer and various concentrations (1.1 wt%, 2.9 wt%, 7.5 wt%, and 18 wt%) of CdSe QDs in PE-*b*-PCHE matrix. The beam source λ = 0.756 nm and the data was taken at T = 140°C. The data is vertically shifted for clarity.

The microtomed films of QD-polymer composites were examined via TEM. Micrographs of the 1.1 wt% CdSe in PE-*b*-PCHE matrix are shown in Figure 5.3. In

general, these films were difficult to image as they were prone to beam damage over time and at higher resolutions. Seams and air pockets in the solid composite also provided starting points for cracks in the polymer film, resulting in damaged and curled films. Note that the horizontal lines evident in the lower resolution TEM micrograph are a result of the microtoming process and not indicative of the polymer structure.

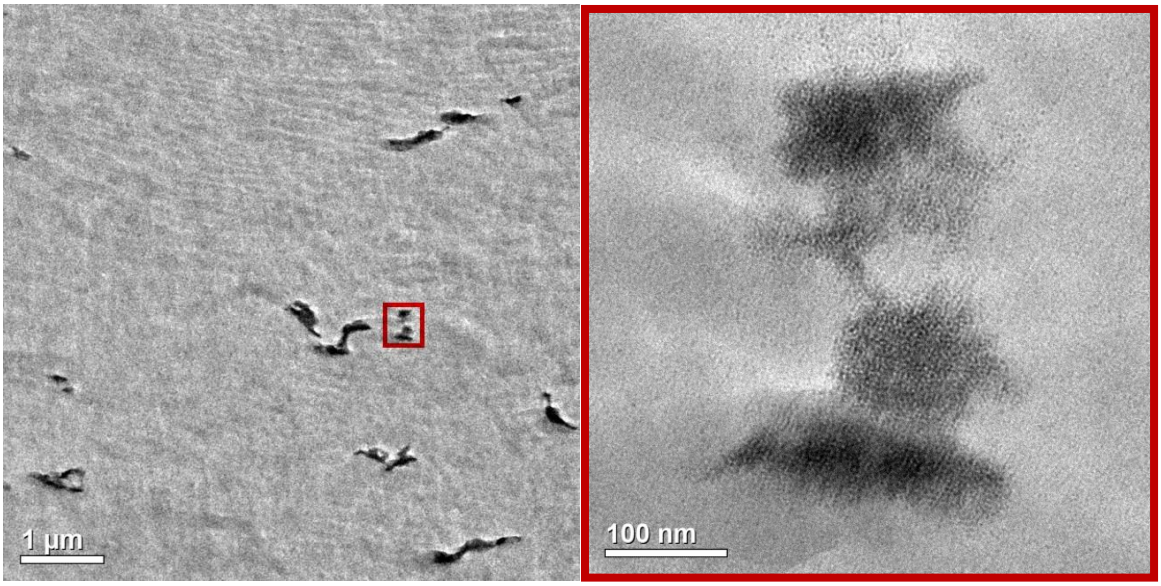

Figure 5.3: Micrographs of microtomed sections of 1.1 wt% CdSe QDs in PE-*b*-PCHE matrix. The films here were microtomed from a bulk composite formed at T = 140°C.

5.1.4 Discussion of Composite Structure

The lamellar morphology of the PE-*b*-PCHE polymer is maintained at each concentration of CdSe QDs, as confirmed by the persistence of the peaks associated with integer values of q^* (Figure 5.2). However, a broad peak at higher q = 0.14 Å^{-1} appears upon addition of QDs and grows larger with higher QD concentration. This feature ultimately obscures the $2q^*$ and $3q^*$ peaks of the neat polymer at high QD concentrations. Using equation 5.1, the spacing associated with this peak at q = 0.14 Å^{-1} is 4.5 nm and is attributed to the distance between aggregated QDs. From TEM and

SAXS measurements, the QDs are observed to be roughly ~3.5 nm in diameter. Thus, the spacing apparent in the composite SAXS data suggests there is approximately 1 nm spacing between QDs. This spacing is consistent with ligands on the surface of the QDs being interwoven; the longest ligands have a length on the order of 1 nm. The cartoon schematic in Figure 5.4 demonstrates how this might look.

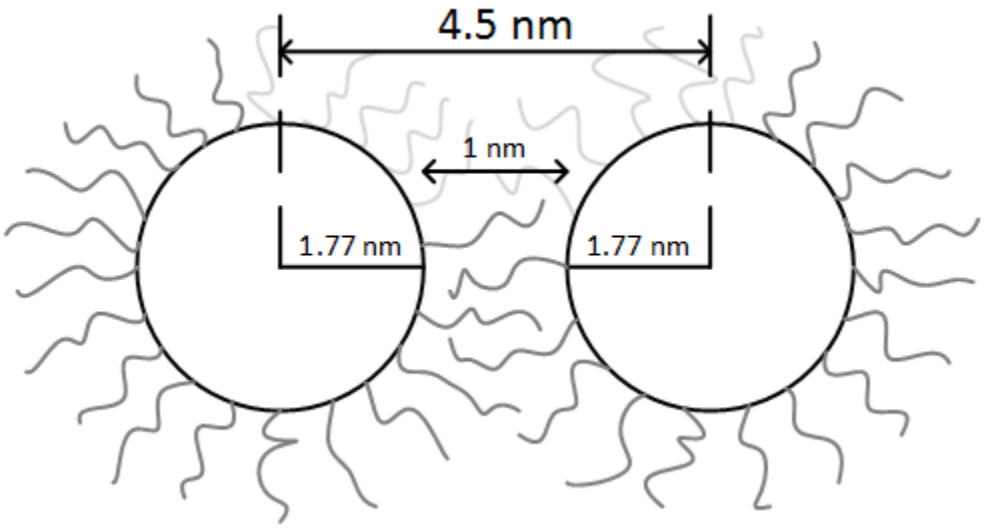

Figure 5.4: Cartoon depiction of aggregated QDs. The QD diameter is 3.5 nm, as measured by TEM and SAXS. Ligands on the surface of the QDs are on the order of 1 nm in length.

The polymer lamellae spacing appears unaffected by the quantum dots; the peaks do not shift upon QD addition. However, several additional small peaks appear at larger q past q = 0.14 $Å^{-1}$ and become increasingly prominent with higher QD concentrations, and thus are attributed to the potential ordering of QDs. These peaks occur at values close to body centered cubic (BCC) or simple cubic (SC) packing ratios of q/q^* but do not exhibit all expected ratios, which suggests that the QD aggregates are largely disordered. Table 5.2 demonstrates the expected values for BCC, SC, and face centered cubic (FCC).

q/q^*	Position, q [$Å^{-1}$]	Expected value for q^* = 0.141	Error	SC	BCC	FCC
1	0.141	0.141	--	X	X	X
√2	0.202	0.199	1.5%	X	X	--
√3	0.236	0.244	3.3%	X	X	X
2	0.285	0.282	1.1%	X	X	X
√5	--	0.315	--	X	X	--
√6	0.352	0.345	2%	X	X	--

Table 5.2: Recorded peak values and their relation to expected values given various q/q^* ratios. Expected q/q* values for simple cubic (SC), body-centered cubic (BCC), and face-centered cubic (FCC) are indicated by 'X' in the columns.

The TEM results shown in Figure 5.3 are consistent with the results observed in SAXS. The QDs are present in aggregated chunks in the polymer film. There are small sections of QDs exhibiting local order but the QDs appear to be largely disordered from the TEM images, which is consistent with the observation from SAXS. This result is unsurprising: there is little enthalpic drive for the QDs to prefer one polymer component over the other based on the ligands on the QD surface and their similarity in chemical nature to both polymer components. The majority of ligands on the surface of the QDs are trioctylphosphine and trioctylphosphine oxide, which are comprised of linear alkane chains bound to a phosphorous. The linear alkane chains are thus very similar to short PE chains. PE has a solubility parameter of 7.9 $(cal/cm^3)^{1/2}$, compared to PCHE with a solubility parameter of roughly 8.3 $(cal/cm^3)^{1/2}$.[114,140] Thus, there is insufficient enthalpic gain for the QDs to disperse in either polymer block selectively or prefer dispersion in the

polymer over proximity to other QDs. The close proximity of the QDs suggested by the SAXS data (roughly 1 nm between QDs) could also be a result of partial ligand loss from the QD surface. QDs dropcast from solution typically exhibit an average of 2 nm between QD edges when close packed. Ligand loss is a common cause of aggregated QDs; it is possible that some ligand loss occurs during the composite processing at elevated temperatures ($T \geq 140°C$).[2]

The polymer matrix chains are much longer than the ligands on the nanoparticle surface. From Chapter Four, $N_{ligand} = 4$, whereas $N_{polymer} = 230$.[177] Thus, $N_{polymer}/N_{ligand} = 57.5$, firmly in the territory of dry brush conditions and nanoparticle aggregation for relatively high ligand density on the QD surface (1.6 nm^{-2}, if no ligand loss is assumed) observed for nanoparticle-homopolymer composites where $\chi \approx 0$.[117,119,146,147,141] Given the small χ of this PE-*b*-PCHE polymer, the results of the simpler homopolymer composites may demonstrate similarities. Based on the QD aggregation apparent in the TEM images and SAXS data, the polymer matrix chains do not wet the QD ligands, as would be the case for wet brush conditions. The loss in polymer matrix chain conformational entropy is minimized via QD aggregation, at the cost of QD translational entropy (dispersion in the polymer matrix).

The next section employs a polymer with more drastic chemical difference in block components and revisits a similar freeze-drying and temperature processing strategy in comparison with a direct deposition method to form QD-polymer composites.

Section 5.2 – CdSe in Poly(styrene)-*b*-Poly(butadiene)

This section details experiments in which CdSe QDs were prepared in a polymer matrix via two methods: freeze drying followed by heating to form a bulk structure, and drying a film from solvent. The composite structures are shown to be different based on the method of preparation. Poly(butadiene) (PB) was previously demonstrated to be a good polymer for dispersing CdSe QDs with native ligands in Chapter Four.

5.2.1 Neat Polymer Characteristics

The poly(styrene)-*b*-poly(1,4-butadiene) (PS-*b*-PB) block copolymer used in these studies was synthesized by Ronald Lewis. Pertinent polymer characteristics are given in Table 5.3.

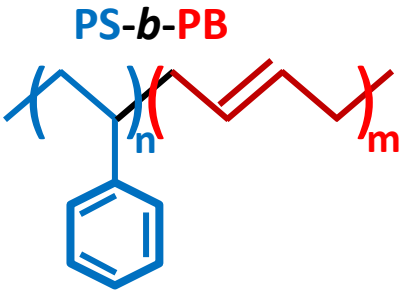	**M_n**	**f_{PB}**	**T_{ODT}**	**PB block Microstructure**
	22.1 kg/mol	**0.198**	**150°C**	**10% 1,2-PB 90% 1,4-PB**

Table 5.3: PS-*b*-PB characteristics; all were measured by Ronald Lewis. The PB microstructure and f (using published densities[178]) were determined via proton NMR, and Mn was determined by proton NMR end group analysis. T_{ODT} was determined from rheology on heating (1 °/sec).

TEM micrographs of neat PS-*b*-PB cryo-microtomed from a bulk composite annealed at 130°C for 8 hr are given in Figure 5.5. The sample was stained with OsO_4, which penetrates the PB component of the block copolymer.[179] The polymer forms PB spheres in a body-centered cubic lattice with a unit cell parameter of 13.1 nm.

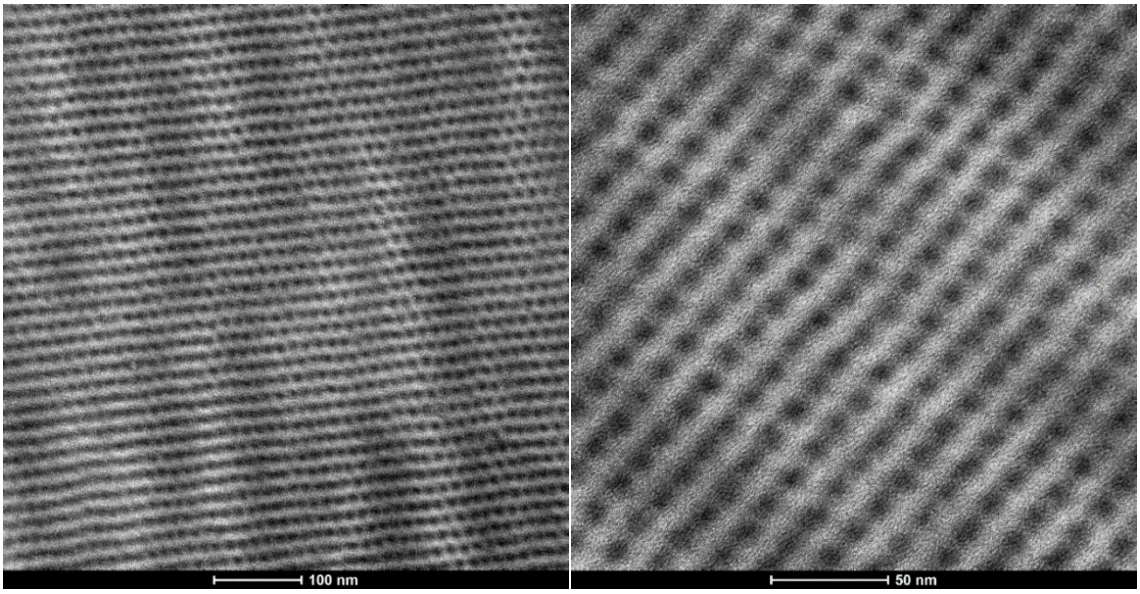

Figure 5.5: Micrographs of PS-*b*-PB block copolymer cryo-microtomed from a bulk composite that was annealed at 130°C for 8 hr. The samples were stained with OsO_4. These samples were prepared and micrographs taken by Dr. Bongjoon Lee.

5.2.2 Composite Preparation

Composites of CdSe QDs and PS-*b*-PB were prepared in two ways: films dropcast from solution, and bulk structures prepared from freeze-drying. In the preparation of freeze dried samples, 20 mg of dry polymer was dispersed in ~5 mL of benzene and added to 5.88 nmol of dried QDs (2.3 nm in radius). The resulting mixture appeared colored and clear, indicative of good mixing. The dispersion was immersed in liquid nitrogen to freeze dry the sample. Immediately following this step, the sample was moved into an oven and held under vacuum at room temperature overnight to sublime the benzene. The next day, the vacuum oven was heated to 140°C and held at this temperature for 1.5 hours. Afterward, the oven slowly cooled to room temperature over the course of 3-5 hours. The resulting composite was colored, slightly sticky, and granulated. A small piece of this composite was encapsulated in epoxy and cryo-microtomed by Dr. Bongjoon Lee for TEM.

In the preparation of dropcast films, a quantity of dry polymer (2-10 mg) was dispersed in benzene (200 uL – 1 mL) and then added to dried QDs (0.5-10 nmol, 2.3 nm in radius). The dried QDs were prepared from a measured volume of CdSe QDs dried from hexane, where the volume dried was chosen based on the concentration of QDs as determined by their absorbance. The QDs readily disperse in benzene; the resulting mixture of PS-*b*-PB and CdSe QDs in benzene was colored and transparent. One to 2 uL of the QD-polymer dispersion was dropcast onto carbon coated copper TEM grids and allowed to dry in air.

5.2.3 Results

Micrographs of CdSe QDs in PS-*b*-PB prepared through freeze-drying were taken by Dr. Bongjoon Lee before and after staining with osmium tetroxide, OsO_4, and are shown before staining in Figure 5.6 and after staining in Figure 5.7.

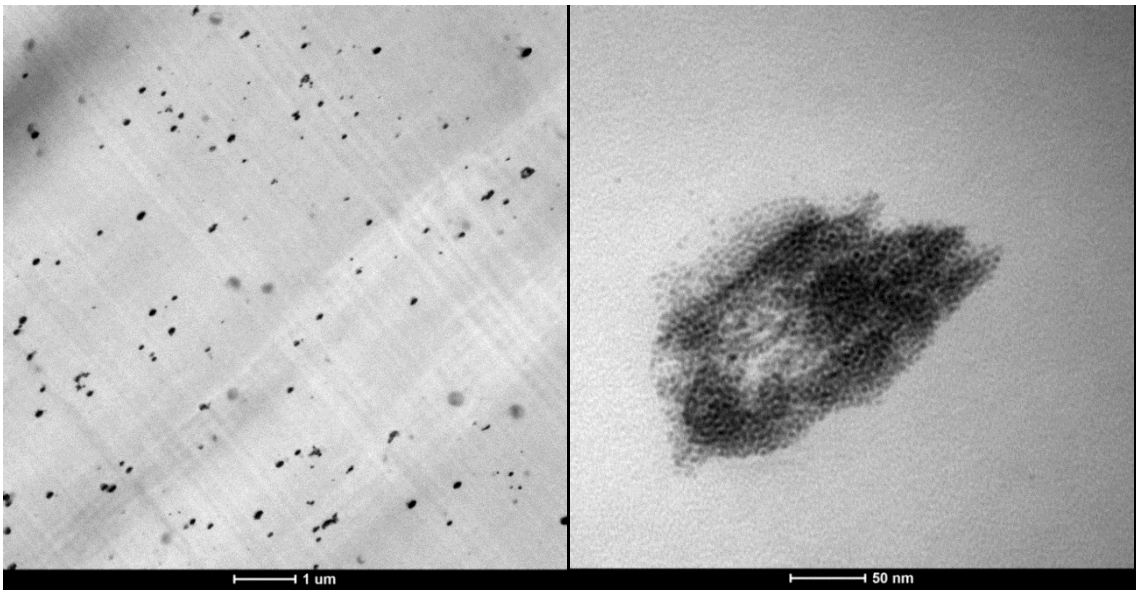

Figure 5.6: Micrographs of cryo-microtomed sections of CdSe QDs in PS-*b*-PB prepared from freeze-drying a dispersion. These micrographs were taken by Dr. Bongjoon Lee.

The resulting composite of CdSe QDs in PS-*b*-PB prepared through freeze-drying was 6 wt% (1.5 vol%) CdSe QDs in polymer. The QDs appear largely aggregated in small clumps throughout the polymer film. After staining, the sphere-forming morphology of PS-*b*-PB is evident in the micrographs; OsO_4 stains PB (Figure 5.7).

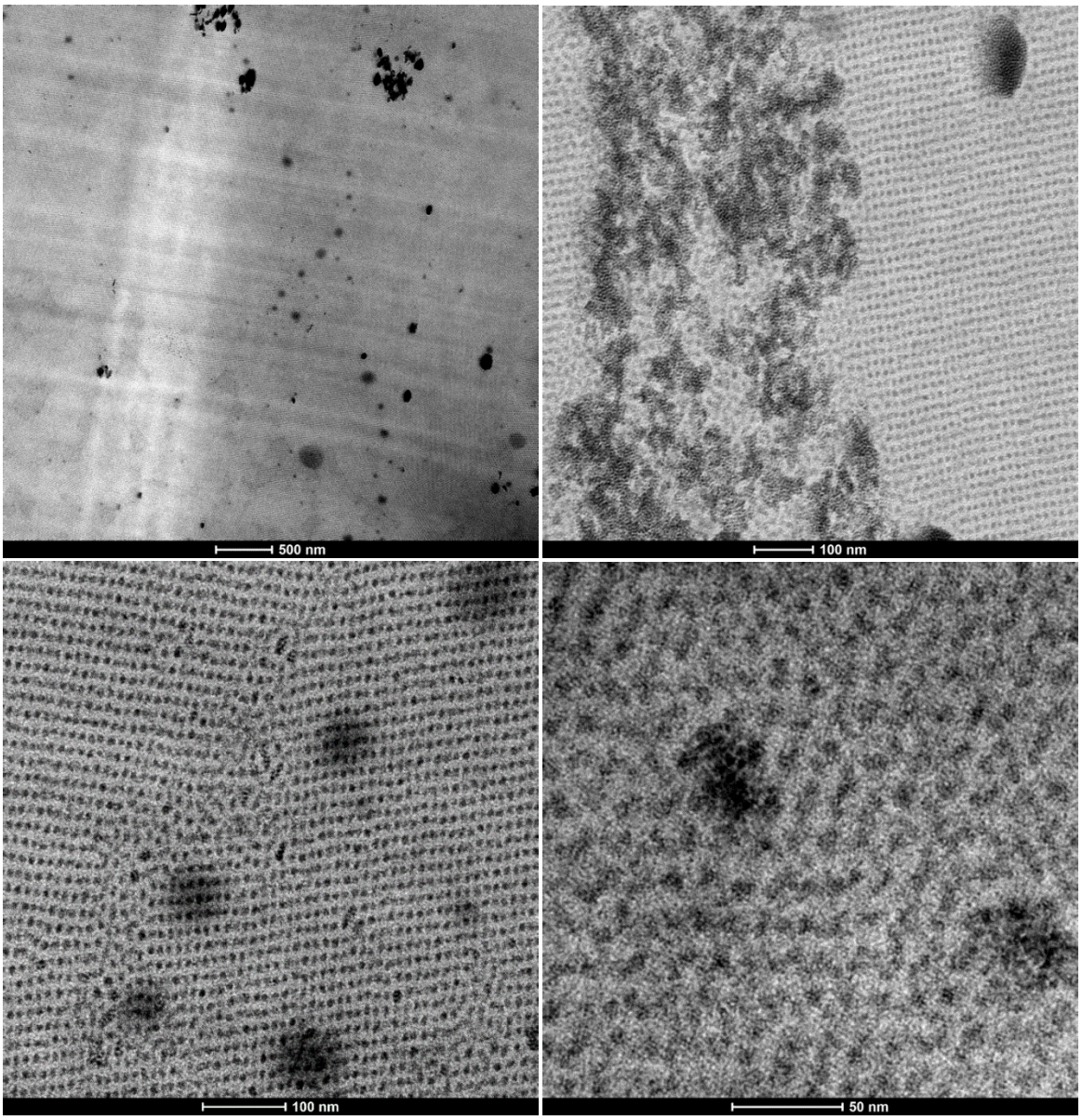

Figure 5.7: Micrographs of microtomed sections of CdSe QDs (6 wt% or 1.5 vol%) in PS-*b*-PB after staining with OsO_4. These micrographs were taken by Dr. Bongjoon Lee.

For comparison, micrographs of 6 wt% (1.5 vol%) CdSe QDs in PS-*b*-PB films dropcast from benzene were taken and are shown in Figure 5.8. The center-to-center spacing between the QDs was approximately 6.6 nm across most of the micrographs. However, in some small sections, like the one circled in red, the spacing increased to 7.7 nm.

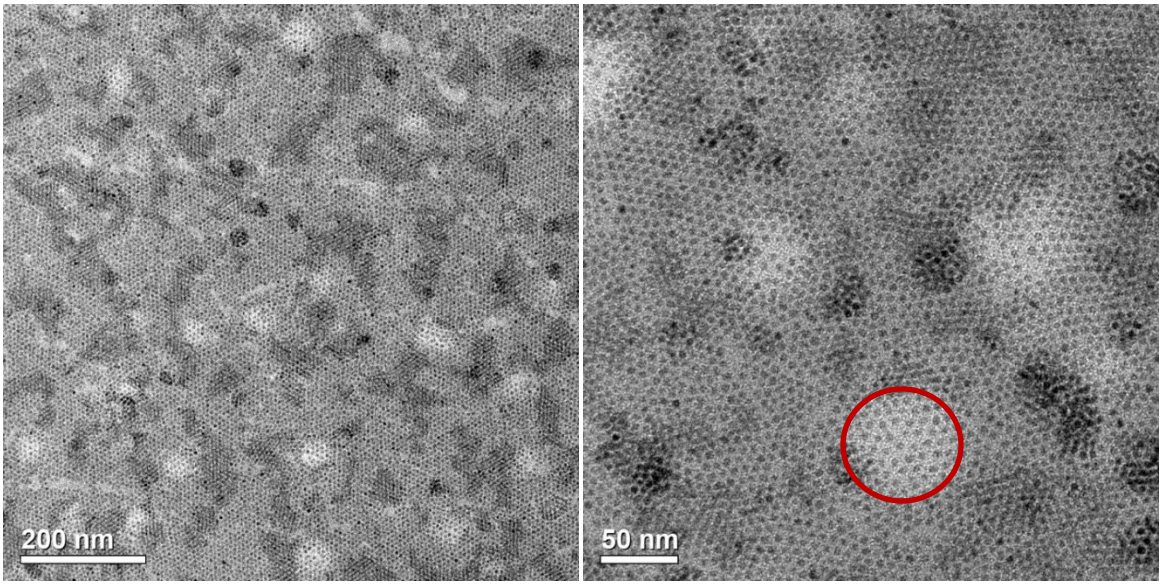

Figure 5.8: Micrographs of CdSe QDs (6 wt% or 1.5 vol%) in PS-*b*-PB of films dropcast from benzene.

5.2.4 Discussion of Composite Structures

From the micrographs of freeze-dried CdSe QDs in PS-*b*-PB, it is apparent that the QDs are mostly aggregated in clusters ranging from < 50 nm to ~500 nm in size (aggregate edge length or diameter). Often, a small number (<20) of stray QDs are visible near, but separated from, the dense QD aggregates, and are ostensibly dispersed in the polymer. However, it is difficult to say if any of the lone QDs prefer the PB domain (sphere-forming) over the PS. In some of the higher magnification stained images, a small fraction (<1 in 100) of the PB spheres appear to contain one or more QDs. Upon examining the unstained images, however, the vast majority of QDs are contained in the

aggregates and not dispersed in the polymer. This QD aggregation does not appear to prevent PS-*b*-PB sphere formation, as the polymer sphere forming phases are visible after staining. Interestingly, the grain boundaries of the polymer sphere forming morphology do not appear to be drastically affected by the presence of the QDs. This is evident in the top right frame of Figure 5.7, where a large QD aggregate only disrupts local morphology, but does not affect the larger grain evident on either side of the aggregate. Additionally, the polymer still exhibits sphere forming morphology in the small spaces (10-100 nm) between QD aggregates.

In the films prepared from dropcasting QDs and PS-*b*-PB from benzene, the QDs prefer to form separate layers of QDs either above, below, or sandwiched between layers of the polymer matrix. The center-to-center spacing between QDs in the majority of the films (6.6 nm) indicates packing consistent with close-packed QDs based on TEM data of neat QDs dropcast from hexane (6.8 ± 0.4 nm). However, there are small sections such as the one circled in red in Figure 5.8 where the QD spacing grows larger. In this example, the center-to-center spacing between QDs has increased to 7.7 nm. The increase in spacing (1.1 nm) is small compared to the spacing between polymer spheres (11.3 nm, as calculated from a lattice parameter of a = 13.1 nm). One possibility is that the polymer film formed a raised surface or bubble in that area while drying and the QDs formed a film that stretched across the raised surface. QD localization at the free surface or substrate interface may reduce the surface energy of the thin film, as has been demonstrated in the case of nanoparticles in thin film homopolymer and diblock copolymer composites.[117,180]

Ultimately, there is a clear difference between QD-polymer composites formed through freeze-drying and subsequent temperature processing and those prepared via dropcasting. At some point during the process of freeze-drying or subsequent heating, the QDs irreversibly aggregate in the polymer composites. The lack of these dense aggregates in the dropcast films suggests that the drying process enables phase separation of the QDs from the polymer but does not lead to the same aggregation seen in freeze-dried samples. However, the opportunity to better mix QDs in the polymer composite may be attainable with the right solvent processing via the dropcasting method. The next section in this chapter addresses one route towards using solvent processing to achieve better mixing of polymer and QDs in composites prepared via dropcasting.

Section 5.3 – CdSe in Poly(lactic acid)-*b*-Poly(1,4-butadiene)

In this section an alternative route towards QD organization in block copolymers is considered utilizing the inversion of polymer micelles. In certain solvents, or a mixture of solvents, we expect the poly(lactic acid)-*b*-poly(butadiene) (PLA-*b*-PB) block copolymer to form micelles, given the considerable differences in chemical composition between the two blocks ($\chi \approx 0.64$ at room temperature, given $\hat{V}_{ref}$ calculated from published densities[178,181]) Recall from Chapter One that the interaction parameter between two components, χ_{AB}, can be estimated by

$$\chi_{AB} = \frac{\hat{V}_{ref}}{RT}(\delta_A - \delta_B)^2 \tag{5.2}$$

where $\hat{V}_{ref}$ is the molar reference volume, T is the temperature, and δ_A and δ_B are the Hildebrand solubility parameters of components A and B. In the event that χ_{AB} is < 0.3, an empirical modification to the formula is more accurate[114]:

$$\chi_{AB} = 0.34 + \frac{\hat{V}_{ref}}{RT}(\delta_A - \delta_B)^2 \tag{5.3}$$

The Hildebrand solubility parameters give insight into the interactions between the polymer block components and various solvents. The Hildebrand solubility parameter for PLA (δ = 9.9 $(cal/cm^3)^{1/2}$) is large in comparison to that for PB (δ = 8.3 $(cal/cm^3)^{1/2}$); thus, good solvents that are thermodynamically driven to mix with and swell one polymer component (χ < 0.5 between the polymer component and the solvent) may not be good solvents for the remaining polymer component. Consider the example of n-hexane (δ = 7.3 $(cal/cm^3)^{1/2}$): whereas PB mixes with this solvent ($\chi \approx 0.56$), PLA faces strong penalties for mixing ($\chi \approx 1.5$). As χ increases, the interactions between solvent and polymer become increasingly unfavorable for mixing. When χ = 0.5 (theta solvent), the unfavorable solvent-polymer segment interactions are balanced out by the self-avoiding nature of the polymer coil (*i.e.* self-avoiding walk) such that the polymer does not swell in the solvent and adopts a random walk behavior. Thus, when a diblock copolymer is a solvent environment where one polymer block is driven to mix with the solvent ($\chi \leq 0.5$), whereas the other polymer block is not, the diblock copolymer may self-assemble into polymer micelles to shield unfavorable interactions between the solvent and the latter polymer block.[182-185] The micellar structure balances entropic loss of polymer chains that adopt the micellar structure with enthalpic gains of minimizing the interaction between the solvent and the polymer block component with a large χ.[186] In practice, this PLA-*b*-PB may form micelles in solvents similar to hexane, where there is a large driving force

($\chi \approx 1.5$) for the PLA component to minimize interaction with the solvent. The resulting micellar structure would be composed of PB corona protecting a PLA micellar core.

When the inverted micelles (minority block on the outside) are dried from a solvent, the polymer rearranges to fill space. In the bulk phase, χN is large enough ($\chi N \approx 65$) that the polymer is enthalpically driven to order in a way that minimizes the interactions between the PB and PLA blocks. When the polymer dries from the inverted micelles, at some point the micelles must either break apart or invert to form a bulk structure. Can this drying process be used to capture the QDs inside the polymer minority component block? While many processes have been modeled or tested for incorporating QDs into polymer micelles,[187-194] the inversion of micelles to capture QDs during the drying process is a novel pathway. A cartoon mock-up of the intended micelle inversion process is given in Figure 5.9.

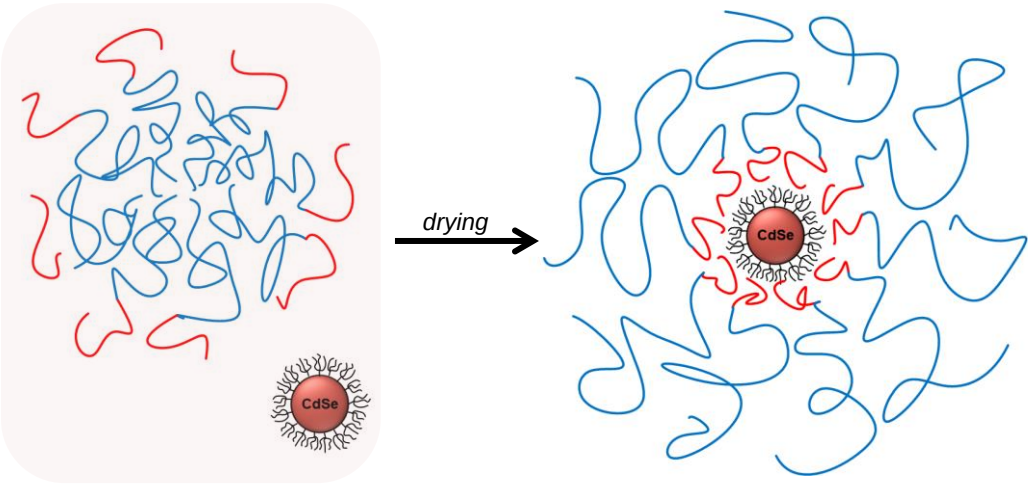

Figure 5.9: Cartoon schematic of QDs and inverted PLA-*b*-PB micelles dispersed in a nonpolar solvent. Upon drying, the micelles have a chance to capture the QDs in the PB component (favorable enthalpic interactions).

5.3.1 Neat Polymer Characteristics

The poly(D,L lactide)-b-poly(1,4-butadiene) (PLA-*b*-PB) used in this study was synthesized by Ronald Lewis via anionic polymerization followed by ring-opening polymerization.[195,144] Dispersity is believed to be < 1.1 given the synthesis methods. The characteristics are given in Table 5.4. The volume fraction of PB is 0.159, which suggests this polymer should form a BCC phase.

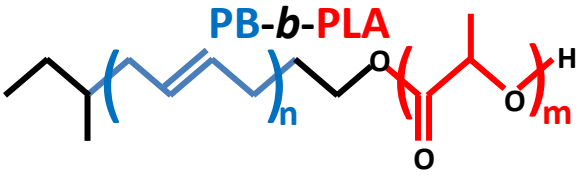	**M_n**	***f_{PB}***	**T_{ODT}**	**PB Block Microstructure**
	8900 g/mol	**0.159**	**125°C**	**12% 1,2-PB 86% 1,4-PB**

Table 5.4: Characteristics of PLA-*b*-PB polymer. All measurements were made by Ronald Lewis. PB microstructure and *f* (using published densities[178.195]) were determined via proton NMR, M_n was determined via proton NMR by end group analysis. T_{ODT} was determined from rheology on heating (1 °/sec).

SAXS data of this polymer shown in Figure 5.10 shows peaks at $\sqrt{2}q^*$, $\sqrt{3}q^*$, and $2q^*$, which is consistent with body centered cubic or simple cubic ordering. From Equation 5.1, the corresponding unit cell length is 12 nm given $q^* = 0.052$ Å^{-1}.

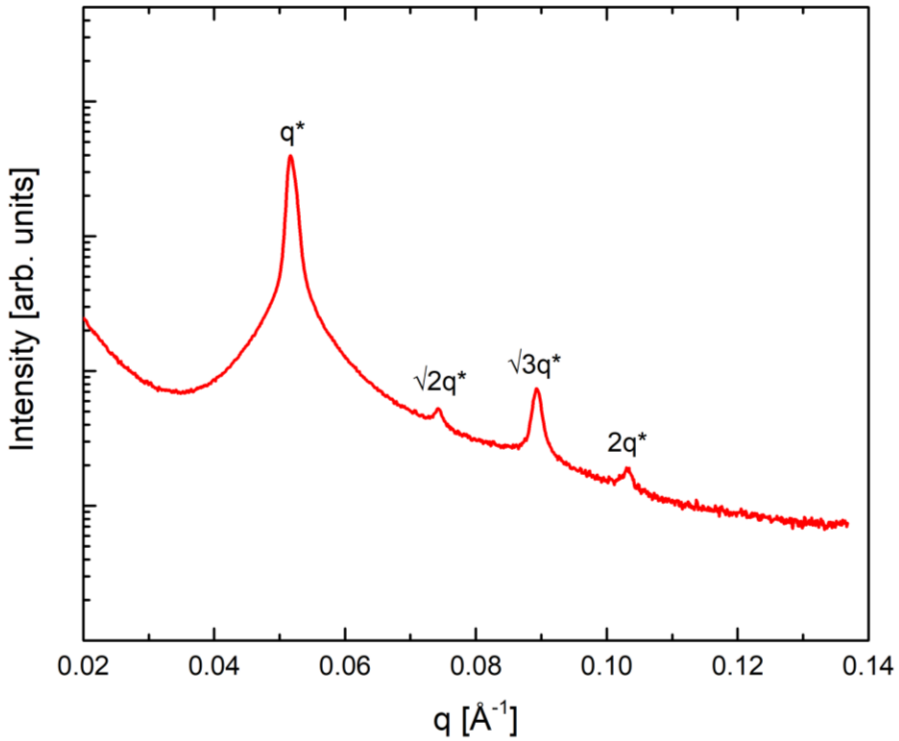

Figure 5.10: SAXS data of PLA-*b*-PB taken after 5 minutes at 85°C. The source wavelength is 0.7293 Å.

5.3.2 Micellization

Polymer micelles are formed when the solvent environment is unfavorable for one block of the block copolymer at polymer concentrations exceeding the critical micelle concentration (CMC). When the polymer is more dilute than the CMC, the polymer is observed only as single chains in solution. Above the CMC, when one block is driven thermodynamically to mix with the solvent but the other block is not, the polymer chains arrange to minimize interactions between the solvent and the block that does not disperse in the solvent.[186,196]

This PLA-*b*-PB polymer can be readily dispersed in solvents like chloroform (δ = 9.3 (cal/cm^3)$^{1/2}$) and tetrahydrofuran (δ = 9.1 (cal/cm^3)$^{1/2}$).[114] These solvents fall between nonpolar solvents (like hexane, δ = 7.3 (cal/cm^3)$^{1/2}$) and more polar solvents (like ethanol,

$\delta = 12.7$ $(cal/cm^3)^{1/2}$). Whereas PB is hydrophobic and nonpolar ($\delta = 8.3$ $(cal/cm^3)^{1/2}$), PLA is more polar in nature ($\delta = 9.9$ $(cal/cm^3)^{1/2}$). To induce polymer micellization, a careful balance of polar and nonpolar solvents is required. To form micelles with the minority block PB on the outside, the solvent must be chosen to be nonpolar enough to disperse PB and have unfavorable enthalpic interactions with PLA, but not so nonpolar as to lead to polymer phase separation. This balance was achieved by using a mixture of chloroform (a fairly good solvent for both blocks) and hexane (only a good solvent for PB).

Samples of PLA-*b*-PB were prepared for DLS by dispersing a weighed quantity of polymer in a mixture of chloroform and hexane and passing the dispersion through a 0.35 μM PTFE filter. DLS results shown in Figure 5.11 reveal the transformation from free polymer chains in solution to polymer micelles upon increasing the proportion of hexane; this change is evident in the shift of hydrodynamic radius from roughly 3.7 nm to 10-20 nm. This changeover occurs at roughly 31-33% chloroform and 67-69% hexane mixtures; at solvent mixtures of higher chloroform percentages, the polymer is still freely dispersed in solution as single chains. When the percentage of hexane exceeds roughly 70%, the hydrodynamic radius jumps up to >100 nm and as the percentage of hexane increases, the mixture turns cloudy, indicating phase separation.

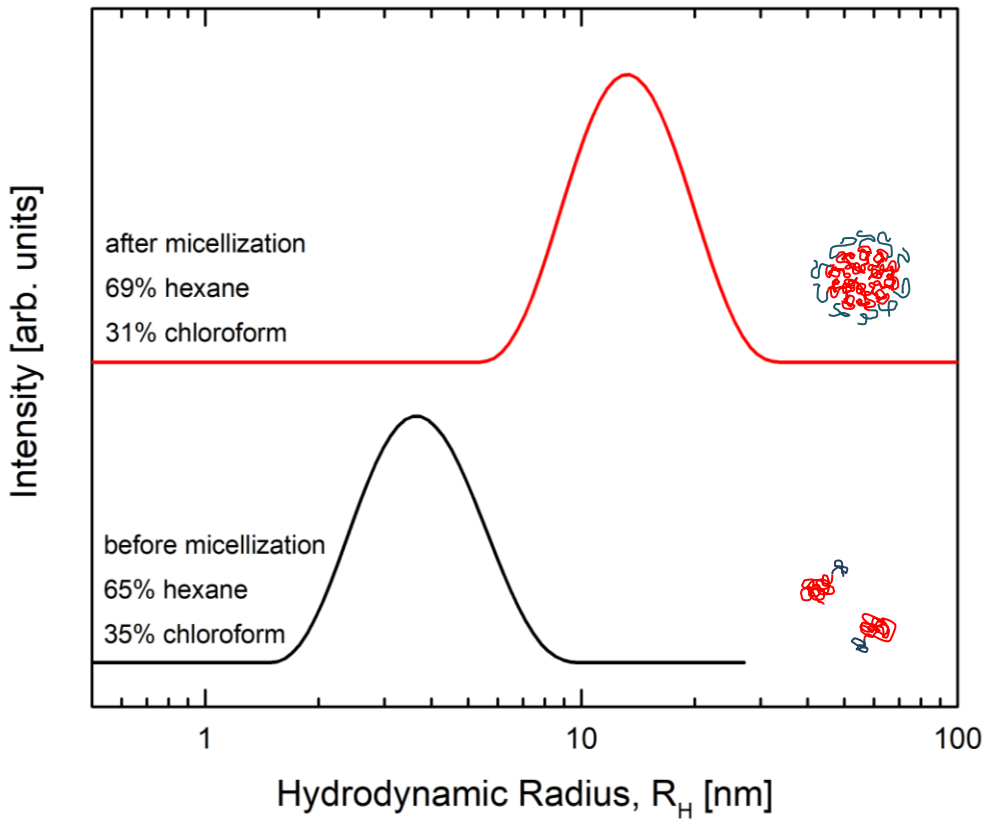

Figure 5.11: Hydrodynamic radius data of PLA-*b*-PB taken before (bottom curve) and after (top curve) micellization. Before micellization, the polymer is dispersed as free chains in a mixture of 65% hexane, 35% chloroform. Upon addition of hexane to 69% hexane and 31% chloroform, polymer micelles form.

In the event the samples in tubes (covered with parafilm) were allowed to sit for days at a time, solvent evaporation was noticeable. The polymer-solvent mixtures occasionally turned cloudy over time; this was attributed to the ratio of chloroform and hexane being disturbed in the evaporation process, leading to >70% hexane solvent. The vapor pressure of neat hexane at room temperature is 151 mmHg, whereas the vapor pressure of neat chloroform at room temperature is 197 mmHg (both estimated using Antoine's Equation). Thus, the observation of polymer phase separation is consistent with the loss of slightly higher vapor pressure chloroform; if the starting ratio of hexane: chloroform is high, the subsequent faster evaporation of chloroform leads to hexane:

chloroform ratios high enough to phase separate the polymer. The samples that grew cloudy over time were also similar in appearance to polymer-solvent mixtures prepared at >70% hexane.

5.3.2b Incorporating Quantum Dots

Addition of the CdSe QDs to the polymer dispersion was tested at two different time points: after polymer micellization, and before. These processes are depicted in Figure 5.12 (QDs added after micellization) and Figure 5.13 (QDs added before micellization). Polymer samples were prepared by mixing 2-20 mg of PLA-*b*-PB with 100 uL to 1 mL of chloroform and then 100 uL to 1 mL of hexane. The exact quantity of polymer and ratio of two solvents was varied across experiments; in general, roughly 10 mg of polymer was used and the starting chloroform/hexane ratio was 40/60. Note that the polymer does not disperse in neat hexane, so chloroform was added first. This polymer in solvent was filtered twice through 0.35 μM PTFE filters into a small tube and sealed with parafilm. The sample was then evaluated using DLS within the next 1-18 hours. At this stage, the DLS indicated a single size population at $R_H \approx 4$ nm.

When the objective was to add QDs after polymer micellization, the polymer solution was moved to a vial, a small (10-30 μL) volume of filtered hexane was added, and the vial was agitated to ensure mixing. The resulting mixture was added again to the DLS tube and new DLS was taken. This process was repeated until the DLS indicated a size population at $R_H \approx$ 10-20 nm. At that point, the mixture was poured into a vial containing a known quantity (0.5-10 nmol) of dried QDs. The vial was agitated to ensure mixing and then filtered again through a 0.35 μM PTFE filter. The sample was observed using DLS. This process is depicted in Figure 5.12.

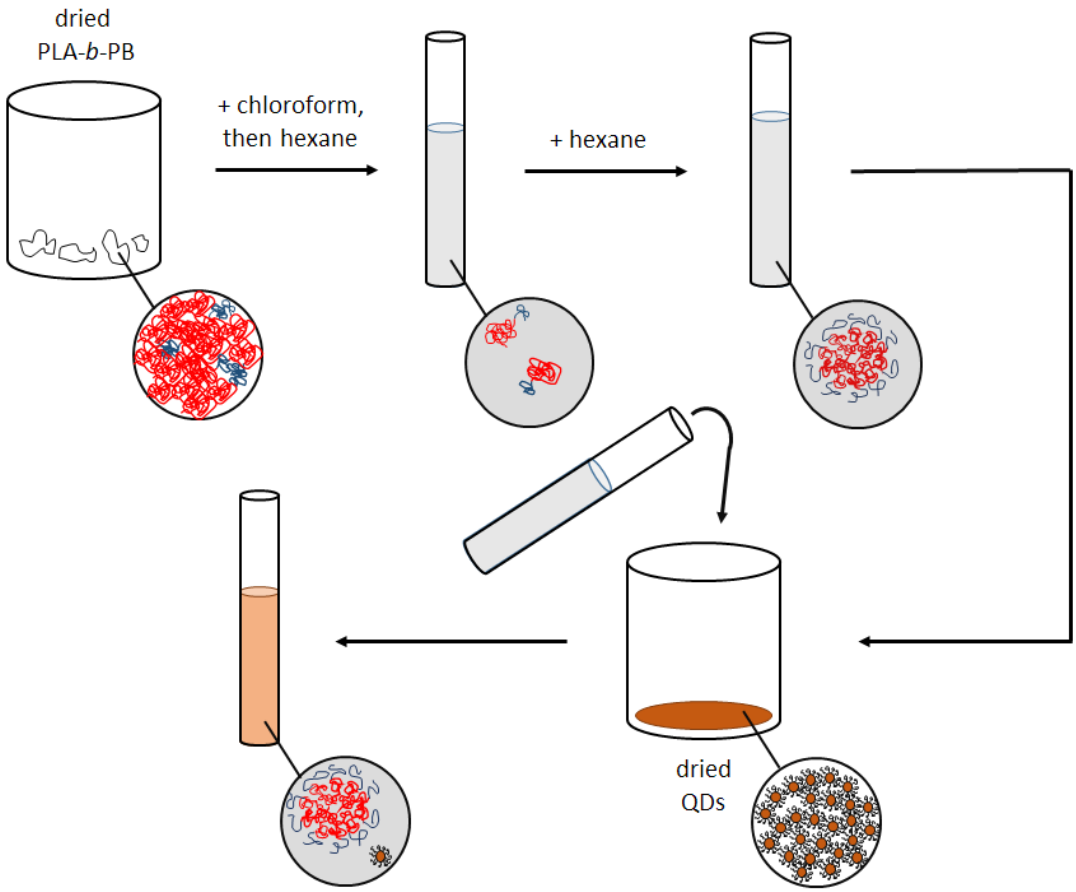

Figure 5.12: Cartoon schematic of the preparation of CdSe QDs with preformed PLA-*b*-PB micelles in a mixture of chloroform and hexane.

When the objective was to add QDs before polymer micellization, the original polymer solution ($R_H \approx 4$ nm) was added to a vial containing a known quantity (0.5-10 nmol) of dried QDs and agitated to mix. The resulting mixture was filtered through a 0.35 μM PTFE filter and DLS was repeated. The dispersion was transferred to a clean vial and 10-30 μL of filtered hexane was added. The dispersion was agitated and then transferred back to the tube for DLS. This hexane addition process was repeated until a size population of $R_H \approx$ 10-20 nm was observed. Figure 5.13 shows a cartoon schematic detailing this process.

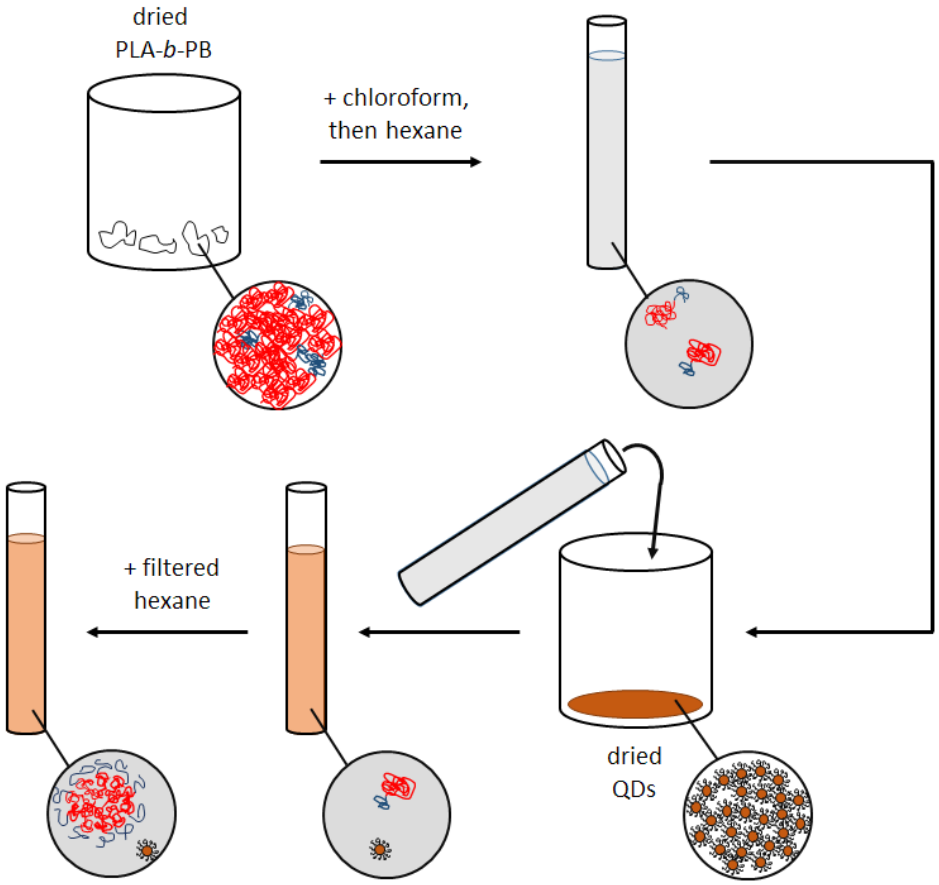

Figure 5.13: Cartoon schematic of adding CdSe QDs to a dispersion of PLA-*b*-PB in chloroform and hexane. PLA-*b*-PB micelles are then formed by subsequent addition of hexane.

Samples prepared with QDs added before and after polymer micellization were studied using dynamic light scattering and are shown in Figure 5.14. All dispersions appeared colored and clear to the eye regardless if the QDs were added before or after polymer micellization.

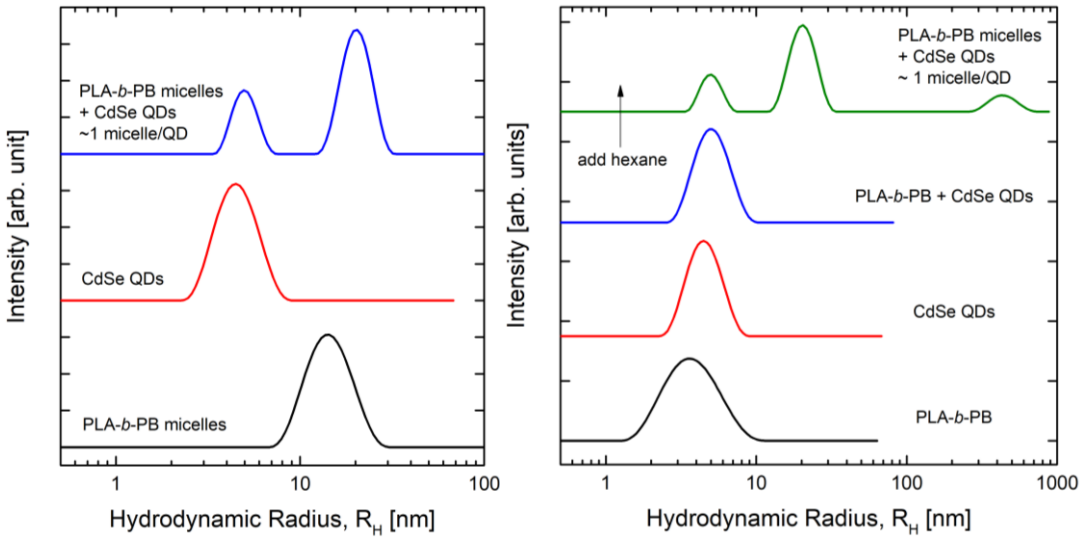

Figure 5.14: Hydrodynamic radii of CdSe QDs added after (left) and before (right) micellization of PLA-*b*-PB in chloroform-hexane mixtures . The mixtures containing polymer are roughly 1 wt% PLA-*b*-PB in solvent; mixtures containing QDs are roughly 0.3 wt% QDs in solvent. In the mixtures containing both polymer and QDs, there is roughly 1 QD for every polymer micelle.

5.3.3 Film Composite Preparation

Films of CdSe QDs in PLA-*b*-PB were dropcast from mixtures similar to those prepared for micellization studies. Typical dispersions were prepared with 2-15 mg of PLA-*b*-PB and 0.3-10 nmol of CdSe QDs in 500 uL to 4 mL of hexane/chloroform mixture. One to 2 μL of these solutions were dropcast onto carbon coated copper TEM grids to form thin films. The resulting films ranged from <0.5 vol% to 12 vol% CdSe QDs. When larger volumes of these mixtures were dropcast onto clean glass slides, the resulting film was colored and translucent.

5.3.4 Film Composite Results

TEM was performed on a variety of samples as described above. Figure 5.15 shows the results of films prepared from dispersions where the QDs were added before and after polymer micellization in chloroform and hexane.

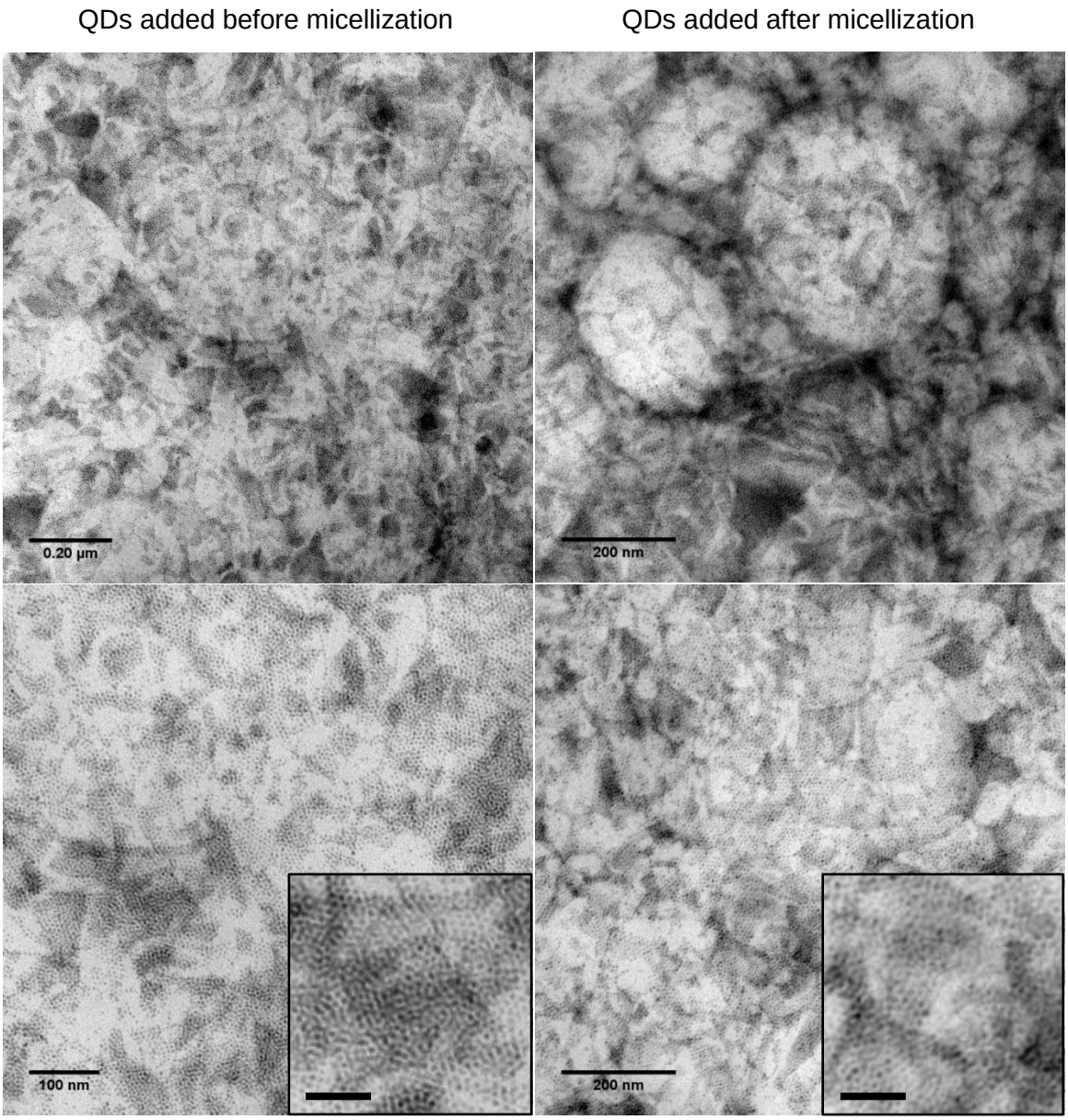

Figure 5.15: Micrographs of CdSe QDs added to PLA-*b*-PB in a chloroform and hexane mixture before (left column) and after (right column) polymer micellization. Inset image scale bars are 50 nm. Films were prepared by dropcasting.

A series of TEM micrographs of CdSe QDs and PLA-*b*-PB dropcast from differing ratios of chloroform: hexane is shown in Figure 5.16. Ratios of 0% hexane and 100% chloroform to 70% hexane and 30% chloroform were tested. Higher proportions of hexane (exceeding 70%) led to cloudy solutions indicative of polymer phase separation.

All samples shown in Figure 5.16 constitute 1 vol% CdSe in polymer. The 50% hexane and 50% chloroform case appears to the eye to be less concentrated than the other samples; this is attributed to a small section of the TEM grid containing a large mountain of QDs that appear to have phase separated. The majority of the film is represented by the images shown in Figure 5.16.

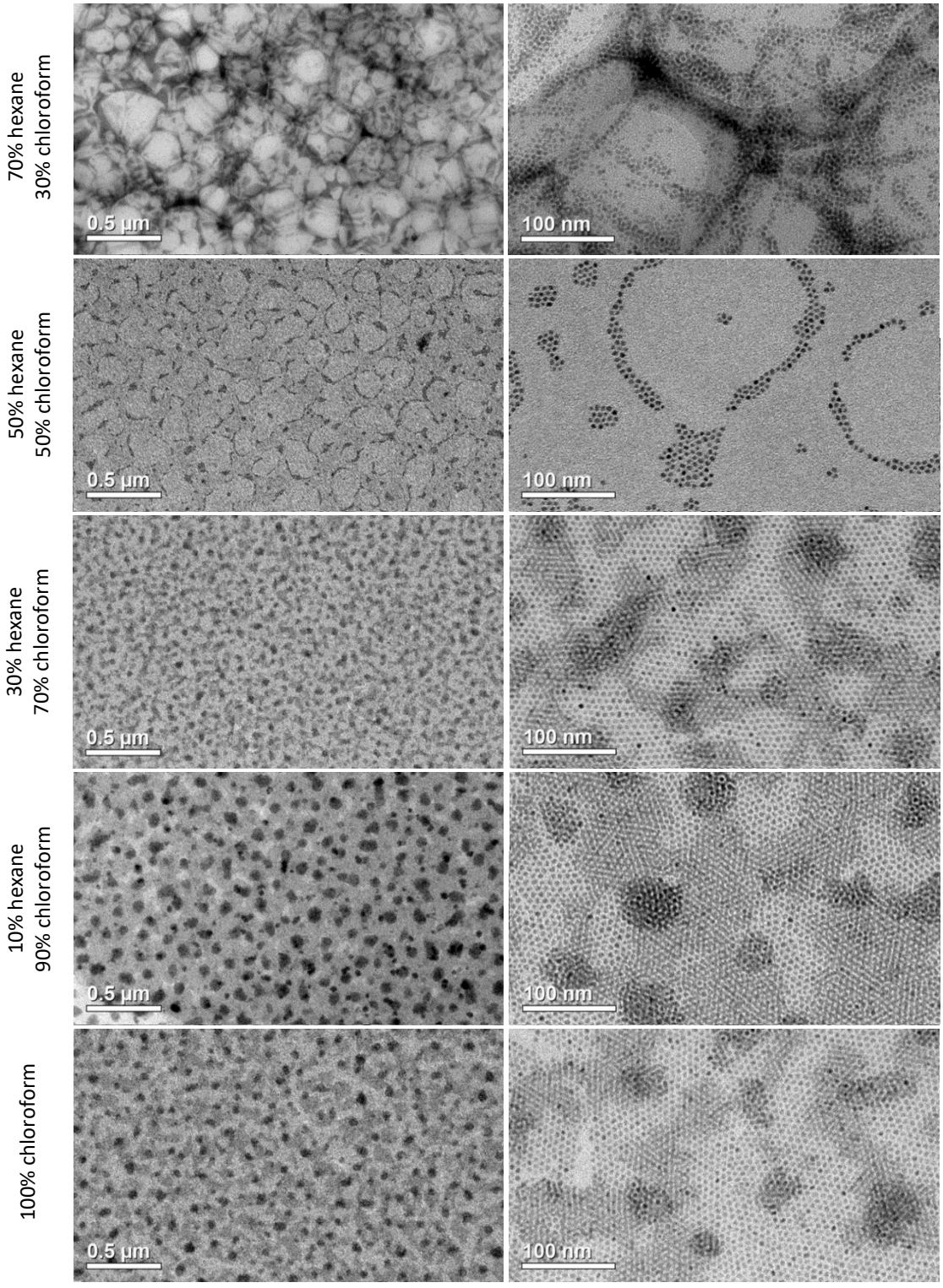

Figure 5.16: Micrographs of 1 vol% CdSe in PLA-*b*-PB composites prepared by dropcasting from mixtures of 70%-30%, 50%-50%, 30%-70%, 10%-90%, and 0%-100% hexane-chloroform, respectively, from top to bottom. On the left is a broad view of dropcasted film structure and on the right are higher magnification images.

Fourier transforms of TEM images reveal periodic structure information which can be used to identify repeating features prominent in the micrograph. The resulting fast Fourier transform (FFT) image can be radially averaged to determine the average center-to-center spacing between QDs. Table 5.5 includes data taken from multiple images of samples prepared from different ratios of chloroform: hexane.

% Hexane	% Chloroform	Average Spacing between QDs
70	30	6.2 ± 0.2 nm
50	50	6.6 ± 0.2 nm
30	70	6.4 ± 0.1 nm
10	90	6.9 ± 0.1 nm
0	100	6.5 ± 0.1 nm

Table 5.5: Average center-to-center spacing between CdSe QDs in PLA-*b*-PB composites prepared from different ratios of hexane-chloroform mixtures. Average spacing between these CdSe QDs prepared from hexane is 6.8 ± 0.4 nm.

In addition, the effect of CdSe QD concentration was tested. Figure 5.17 shows samples ranging from 0.08 vol% CdSe in polymer to 12 vol% CdSe in polymer dropcast from 70% hexane and 30% chloroform, and 0% hexane and 100% chloroform. The 12 vol% CdSe case was chosen as this concentration allows for ~1 QD per expected polymer sphere based on the lattice spacing calculated from neat PLA-*b*-PB.

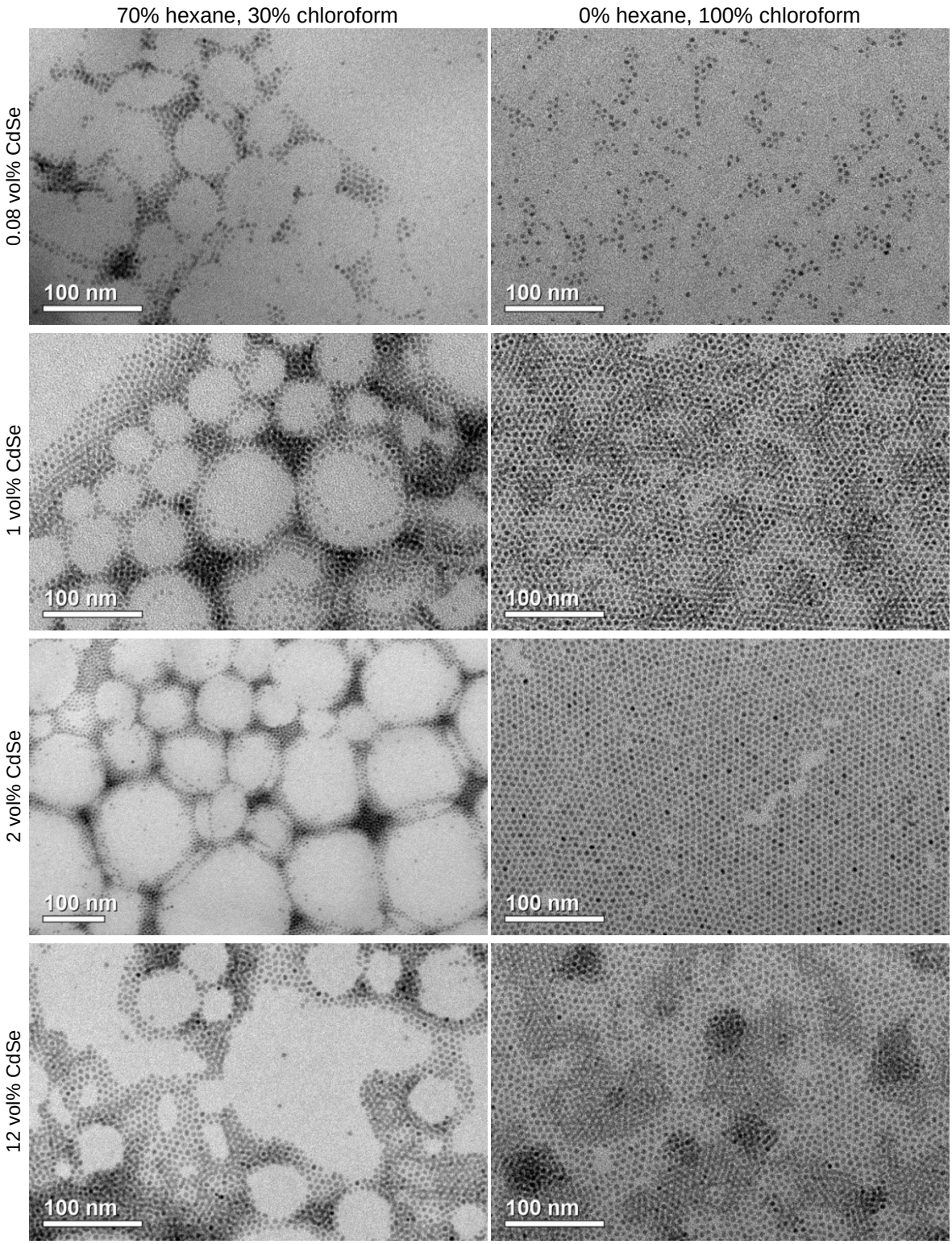

Figure 5.17: Micrographs of CdSe QDs in PLA-*b*-PB polymer dropcast from 70% hexane, 30% chloroform and 100% chloroform mixtures. The vol% of CdSe QDs in polymer varies from 0.08 vol% to 12 vol% top to bottom in this figure.

In general, contrast between different polymer blocks (PLA and PB) is poor in micrographs, whereas the QDs are readily apparent due to the high electron density of the CdSe compared to the polymer. In attempts to reveal the polymer phase behavior, some samples were stained with osmium tetroxide (OsO_4), which has been shown to stain PB.[179] The stained samples were prepared by taking TEM grids with dropcast QD-polymer films and exposing them to OsO_4 vapor for times ranging between 10 and 40 minutes. Examples of films after staining with OsO_4 are given in Figure 5.18.

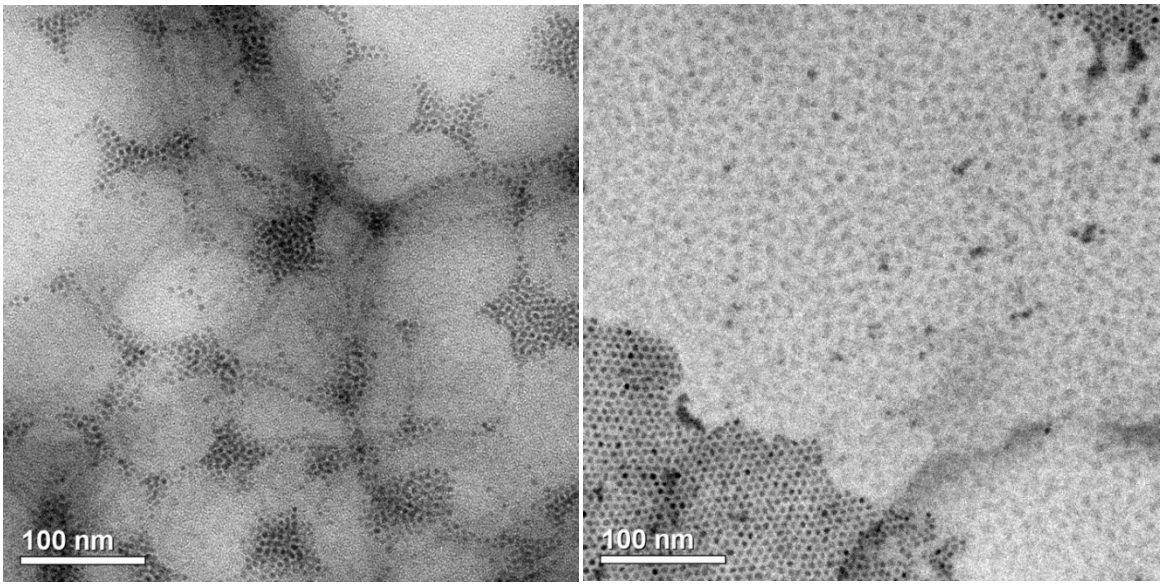

Figure 5.18: Micrographs of CdSe QDs and PLA-*b*-PB prepared from dropcasting from mixtures of 70% hexane and 30% chloroform (left) and 100% chloroform (right), after staining. Both films are 2 vol% CdSe QDs in polymer.

5.3.5 Discussion of Composite Structures

The micrographs of films (Fig. 5.15) prepared from QDs added before and after polymer micellization show the same general film structures. Both films exhibit some areas with single layer sheets of QDs as well as areas of QD multilayers where multiple QDs are stacked in a small projected area. Furthermore, both films exhibit circular motifs where QDs stack at the edges of circles (more readily apparent in the lower magnification

images). Thus, it appears that adding QDs before polymer micellization results in similar composite films to films prepared by adding QDs after polymer micellization. This result is unsurprising given the DLS data of polymer-QD dispersions where the QDs are added prior to, or after, polymer micellization (Figure 5.14). In both cases, distinctly separate populations of QDs and micelles are evident in the hydrodynamic radii distributions at ~4 nm for QD and 10-20 nm for micelles; this suggests that the polymer micellization process in solvent does not capture the majority of the QDs. Small changes in the peak location of the micelles (from ~15 nm to ~19 nm) are evident when micelles and QDs are both present in dispersion; this is attributed to limits in the REPES model.[100] In general, these two size populations are at the limit of the model's resolution for identifying two separate populations, given the five-fold increase between the positions of the smaller peak and the larger peak. Furthermore, DLS of dispersions featuring increased QD concentration see an increase in peak intensity associated with QDs at ~4 nm, but do not produce any changes in the intensity of the micelle peak. Hence, no appreciable change in QD dispersion is observed when the QDs are added before or after polymer micellization.

The chloroform: hexane ratio drastically affects the resulting film morphology as seen in Figure 5.16. At 50% hexane and higher, QDs collect around the edges of what appear to be roughly spherical shapes. At 30% hexane and lower, the QDs instead form sheets with islands of second and third layers of QDs. This difference in film morphology is attributed to the polymer behavior in the different solvent mixtures. At higher hexane concentrations, the mixture environment is enthalpically unfavorable for polymer mixing as the chloroform evaporates faster than the hexane, resulting in a hexane-rich environment. To minimize interaction with the solvent, the polymer forms microemulsion

droplets, which pushes the QDs to the outside of the droplets to act as a surfactant; similar QD-surfactant behavior has been demonstrated in a simpler system of CdSe QDs in a toluene-water mixture and with gold nanoparticles.[197,198] In this case, the ligands on the QD surface enthalpically favor mixing with the nonpolar solvent and stabilize the microemulsion surfaces by lowering the interfacial energy of the microemulsion droplets. Thus, as the film dries, the QDs end up in the spaces between the polymer microemulsions. This process is depicted in Figure 5.19 in a cartoon schematic. In contrast, when the hexane concentration is 30% or lower, the solvent environment is more favorable for the polymer and these microemulsion structures are no longer evident. However, from these figures, it is unclear where the polymer is in the samples prepared from lower hexane concentrations.

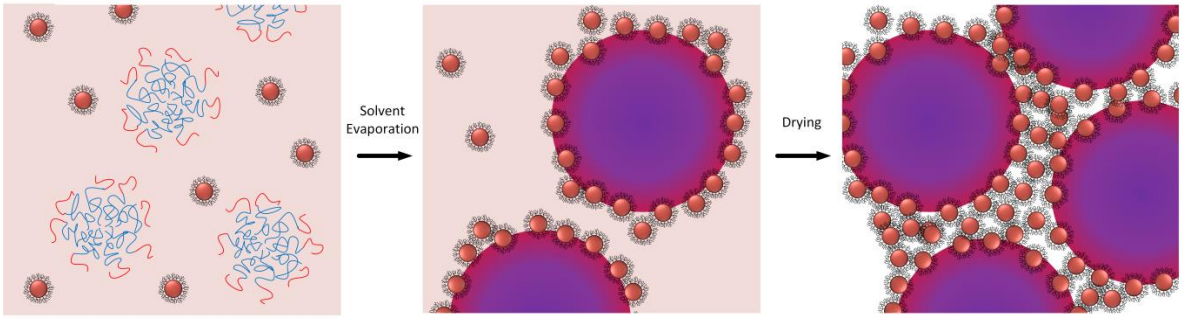

Figure 5.19: Cartoon schematic of the drying process of PLA-*b*-PB micelles with QDs from >50% hexane and <50% chloroform mixtures. Before drying, PLA-*b*-PB micelles are dispersed in the solvent mixture with freely dispersed QDs. As solvent begins to evaporate, chloroform evaporates faster than hexane, resulting in higher proportions of hexane. The polymer forms a microemulsion with QDs acting as a surfactant on the emulsion edges. As the solvent continues to evaporate, the QDs remain stuck between microemulsion polymer droplets as they dry into a film.

The staining results shown in Figure 5.18 help identify the differences in polymer structure and organization for the two extreme cases of 70% hexane and 30% chloroform, and 100% chloroform. The 70% hexane and 30% chloroform case does not indicate any

ordered polymer structure but confirms the presence of polymer around the QDs as the film shows staining in the void spaces between QDs. In the case of 100% chloroform, the polymer demonstrates spherical forming morphology separated from the QDs. In this figure, the single layer of QDs borders a section of sphere-forming polymer film. Although some small number of QDs ends up in this polymer film, the vast majority of QDs are separated from the polymer in the sheet-forming behavior evident in the unstained samples (Figure 5.16).

The QD spacing obtained from analyzing fast Fourier transforms of TEM micrographs (Table 5.5) confirms that there is little mixing between QDs and polymer across samples prepared from all solvent mixtures. The center-to-center spacing between QDs dropcast from hexane is 6.8 ± 0.4 nm (as demonstrated in the example in Chapter 2). The center-to-center spacing between QDs dropcast with PLA-*b*-PB given in Table 5.5 is similar to this value for any given ratio of hexane to chloroform. In some films, there are examples of areas where single QDs are ~20 nm away from their closest neighbor, but there appears to be no correlation between them nor does staining reveal any underlying polymer structure.

The vol% of CdSe QDs in the PLA-*b*-PB film appears to have little effect on the resulting film structure for concentrations up to 12 vol% CdSe. Figure 5.17 shows a range of concentrations from 0.08 vol% CdSe to 12 vol% CdSe (roughly 1 QD per polymer sphere) for both 70% hexane and 30% chloroform and 100% chloroform. Across all QD concentrations for a given solvent mixture, the same general morphology is observed. In the case of 70% hexane and 30% chloroform, the QDs collect in the spaces between

polymer microemulsions. In the case of 100% chloroform, the QDs form layers of sheets separated from the polymer.

Ultimately, there are entropic constraints associated with the polymer trying to fill space around a hard QD core that limit the formation of well-dispersed QD-polymer composites. For the QDs to fit into polymer spheres, the QDs should reduce the packing stress of the polymer to fill space in that sphere. A favorable QD-polymer composite may be designed from calculations based on the curvature of the QD surface and polymer packing constraints. In this study, the QD size (radius of 2.3 nm) is comparable to the polymer particle size in the bulk (radius of 5.1 nm for polymer core + corona). Given the neat PLA-*b*-PB unit cell parameter (11.7 nm) and the volume fraction of PB (0.19), the volume of each PB sphere is roughly 152 nm^3. For comparison, each QD core is approximately 51 nm^3 without ligands, or roughly double that volume with ligands. Although the ligand coverage is expected to tolerate interdigitating ligands or polymer chains, the comparative volume of the QD with ligands is on the same order of magnitude as the PB core of the polymer sphere. Thus, to fit a single QD in the PB core would require the volume of each core to almost double, and induces a loss in polymer conformational entropy as the PB must stretch to surround the QD sphere.[73,74] It is important to note that if the ligands on the surface of the QD enthalpically favor mixing with the minority polymer block, the QDs effectively increase the volume fraction of the minority block. To combat this, one solution may be the addition of majority block homopolymer to maintain the effective volume fraction of minority and majority block components. For example, if the addition of the QDs increases the effective volume fraction of the minority block by 25%, a polymer originally featuring a volume fraction

of 0.16 would now increase to 0.2. At sufficient degree of polymerization ($\chi N > \sim 24$ from Figure 1.5), this would essentially encourage a phase transformation from BCC structure to hexagonally close packed cylinders. Similar changes in phase morphology have been theoretically predicted and experimentally demonstrated (*i.e.* transition from hexagonally packed cylinders to lamellae) upon incorporation of nanoparticles,[160,199-204] and a Monte Carlo simulation of particles preferring the minority polymer block exhibited new microphase ordering that leads to phase separation when the particle size is comparable to the minority polymer block radius of gyration.[154] Thus, addition of the majority block homopolymer may balance the addition of QDs to maintain the original volume fraction of the sphere-forming polymer morphology. Alternatively, a block copolymer with a minority block volume fraction so small as to not exhibit ordered phase behavior may develop an ordered structure upon the incorporation of QDs featuring ligands enthalpically favored to mix with the minority block. While studies have demonstrated the capacity of nanoparticles to produce changes in polymer morphology there is not yet an example of nanoparticles or QDs inducing polymer order in a polymer system that does not exhibit ordered phase behavior in the neat bulk.

The enthalpic environment can potentially be better managed using solvent annealing to maintain a specific solvent environment during film drying. In this case, the formation of polymer micelles in dispersion required a high concentration of hexane that proved problematic during the drying process as it led to the formation of polymer microemulsions. Better control of the solvent vapor pressures may be a viable method to determine a pathway of micelle inversion to capture QDs. Exhaustive studies could be performed to assess the resulting structure of QD-polymer composites as a function of the

solvent vapor pressure during the drying process. This type of study would greatly benefit from in-situ microscopy where the QD placement could be readily observed in real-time as the film dries from dispersion.

In conclusion, the route towards QD encapsulation using micelles is complicated and depends heavily on the path taken. In this case, although inverted polymer micelles separate from QDs were present in solution and confirmed by DLS, the inversion of the polymer micelles to form a film did not successfully capture the QDs in the polymer sphere-forming morphology. Whereas QD concentration and incorporation into the polymer-solvent mixture before as opposed to after polymer micellization appeared to have little effect on the subsequent film structure, the solvent mixture drastically changed the resulting film morphology between polymer microemulsion and polymer sphere-forming morphology separate of the QDs.

Bibliography

1. Alivisatos, A. P. Semiconductor Clusters, Nanocrystals, and Quantum Dots. *Science.* **271,** 933–937 (1996).

2. Murray, C. B., Kagan, C. R., Bawendi, M. G. Synthesis and Characterization of Monodisperse Nanocrystals and Close-Packed Nanocrystal Assemblies. *Annu. Rev. Mater. Sci.* **30,** 545–610 (2000).

3. Brus, L. Chemical approaches to semiconductor nanocrystals. *J. Phys. Chem. Solids* **59,** 459–465 (1998).

4. Meulenberg, R. W., Lee, J. R. I., Wolcott, A., Zhang, J. Z., Terminello, L. J., van Buuren, T. Determination of the exciton binding energy in CdSe quantum dots. *ACS Nano* **3,** 325–330 (2009).

5. Mao, H., Chen, J., Wang, J., Li, Z., Dai, N., Zhu, Z. Photoluminescence investigation of CdSe quantum dots and the surface state effect. *Phys. E Low-Dimensional Syst. Nanostructures* **27,** 124–128 (2005).

6. Ashoori, R. C. Electrons in artificial atoms. *Nature* **379,** 413–419 (1996).

7. Liu, W., Howarth, M., Greytak, A. B., Zheng, Y., Nocera, D. G., Ting, A. Y., Bawendi, M. G. Compact Biocompatible Quantum Dots Functionalized for Cellular Imaging. *J. Am. Chem. Soc.* **130,** 1274–1284 (2008).

8. Chan, W. C., Nie, S. Quantum dot bioconjugates for ultrasensitive nonisotopic detection. *Science* **281,** 2016–2018 (1998).

9. Gao, X., Yang, L., Petros, J. A., Marshall, F. F., Simons, J. W., Nie, S. In vivo molecular and cellular imaging with quantum dots. *Curr. Opin. Biotechnol.* **16,** 63–72 (2005).

10. Gao, X., Cui, Y., Levenson, R. M., Chung, L. W. K., Nie, S. In vivo cancer targeting and imaging with semiconductor quantum dots. *Nat. Biotechnol.* **22,** 969–976 (2004).

11. Uyeda, H. T., Medintz, I. L., Jaiswal, J. K., Simon, S. M., Mattoussi, H. Synthesis of compact multidentate ligands to prepare stable hydrophilic quantum dot fluorophores. *J. Am. Chem. Soc.* **127,** 3870–3878 (2005).

12. Schüler, A., Python, M., del Olmo, M. V., de Chambrier, E. Quantum dot containing nanocomposite thin films for photoluminescent solar concentrators. *Sol. Energy* **81,** 1159–1165 (2007).

13. Purcell-Milton, F., Gun'ko, Y. K. Quantum dots for Luminescent Solar Concentrators. *J. Mater. Chem.* **22,** 16687–16697 (2012).

14. Coropceanu, I., Bawendi, M. G. Core/shell quantum dot based luminescent solar concentrators with reduced reabsorption and enhanced efficiency. *Nano Lett.* **14,** 4097–4101 (2014).

15. Bomm, J., Büchtemann, A., Chatten, A. J., Bose, R., Farrell, D. J., Chan, N. L. A., Xiao, Y., Slooff, L. H., Meyer, T., Meyer, A., van Sark, W. G. J. H. M., Koole, R. Fabrication and full characterization of state-of-the-art quantum dot luminescent solar concentrators. *Sol. Energy Mater. Sol. Cells* **95,** 2087–2094 (2011).

16. Meinardi, F., Colombo, A., Velizhanin, K. A., Simonutti, R., Lorenzon, M., Beverina, L., Viswanatha, R., Klimov, V. I., Brovelli, S. Large-area luminescent solar concentrators based on 'Stokes-shift-engineered' nanocrystals in a mass-polymerized PMMA matrix. *Nat. Photonics* **8,** 392–399 (2014).

17. Suárez, I., Gordillo, H., Abargues, R., Albert, S., Martínez-Pastor, J. Photoluminescence waveguiding in CdSe and CdTe QDs-PMMA nanocomposite films. *Nanotechnology* **22,** 435202 (2011).

18. Kwak, J., Bae, W. K., Lee, D., Park, I., Lim, J., Park, M., Cho, H., Woo, H., Yoon, D. Y., Char, K., Lee, S., Lee, C. Bright and Efficient Full-Color Colloidal Quantum Dot Light-Emitting Diodes Using an Inverted Device Structure. *Nano Lett.* **12**, 2362-2366 (2012).

19. Wood, V., Panzer, M. J., Chen, J., Bradley, M. S., Halpert, J. E., Bawendi, M. G., Bulovic, V. Inkjet-Printed Quantum Dot-Polymer Composites for Full-Color AC-Driven Displays. *Adv. Mater.* **21,** 2151–2155 (2009).

20. Leschkies, K. S., Divakar, R., Basu, J., Enache-Pommer, E., Boercker, J. E., Carter, C. B., Kortshagen, U. R., Norris, D. J., Aydil, E. S. Photosensitization of ZnO Nanowires with CdSe Quantum Dots for Photovoltaic Devices. *Nano Lett.* **7,** 1793–1798 (2007).

21. Leschkies, K. S., Beatty, T. J., Kang, M. S., Norris, D. J. & Aydil, E. S. Solar Cells Based on Junctions between Colloidal PbSe Nanocrystals and Thin ZnO Films. *ACS Nano* **3,** 3638–3648 (2009).

22. Talapin, D. V., Murray, C. B. PbSe Nanocrystal Solids for n- and p-Channel Thin Film Field-Effect Transistors. *Science* **310,** 86–89 (2005).

23. Mangolini, L., Kortshagen, U. Plasma-assisted synthesis of silicon nanocrystal inks. *Adv. Mater.* **19,** 2513–2519 (2007).

24. Talapin, D. V., Lee, J.-S., Kovalenko, M. V., Shevchenko, E. V. Prospects of colloidal nanocrystals for electronic and optoelectronic applications. *Chem. Rev.* **110,** 389–458 (2010).

25. Murray, C. B., Kagan, C. R., Bawendi, M. G. Self-Organization of CdSe Nanocrystallites into Three-Dimensional Quantum Dot Superlattices. *Science* **270,** 1335–1338 (1995).

26. Talapin, D. V., Shevchenko, E. V., Murray, C. B., Titov, A. V., Král, P. Dipole - Dipole interactions in nanoparticle superlattices. *Nano Lett.* **7,** 1213–1219 (2007).

27. Fischer, S., Salcher, A., Kornowski, A., Weller, H., Förster, S. Completely Miscible Nanocomposites. *Angew. Chemie* **123,** 7957–7960 (2011).

28. Shevchenko, E. V., Talapin, D. V., Kotov, N. A., O'Brien, S., Murray, C. B. Structural diversity in binary nanoparticle superlattices. *Nature* **439,** 55–59 (2006).

29. Chen, Z., Moore, J., Radtke, G., Sirringhaus, H., O'Brien, S. Binary Nanoparticle Superlattices in the Semiconductor-Semiconductor System: CdTe and CdSe. *J. Am. Chem. Soc.* **129,** 15702–15709 (2007).

30. Shevchenko, E. V., Talapin, D. V., Murray, C. B., O'Brien, S. Structural Characterization of Self-Assembled Multifunctional Binary Nanoparticle Superlattices. *J. Am. Chem. Soc.* **128,** 3620–3637 (2006).

31. Kiely, C. J., Fink, J., Brust, M., Bethell, D., Schiffrin, D. J. Spontaneous ordering of bimodal ensembles of nanoscopic gold clusters. *Nature* **396,** 444–446 (1998).

32. Redl, F. X., Cho, K.-S., Murray, C. B., O'Brien, S. Three-dimensional binary superlattices of magnetic nanocrystals and semiconductor quantum dots. *Nature* **423,** 968–971 (2003).

33. Talapin, D. V., Shevchenko, E. V., Bodnarchuk, M. I., Ye, X., Chen, J., Murray, C. B. Quasicrystalline order in self-assembled binary nanoparticle superlattices. *Nature* **461,** 964–967 (2009).

34. Martin, J. E., Wilcoxon, J. P., Odinek, J., Provencio, P. Control of the Interparticle Spacing in Gold Nanoparticle Superlattices. *J. Phys. Chem. B* **104,** 9475–9486 (2000).

35. Goodyear, C. Goodyear's Verfahren zur Fabrication von Gegenständen aus Kautschuk und Gutta-percha. *Polytech. J.* **139,** 376–390 (1856).

36. Kojima, Y., Usuki, A., Kawasumi, M., Okada, A., Fukushima, Y., Kurauchi, T., Kamigaito, O. Mechanical properties of nylon 6-clay hybrid. *J. Mater. Res.* **8,** 1185–1189 (1993).

37. Usuki, A., Kojima, Y., Kawasumi, M., Okada, A., Fukushima, Y., Kurauchi, T., Kamigaito, O. Synthesis of nylon 6-clay hybrid. *J. Mater. Res.* **8,** 1179–1184 (1993).

38. Haryono, A., Binder, W. H. Controlled arrangement of nanoparticle arrays in block-copolymer domains. *Small* **2,** 600–611 (2006).

39. Mehdizadeh Taheri, S., Fischer, S., Förster, S. Routes to Nanoparticle-Polymer Superlattices. *Polymers* **3,** 662–673 (2011).

40. Bates, F. S., Fredrickson, G. H. Block Copolymers—Designer Soft Materials. *Phys. Today* **52,** 32–38 (1999).

41. Bates, F. S., Fredrickson, G. H. Block Copolymer Thermodynamics: Theory and Experiment. *Annu. Rev. Phys. Chem.* **41,** 525–557 (1990).

42. Vavasour, J. D., Whitmore, M. D. Self-Consistent Field Theory of Block Copolymers with Conformational Asymmetry. *Macromolecules* **26,** 7070–7075 (1993).

43. Leibler, L. Theory of Microphase Separation in Block Copolymers. *Macromolecules* **13,** 1602–1617 (1980).

44. Matsen, M. W. The standard Gaussian model for block copolymer. *J. Phys. Condens. Matter* **14,** R21–R47 (2002).

45. Castelletto, V., Hamley, I. W. Morphologies of block copolymer melts. *Curr. Opin. Solid State Mater. Sci.* **8,** 426–438 (2004).

46. Lee, S., Bluemle, M. J., Bates, F. S. Discovery of a Frank-Kasper sigma phase in Sphere-Forming Block Copolymer Melts. *Science* **330,** 349–353 (2010).

47. Lee, S., Gillard, T. M., Bates, F. S. Fluctuations, Order, and Disorder in Short Diblock Copolymers. *AIChE J.* **59,** 3502-3513 (2013).

48. Zhang, J., Bates, F. S. Dodecagonal Quasicrystalline Morphology in a Poly(styrene-b-isoprene-b-styrene-b-ethylene oxide) Tetrablock Terpolymer. *J. Am. Chem. Soc.* **134,** 7636–7639 (2012).

49. Dubois, J.-M. Properties- and applications of quasicrystals and complex metallic alloys. *Chem. Soc. Rev.* **41,** 6760-6777 (2012).

50. Zoorob, M. E., Charlton, M. D. B., Parker, G. J., Baumberg, J. J., Netti, M. C. Complete photonic bandgaps in 12-fold symmetric quasicrystals. *Nature* **404,** 740–743 (2000).

51. Fischer, S., Exner, A., Zielske, K., Perlich, J., Deloudi, S., Steurer, W., Lindner, P., Förster, S. Colloidal quasicrystals with 12-fold and 18-fold diffraction symmetry. *PNAS* **108**, 1810-1814 (2010).

52. Man, W., Megens, M., Steinhardt, P. J., Chaikin, P. M. Experimental measurement of the photonic properties of icosahedral quasicrystals. *Nature* **436,** 993–996 (2005).

53. Sankaran, V., Yue, J., Cohen, R. E., Schrock, R. R., Silbey, R. J. Synthesis of Zinc Sulfide Clusters and Zinc Particles within Microphase-Separated Domains of Organometallic Block Copolymers. *Chem. Mater.* **5,** 1133–1142 (1993).

54. Kane, R. S., Cohen, R. E., Silbey, R. Synthesis of PbS Nanoclusters within Block Copolymer Nanoreactors. *Chem. Mater.* **8,** 1919–1924 (1996).

55. Fogg, D. E., Radzilowski, L. H., Blanski, R., Schrock, R. R., Thomas, E. L. Fabrication of Quantum Dot/Polymer Composites: Phosphine-Functionalized Block Copolymers as Passivating Hosts for Cadmium Selenide Nanoclusters. *Macromolecules* **30,** 417–426 (1997).

56. Kane, R. S., Cohen, R. E., Silbey, R. Semiconductor Nanocluster Growth within Polymer Films. *Langmuir* **15,** 39–43 (1999).

57. Kane, R. S., Cohen, R. E., Silbey, R. Synthesis of Doped ZnS Nanoclusters within Block Copolymer Nanoreactors. *Chem. Mater.* **11,** 90–93 (1999).

58. Gratt, J. A., Cohen, R. E. Optical Properties of Block Copolymers Containing Pendant Carbazole Groups and In Situ Synthesized CdS Nanoclusters. *J. Appl. Polym. Sci.* **88,** 177–182 (2003).

59. Abes, J. I., Cohen, R. E., Ross, C. A. Selective Growth of Cobalt Nanoclusters in Domains of Block Copolymer Films. *Chem. Mater* **15,** 1125–1131 (2003).

60. Sill, K., Emrick, T. Nitroxide-Mediated Radical Polymerization from CdSe Nanoparticles. *Chem. Mater* **16,** 1240–1243 (2004).

61. Pyun, J., Matyjaszewski, K. Synthesis of Nanocomposite Organic/Inorganic Hybrid Materials Using Controlled/"Living" Radical Polymerization. *Chem. Mater.* **13,** 3436–3448 (2001).

62. Park, J. T., Koh, J. H., Koh, J. K. & Kim, J. H. Surface-initiated atom transfer radical polymerization from TiO2 nanoparticles. *Appl. Surf. Sci.* **255,** 3739–3744 (2009).

63. Morinaga, T., Ohkura, M., Ohno, K., Tsujii, Y., Fukuda, T. Monodisperse Silica Particles Grafted with Concentrated Oxetane-Carrying Polymer Brushes: Their

Synthesis by Surface-Initiated Atom Transfer Radical Polymerization and Use for Fabrication of Hollow Spheres. *Macromolecules* **40,** 1159–1164 (2007).

64. Wang, T.-L., Ou, C.-C., Yang, C.-H. Synthesis and Properties of Organic/Inorganic Hybrid Nanoparticles Prepared Using Atom Transfer Radical Polymerization. *J. Appl. Polym. Sci.* **109,** 3421–3430 (2008).

65. Boal, a. K., Galow, T. H., Ilhan, F., Rotello, V. M. Binary and Ternary Polymer-Mediated 'Bricks and Mortar' Self-Assembly of Gold and Silica Nanoparticles. *Adv. Funct. Mater.* **11,** 461–465 (2001).

66. Bockstaller, M. R., Lapetnikov, Y., Margel, S., Thomas, E. L., Size-Selective Organization of Enthalpic Compatibilized Nanocrystals in Ternary Block Copolymer/Particle Mixtures. *J. Am. Chem. Soc* **125,** 5276–5277 (2003).

67. Sohn, B.-H., Choi, J.-M., Yoo, S. I., Yun, S.-H., Zin, W.-C., Jung, J. C., Kanehara, M., Hirata, T., Teranishi, T. Directed Self-Assembly of Two Kinds of Nanoparticles Utilizing Monolayer Films of Diblock Copolymer Micelles. *J. Am. Chem. Soc.* **125,** 6368–6369 (2003).

68. Lin, Y., Böker, A., He, J., Sill, K., Xiang, H., Abetz, C., Li, X., Wang, J., Emrick, T., Long, S., Wang, Q., Balazs, A., Russell, T. P. Self-directed self-assembly of nanoparticle/copolymer mixtures. *Nature* **434,** 55–59 (2005).

69. Chiu, J. J., Kim, B. J., Kramer, E. J., Pine, D. J. Control of nanoparticle location in block copolymers. *J. Am. Chem. Soc.* **127,** 5036–5037 (2005).

70. Förster, S., Plantenberg, T. From Self-Organizing Polymers to Nanohybrid and Biomaterials. *Angew. Chem. Int. Ed. Engl.* **41,** 688–714 (2002).

71. Bomm, J., Fabrication and spectroscopic studies on highly luminescent CdSe/CdS nanorod polymer composites. *Beilstein J. Nanotechnol.* **1,** 94–100 (2010).

72. Milner, S. T. Polymer Brushes. *Science* **251,** 905–914 (1991).

73. Thompson, R. B., Ginzburg, V. V., Matsen, M. W., Balazs, A. C. Predicting the mesophases of copolymer-nanoparticle composites. *Science* **292,** 2469–2472 (2001).

74. Balazs, A. C., Emrick, T., Russell, T. P. Nanoparticle polymer composites: where two small worlds meet. *Science* **314,** 1107–1110 (2006).

75. Schultz, A. J., Hall, C. K., Genzer, J., Carolina, N. Computer Simulation of Block Copolymer/Nanoparticle Composites. *Macromolecules* **38,** 3007–3016 (2005).

76. Wang, Q., Nealey, P. F., de Pablo, J. J. Behavior of single nanoparticle/homopolymer chain in ordered structures of diblock copolymers. *J. Chem. Phys.* **118,** 11278–11285 (2003).

77. Schmaltz, B., Brinkmann, M., Mathis, C. Nanoscale Organization of Fullerenes by Self-Assembly in a Diblock Copolymer Host Matrix. *Macromolecules* **37,** 9056–9063 (2004).

78. Spatz, J. P. Nano- and Micropatterning by Organic-Inorganic Templating of Hierarchical. *Angew. Chem. Int. Ed. Engl.* **41,** 3359–3362 (2002).

79. Mackay, M. E., Tuteja, A., Duxbury, P. M., Hawker, C. J., Van Horn, B., Guan, Z., Chen, G., Krishnan, R. S., General strategies for nanoparticle dispersion. *Science* **311,** 1740–1743 (2006).

80. Chiu, J. J., Kim, B. J., Yi, G.-R., Bang, J., Kramer, E. J., Pine, D. J. Distribution of Nanoparticles in Lamellar Domains of Block Copolymers. *Macromolecules* **40,** 3361–3365 (2007).

81. Chen, O., Zhao, J., Chauhan, V. P., Cui, J., Wong, C., Harris, D. K., Wei, H., Han, H.-S., Fukumura, D., Jain, R. K., Bawendi, M. G. Compact high-quality CdSe-CdS core-shell nanocrystals with narrow emission linewidths and suppressed blinking. *Nat. Mater.* **12,** 445–451 (2013).

82. Wenger, W. N., Bates, F. S., Aydil, E. S. Functionalization of Cadmium Selenide Quantum Dots with Poly(ethylene glycol): Ligand Exchange, Surface Coverage, and Dispersion Stability. *Langmuir* **33,** 8239–8245 (2017).

83. Reiss, P., Bleuse, J., Pron, A. Highly luminescent CdSe/ZnSe core/shell nanocrystals of low size dispersion. *Nano Lett.* **2,** 781–784 (2002).

84. Peng, Z. A., Peng, X. Formation of high-quality CdTe, CdSe, and CdS nanocrystals using CdO as precursor. *J. Am. Chem. Soc.* **123,** 183–184 (2001).

85. Jasieniak, J., Bullen, C., van Embden, J., Mulvaney, P. Phosphine-free synthesis of CdSe nanocrystals. *J. Phys. Chem. B* **109,** 20665–20668 (2005).

86. Dabbousi, B. O., (CdSe)ZnS Core-Shell Quantum Dots: Synthesis and Characterization of a Size Series of Highly Luminescent Nanocrystallites. *J. Phys. Chem. B* **101,** 9463–9475 (1997).

87. Reiss, P., Protière, M., Li, L. Core/Shell Semiconductor Nanocrystals. *Small* **5,** 154–168 (2009).

88. Chen, Y., Vela, J., Htoon, H., Casson, J. L., Werder, D. J., Bussian, D. A., Klimov, V. I., Hollingsworth, J. A. "Giant" multishell CdSe nanocrystal quantum dots with suppressed blinking. *J. Am. Chem. Soc.* **130,** 5026–5027 (2008).

89. Jasieniak, J., Smith, L., Embden, J. Van, Mulvaney, P., Califano, M. Re-examination of the Size-Dependent Absorption Properties of CdSe Quantum Dots. *J. Phys. Chem. C* **113,** 19468–19474 (2009).

90. Talapin, D. V, Rogach, A. L., Kornowski, A., Haase, M., Weller, H. Highly Luminescent Monodisperse CdSe and CdSe/ZnS Nanocrystals Synthesized in a Hexadecylamine−Trioctylphosphine Oxide−Trioctylphospine Mixture. *Nano Lett.* **1,** 207–211 (2001).

91. Young, A. G., Al-Salim, N., Green, D. P., McQuillan, A. J. Attenuated total reflection infrared studies of oleate and trioctylphosphine oxide ligand adsorption and exchange reactions on CdS quantum dot films. *Langmuir* **24,** 3841–3849 (2008).

92. Eilon, M. J., Mokari, T., Banin, U. Surface exchange effect on hyper Rayleigh scattering in CdSe nanocrystals. *J. Phys. Chem. B* **105,** 12726–12731 (2001).

93. Katari, J. E. B., Colvin, V. L., Alivisatos, A. P. X-ray photoelectron spectroscopy of CdSe nanocrystals with applications to studies of the nanocrystal surface. *J. Phys. Chem.* **98,** 4109–4117 (1994).

94. Al-Salim, N., Young, A. G., Tilley, R. D., McQuillan, A. J., Xia, J. Synthesis of CdSeS Nanocrystals in Coordinating and Noncoordinating solvents: Solvent's Role in Evolution of the Optical and Structural Properties. *Chem. Mater.* **19,** 5185–5193 (2007).

95. Murray, C. B., Norris, D. J., Bawendi, M. G. Synthesis and Characterization of Nearly Monodisperse CdE (E = S, Se, Te) Semiconductor Nanocrystallites. *J. Am. Chem. Soc* **115,** 8706–8715 (1993).

96. Kandasamy, K., Singh, H. B., Kulshreshtha, S. K. Synthesis and characterization of CdS and CdSe nanoparticles prepared from novel intramolecularly stabilized single-source precursors. *J. Chem. Sci.* **121,** 293–296 (2009).

97. Tolbert, S. H., Alivisatos, A. P. The wurtzite to rock salt structural transformation in CdSe nanocrystals under high pressure. *J. Chem. Phys.* **102,** 4642–4656 (1995).

98. Peng, X., Manna, L., Yang, W., Wickham, J., Scher, E., Kadavanich, A., Alivisatos, A. P., Shape control of CdSe nanocrystals. *Nature* **404,** 59–61 (2000).

99. Tillmann, K., Jäger, W. Quantitative HRTEM analysis of semiconductor quantum dots. *J. Electron Microsc.* **49,** 101–113 (2000).

100. Jakeš, J. Testing of the constrained regularization method of inverting Laplace transform on simulated very wide quasielastic light scattering autocorrelation functions. *Czechoslov. J. Phys.* **38,** 1305–1316 (1988).

101. Nikolic, M. S., Krack, M., Aleksandrovic, V., Kornowski, A., Förster, S., Weller, H. Tailor-made ligands for biocompatible nanoparticles. *Angew. Chem. Int. Ed. Engl.* **45,** 6577–6580 (2006).

102. Mehata, M. S. Enhancement of Charge Transfer and Quenching of Photoluminescence of Capped CdS Quantum Dots. *Sci. Rep.* **5**, 1–11 (2015).

103. Debije, M. G., Verbunt, P. P. C. Thirty Years of Luminescent Solar Concentrator Research: Solar Energy for the Built Environment. *Adv. Energy Mater.* **2,** 12–35 (2012).

104. Meinardi, F., Colombo, A., Velizhanin, K. A., Simonutti, R., Lorenzon, M., Beverina, L., Viswanatha, R., Klimov, V. I., Brovelli, S. Large-area luminescent solar concentrators based on 'Stokes-shift-engineered' nanocrystals in a mass-polymerized PMMA matrix. *Nat. Photonics* **8,** 392–399 (2014).

105. Susumu, K., Uyeda, H. T., Medintz, I. L., Pons, T., Delehanty, J. B., Mattoussi, H. Enhancing the Stability and Biological Functionalities of Quantum Dots via Compact Multifunctional Ligands. *J. Am. Chem. Soc* **129,** 13987–13996 (2007).

106. Lee, J., Kim, J., Park, E., Jo, S., Song, R. PEG-ylated cationic CdSe/ZnS QDs as an efficient intracellular labeling agent. *Phys. Chem. Chem. Phys.* **10,** 1739–1742 (2008).

107. Mei, B. C., Susumu, K., Medintz, I. L., Delehanty, J. B., Mountziaris, T. J., Mattoussi, H. Modular poly(ethylene glycol) ligands for biocompatible semiconductor and gold nanocrystals with extended pH and ionic stability. *J. Mater. Chem.* **18,** 4949-4958 (2008).

108. Thiry, M., Boldt, K., Nikolic, M. S., Schulz, F., Ijeh, M., Panicker, A., Vossmeyer, T., Weller, H. Fluorescence properties of hydrophilic semiconductor nanoparticles with tridentate polyethyleneoxide ligands. *ACS Nano* **5**, 4965-4973 (2011).

109. Sondi, I., Siiman, O., Koester, S., Matijevic, E. Preparation of Aminodextran - CdS Nanoparticle Complexes and Biologically Active Antibody - Aminodextran - CdS Nanoparticle Conjugates. *Langmuir* **16,** 3107–3118 (2000).

110. Rogach, A. L., Kornowski, A., Gao, M., Eychmüller, A., Weller, H. Synthesis and Characterization of a Size Series of Extremely Small Thiol-Stabilized CdSe Nanocrystals. *J. Phys. Chem. B* **103,** 3065–3069 (1999).

111. Tosun, B. S., Chernomordik, B. D., Gunawan, A. A., Williams, B., Mkhoyan, K. A., Francis, L. F., Aydil, E. S. Cu_2ZnSnS_4 nanocrystal dispersions in polar liquids. *Chem. Commun.* **49,** 3549–3551 (2013).

112. Heath, J. R., Knobler, C. M., Leff, D. V. Pressure/Temperature Phase Diagrams and Superlattices of Organically Functionalized Metal Nanocrystal Monolayers: The Influence of Particle Size, Size Distribution, and Surface Passivant. *J. Phys. Chem. B* **101,** 189–197 (1997).

113. Bullen, C., Mulvaney, P. The effects of chemisorption on the luminescence of CdSe quantum dots. *Langmuir* **22,** 3007–3013 (2006).

114. Hiemenz, P. C., Lodge, T. P. *Polymer Chemistry*. (CRC Press, 2007).

115. Bockstaller, M. R., Mickiewicz, R. A., Thomas, E. L. Block Copolymer Nanocomposites: Perspectives for Tailored Functional Materials. *Adv. Mater.* **17,** 1331–1349 (2005).

116. Meli, L., Arceo, A., Green, P. F. Control of the entropic interactions and phase behavior of athermal nanoparticle/homopolymer thin film mixtures. *Soft Matter* **5,** 533-537 (2009).

117. Green, P. F. The structure of chain end-grafted nanoparticle/homopolymer nanocomposites. *Soft Matter* **7**, 7914–7926 (2011).

118. Hooper, J. B., Schweizer, K. S. Theory of Phase Separation in Polymer Nanocomposites. *Macromolecules* **39,** 5133–5142 (2006).

119. Park, S. J., Kim, S., Yong, D., Choe, Y., Bang, J., Kim, J. U. Interactions between brush-grafted nanoparticles within chemically identical homopolymers: The effect of brush polydispersity. *Soft Matter* **14,** 1026–1042 (2018).

120. Ganesan, V., Ellison, C. J., Pryamitsyn, V. Mean-field models of structure and dispersion of polymer-nanoparticle mixtures. *Soft Matter* **6,** 4010–4025 (2010).

121. Moniruzzaman, M., Winey, K. I. Polymer nanocomposites containing carbon nanotubes. *Macromolecules* **39,** 5194–5205 (2006).

122. Jayaraman, A., Nair, N. Integrating PRISM theory and Monte Carlo simulation to study polymer-functionalised particles and polymer nanocomposites. *Mol. Simul.* **38,** 751–761 (2012).

123. Crosby, A. J., Lee, J. Y. Polymer Nanocomposites: The "Nano" Effect on Mechanical Properties. *Polym. Rev.* **47,** 217–229 (2007).

124. Oberdisse, J. Aggregation of colloidal nanoparticles in polymer matrices. *Soft Matter* **2,** 29–36 (2006).

125. Grossiord, N., Loos, J., Regev, O., Koning, C. E. Toolbox for dispersing carbon nanotubes into polymers to get conductive nanocomposites. *Chem. Mater.* **18,** 1089–1099 (2006).

126. Hilding, J., Grulke, E., George Zhang, Z., Lockwood, F. Dispersion of Carbon Nanotubes in Liquids. *J. Dispers. Sci. Technol.* **24,** 1–41 (2003).

127. Ferreira, P. G., Ajdari, A., Leibler, L. Scaling law for entropic effects at interfaces between grafted layers and polymer melts. *Macromolecules* **31,** 3994–4003 (1998).

128. Jain, S., Ginzburg, V. V., Jog, P., Weinhold, J., Srivastava, R., Chapman, W. G. Modeling polymer-induced interactions between two grafted surfaces: Comparison between interfacial statistical associating fluid theory and self-consistent field theory. *J. Chem. Phys.* **131,** 044908 (2009).

129. Gast, A. P., Leibler, L. Interactions of Sterically Stabilized Particles Suspended in a Polymer Solution. *Macromolecules* **19,** 686–691 (1986).

130. Borukhov, I., Leibler, L. Enthalpic stabilization of brush-coated particles in a polymer melt. *Macromolecules* **35,** 5171–5182 (2002).

131. Trombly, D. M., Ganesan, V. Curvature effects upon interactions of polymer-grafted nanoparticles in chemically identical polymer matrices. *J. Chem. Phys.* **133,** 154904 (2010).

132. Oh, H., Green, P. F. Polymer chain dynamics and glass transition in athermal polymer/nanoparticle mixtures. *Nat. Mater.* **8,** 139–143 (2009).

133. Yeung, C., Balazs, A. C., Jasnow, D. Lateral Instabilities in a Grafted Layer in a Poor Solvent. *Macromolecules* **26,** 1914–1921 (1993).

134. Huang, K., Balazs, A. C. A Two-Dimensional Self-Consistent-Field Model for Grafted Chains: Determining the Properties of Grafted Homopolymers in Poor Solvents. *Macromolecules* **26,** 4736–4738 (1993).

135. McGarrity, E. S., Frischknecht, A. L., Frink, L. J. D., MacKay, M. E. Surface-induced first-order transition in athermal polymer-nanoparticle blends. *Phys. Rev. Lett.* **99,** 238302 (2007).

136. McGarrity, E. S., Frischknecht, A. L., Mackay, M. E. Phase behavior of polymer/nanoparticle blends near a substrate. *J. Chem. Phys.* **128,** 154904 (2008).

137. Meli, L. Microstructure design and formation of organic/inorganic thin film nanocomposites. (University of Texas, Austin, 2007).

138. Chen, X. C., Green, P. F. Structure of thin film polymer/nanoparticles systems: polystyrene (PS) coated-Au nanoparticle/tetramethyl bisphenol-A polycarbonate mixtures (TMPC). *Soft Matter* **7**, 1192–1198 (2011).

139. Kaihara, S., Matsumura, S., Mikos, A. G., Fisher, J. P. Synthesis of poly(L-lactide) and polyglycolide by ring-opening polymerization. *Nat. Protoc.* **2,** 2667–2671 (2007).

140. Polymer Database. *CROW* (2018). at <polymerdatabase.com/class index.html>

141. Kim, J., Green, P. F. Phase Behavior of Thin Film Brush-Coated Nanoparticles / Homopolymer Mixtures. *Macromolecules* **43**, 1524–1529 (2010).

142. Titov, A. V., Král, P. Modeling the self-assembly of colloidal nanorod superlattices. *Nano Lett.* **8,** 3605–3612 (2008).

143. Xu, C., Ohno, K., Ladmiral, V., Composto, R. J. Dispersion of polymer-grafted magnetic nanoparticles in homopolymers and block copolymers. *Polymer* **49,** 3568–3577 (2008).

144. Bates, F. S. An Investigation of Structure and Properties in a Model Set of Diblock Copolymer-Homopolymer Blends. (1982).

145. Bates, F. S. Measurement of the Correlation Hole in Homogeneous Block Copolymer Melts. *Macromolecules* **18,** 525–528 (1985).

146. Chevigny, C., Dalmas, F., Di Cola, E., Gigmes, D., Bertin, D., Boué, F., Jestin, J. Polymer-grafted-nanoparticles nanocomposites: Dispersion, grafted chain conformation, and rheological behavior. *Macromolecules* **44,** 122–133 (2011).

147. Srivastava, S., Agarwal, P., Archer, L. A. Tethered nanoparticle-polymer composites: Phase stability and curvature. *Langmuir* **28,** 6276–6281 (2012).

148. Kalyuzhny, G., Murray, R. W. Ligand effects on optical properties of CdSe nanocrystals. *J. Phys. Chem. B* **109,** 7012–7021 (2005).

149. Hammer, N. I., Emrick, T., Barnes, M. D. Quantum dots coordinated with conjugated organic ligands: new nanomaterials with novel photophysics. *Nanoscale Res. Lett.* **2,** 282–290 (2007).

150. Jasieniak, J., Mulvaney, P. From Cd-Rich to Se-Rich--the Manipulation of CdSe Nanocrystal Surface Stoichiometry. *J. Am. Chem. Soc.* **129,** 2841–8 (2007).

151. Li, T., Zhang, J., Schneiderman, D. K., Francis, L. F., Bates, F. S. Toughening Glassy Poly(lactide) with Block Copolymer Micelles. *ACS Macro Lett.* **5,** 359–364 (2016).

152. Jayaraman, A., Schweizer, K. S. Effective Interactions, Structure, and Phase Behavior of Lightly Tethered Nanoparticles in Polymer Melts. *Macromolecules* **41**, 9430–9438 (2008).

153. Bieligmeyer, M., Taheri, S. M., German, I., Boisson, C., Probst, C., Milius, W., Altstädt, V, Breu, J., Schmidt, H.-W., D'Agosto, F., Förster, S. Completely miscible polyethylene nanocomposites. *J. Am. Chem. Soc.* **134,** 18157–18160 (2012).

154. Huh, J., Ginzburg, V. V., Balazs, A. C. Thermodynamic Behavior of Particle/Diblock Copolymer Mixtures: Simulation and Theory. *Macromolecules* **33,** 8085–8096 (2000).

155. Lopes, W. A. Nonequilibrium self-assembly of metals on diblock copolymer templates. *Phys. Rev. E - Stat. Physics, Plasmas, Fluids, Relat. Interdiscip. Top.* **65,** 031606 (2002).

156. Pryamitsyn, V., Ganesan, V. A coarse-grained explicit solvent simulation of rheology of colloidal suspensions. *J Chem Phys* **122,** 104906 (2005).

157. Pryamitsyn, V., Ganesan, V. Strong segregation theory of block copolymer-nanoparticle composites. *Macromolecules* **39,** 8499–8510 (2006).

158. Osipov, M. A., Gorkunov, M. V., Berezkin, A. V., Kudryavtsev, Y. V. Phase behavior and orientational ordering in block copolymers doped with anisotropic nanoparticles. *Phys. Rev. E* **97,** 042706 (2018).

159. Thompson, R. B., Ginzburg, V. V., Matsen, M. W., Balazs, A. C. Block copolymer-directed assembly of nanoparticles: Forming mesoscopically ordered hybrid materials. *Macromolecules* **35,** 1060–1071 (2002).

160. Lee, J. Y., Thompson, R. B., Jasnow, D., Balazs, A. C. Effect of Nanoscopic Particles on the Mesophase Structure of Diblock Copolymers. *Macromolecules* **35,** 4855–4858 (2002).

161. Buxton, G. a, Lee, J. Y., Balazs, A. C. Computer simulation of morphlogies and optical properties of filled diblock copolymers. *Macromolecules* **36,** 9631–9637 (2003).

162. Lee, J. Y., Shou, Z., Balazs, A. C. Predicting the morphologies of confined copolymer/nanoparticle mixtures. *Macromolecules* **36,** 7730–7739 (2003).

163. Lee, J. Y., Shou, Z., Balazs, A. C. Modeling the self-assembly of copolymer-nanoparticle mixtures confined between solid surfaces. *Phys. Rev. Lett.* **91,** 136103 (2003).

164. He, G., Ginzburg, V. V., Balazs, A. C. Determining the Phase Behavior of Nanoparticle-Filled Binary Blends. *J. Polym. Sci. Part B Polym. Phys.* **44,** 2389–2403 (2006).

165. Gaines, M. K., Smith, S. D., Samseth, J., Bockstaller, M. R., Thompson, R. B., Rasmussen, K. Ø. Spontak, R. J. Nanoparticle-regulated phase behavior of ordered block copolymers. *Soft Matter* **4,** 1609–1612 (2008).

166. Matsen, M. W., Thompson, R. B. Particle distributions in a block copolymer nanocomposite. *Macromolecules* **41,** 1853–1860 (2008).

167. Hoheisel, T. N., Hur, K., Wiesner, U. B. Block copolymer-nanoparticle hybrid self-assembly. *Prog. Polym. Sci.* **40,** 3–32 (2015).

168. Sarkar, B., Alexandridis, P. Self-Assembled Block Copolymer-Nanoparticle Hybrids: Interplay between Enthalpy and Entropy. *Langmuir* **28,** 15975–15986 (2012).

169. Lauter-Pasyuk, V., Lauter, H. J., Ausserre, D., Gallot, Y., Cabuil, V., Kornilov, E. I., Hamdoun, B. Effect of nanoparticle size on the internal structure of copolymer-nanoparticles composite thin films studied by neutron reflection. *Phys. B Condens. Matter* **241-243,** 1092–1094 (1997).

170. Lauter-Pasyuk, V., Lauter, H. J., Ausserre, D., Gallot, Y., Cabuil, V., Hamdoun, B., Kornilov, E. I. Neutron reflectivity studies of composite nanoparticle - copolymer thin films. *Phys. B Condens. Matter* **248,** 243–245 (1998).

171. Hamdoun, B., Ausserré, D., Joly, S., Gallot, Y., Cabuil, V., Clinard, C. New Nanocomposite Materials *J. Phys. II France* **6,** 493–501 (1996).

172. Copolymers, D., Bockstaller, B. M., Kolb, R., Thomas, E. L. Metallodielectric Photonic Crystals Based on Diblock Copolymers. *Adv. Mater.* **13**, 1783–1786 (2001).

173. Weng, C. C., Wei, K. H. Selective Distribution of Surface-Modified TiO_2 Nanoparticles in Polystyrene-b-poly (Methyl Methacrylate) Diblock Copolymer. *Chem. Mater.* **15,** 2936–2941 (2003).

174. Bockstaller, M., Thomas, E. Proximity Effects in Self-Organized Binary Particle–Block Copolymer Blends. *Phys. Rev. Lett.* **93,** 166106 (2004).

175. Listak, J., Bockstaller, M. R. Stabilization of grain boundary morphologies in lamellar block copolymer/nanoparticle blends. *Macromolecules* **39,** 5820–5825 (2006).

176. Hickey, R. J., Gillard, T. M., Lodge, T. P., Bates, F. S. Influence of Composition Fluctuations on the Linear Viscoelastic Properties of Symmetric Diblock Copolymers near the Order–Disorder Transition. *ACS Macro Lett.* **4,** 260–265 (2015).

177. Habersberger, B. M., Gillard, T. M., Hickey, R. J., Lodge, T. P., Bates, F. S. Fluctuation Effects in Symmetric Diblock Copolymer−Homopolymer Ternary Mixtures near the Lamellar−Disorder Transition. *ACS Macro Lett.* **3,** 1041–1045 (2014).

178. Fetters, L. J., Lohse, D. J., Richter, D., Witten, T. A., Zirkel, A. Connection between Polymer Molecular Weight, Density, Chain Dimensions, and Melt Viscoelastic Properties. *Macromolecules* **27,** 4639–4647 (1994).

179. Kato, K. The osmium tetroxide procedure for light and electron microscopy of ABS plastics. *Polym. Eng. Sci.* **7,** 38–39 (1967).

180. Lo, C. T., Lee, B., Gao, M. W., Chou, P. W. Ordering of block copolymer/nanoparticle composite thin films. *Polym. Int.* **62,** 99–105 (2013).

181. Siemann, U. The solubility parameter of poly(DL-lactic acid). *Eur. Polym. J.* **28,** 293–297 (1992).

182. Leibler, L., Orland, H., Wheeler, J. C. Theory of critical micelle concentration for solutions of block copolymers. *J. Chem. Phys.* **79,** 3550–3557 (1983).

183. Zhulina, E. B., Borisov, O. V. Theory of Block Polymer Micelles: Recent Advances and Current Challenges. *Macromolecules* **45,** 4429–4440 (2012).

184. Zhulina, E. B., Adam, M., Larue, I., Sheiko, S. S., Rubinstein, M. Diblock copolymer micelles in a dilute solution. *Macromolecules* **38,** 5330–5351 (2005).

185. Tuzar, Z., Munk, P., Riess, G., Hurtrez, G. *Solvents and Self-Organization of Polymers*. (1996).

186. Riess, G. Micellization of block copolymers. *Prog. Polym. Sci.* **28,** 1107–1170 (2003).

187. Hpone Myint, K., Brown, J. R., Shim, A. R., Wyslouzil, B. E., Hall, L. M. Encapsulation of Nanoparticles During Polymer Micelle Formation: A Dissipative Particle Dynamics Study. *J. Phys. Chem. B* **120,** 11582–11594 (2016).

188. Xu, J., Fan, Q., Mahajan, K. D., Ruan, G., Herrington, A., Tehrani, K. F., Kner, P, Winter, J. O. Micelle-templated composite quantum dots for super-resolution imaging. *Nanotechnology* **25,** (2014).

189. Nasongkla, N., Multifunctional Polymeric Micelles as Cancer-Targeted, MRI-Ultrasensitive Drug Delivery Systems. *Nano Lett.* **6,** 2427–2430 (2006).

190. Jeng, U. S., Sun, Y.-S., Lee, H.-Y., Hsu, C.-H., Liang, K. S. Binding effect of surface-modified cadmium sulfide on the microstructure of PS-*b*-PEO block copolymers. *Macromolecules* **37,** 4617–4622 (2004).

191. Nabar, G. M., Winter, J. O., Wyslouzil, B. E. Nanoparticle packing within block copolymer micelles prepared by the interfacial instability method. *Soft Matter* **14,** 3324–3335 (2018).

192. Wang, J., Li, W., Zhu, J. Encapsulation of inorganic nanoparticles into block copolymer micellar aggregates: Strategies and precise localization of nanoparticles. *Polymer* **55,** 1079–1096 (2014).

193. Li, X., Iocozzia, J., Chen, Y., Zhao, S., Cui, X., Wang, W., Yu, H., Lin, S., Lin, Z. From Precision Synthesis of Block Copolymers to Properties and Applications of Nanoparticles. *Angew. Chemie - Int. Ed.* **57,** 2046–2070 (2018).

194. Tritschler, U., Pearce, S., Gwyther, J., Whittell, G. R., Manners, I. 50th Anniversary Perspective: Functional Nanoparticles from the Solution Self-Assembly of Block Copolymers. *Macromolecules* **50,** 3439–3463 (2017).

195. Schulze, M. W., Lewis, R. M., Lettow, J. H., Hickey, R. J., Gillard, T. M., Hillmyer, M. A., Bates, F. S. Conformational Asymmetry and Quasicrystal Approximants in Linear Diblock Copolymers. *Phys. Rev. Lett.* **118,** 207801 (2017).

196. Moritani, M., Inoue, T., Motegi, M., Kawai, H., Kato, K. *Colloidal and Morphological Behavior of Block and Graft Copolymers*. (Plenum Press, 1971).

197. Lin, Y., Skaff, H., Emrick, T., Dinsmore, A. D., Russell, T. P. Nanoparticle Assembly and Transport at Liquid-Liquid Interfaces. *Science* **299,** 226–229 (2003).

198. Ku, K. H., Shin, J. M., Kim, M. P., Lee, C.-H.Size-controlled nanoparticle-guided assembly of block copolymers for convex lens-shaped particles. *J. Am. Chem. Soc.* **136,** 9982–9989 (2014).

199. Yeh, S.-W., Wei, K.-H., Sun, Y.-S., Jeng, U.-S., Liang, K. S. CdS Nanoparticles Induce a Morphological Transformation of Poly(styrene-*b*-4-vinylpyridine) from

Hexagonally Packed Cylinders to a Lamellar Structure. *Macromolecules* **38,** 6559–6565 (2005).

200. Yeh, S., Wei, K., Sun, Y., Jeng, U., Liang, K. S. Morphological Transformation of PS-*b*-PEO Diblock Copolymer by Selectively Dispersed Colloidal CdS Quantum Dots. *Macromolecules* **36,** 7903–7907 (2003).

201. Sides, S. W., Kim, B. J., Kramer, E. J., Fredrickson, G. H. Hybrid particle-field simulations of polymer nanocomposites. *Phys. Rev. Lett.* **96,** 250601 (2006).

202. Lo, C. T., Chang, Y. C., Wu, S. C., Lee, C. L. Effect of particle size on the phase behavior of block copolymer/nanoparticle composites. *Colloids Surfaces A Physicochem. Eng. Asp.* **368,** 6–12 (2010).

203. Singh, S. *et al.* Ligand displacement induced morphologies in block copolymer/quantum dot hybrids and formation of core–shell hybrid nanoobjects. *Phys. Chem. Chem. Phys.* **19,** 27651–27663 (2017).

204. Liang, R. Precise Localization of Inorganic Nanoparticles in Block Copolymer Micellar Aggregates: From Center to Interface. *Macromolecules* **48,** 256–263 (2015).